

UNIVERSITY OF CALIFORNIA, SAN DIEGO

Interplay of Superconductivity, Magnetism, and Density Waves
in Rare-Earth Tritellurides and Iron-Based Superconducting Materials

A dissertation submitted in partial satisfaction of the
requirements for the degree Doctor of Philosophy
in
Physics

by

Diego Andrés Zocco

Committee in charge:

Professor M. Brian Maple, Chair
Professor Dimitri Basov
Professor Jorge Hirsch
Professor Vitali Nesterenko
Professor Jeffrey Remmel

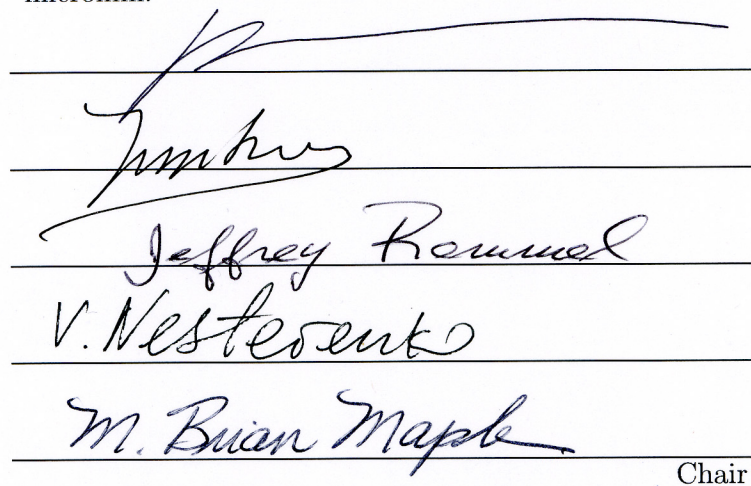
2011

Copyright

Diego Andrés Zocco, 2011

All rights reserved.

The dissertation of Diego Andrés Zocco is approved, and
it is acceptable in quality and form for publication on
microfilm:



Timothy J. Nesterenko

M. Brian Maple
Chair

University of California, San Diego

2011

A papá y mamá, Ángel and Lidia, y a mi hermana, Laura, por entenderme,
apoyarme y acompañarme, siempre.

We are a way for the cosmos to know itself.

The ash of stellar alchemy was now emerging into consciousness. At an ever-accelerating pace, it invented writing, cities, art and science, and sent spaceships to the planets and the stars. These are some of the things that hydrogen atoms do, given fifteen billion years of cosmic evolution.

– Carl Sagan, *Cosmos*

The select man, the excellent man is urged, by interior necessity, to appeal from himself to some standard beyond himself, superior to himself, whose service he freely accepts. The excellent man is the one who makes great demands on himself, and who lives in essential servitude. Life has no savor for him unless he makes it consist in service to something transcendental. Hence he does not look upon the necessity of serving as an oppression. When, by chance, such necessity is lacking, he grows restless and invents some new standard, more difficult, more exigent, with which to coerce himself. This is life lived as a discipline- the noble life (Noblesse oblige). “To live as one likes is plebeian; the noble man aspires to order and law” (Goethe). The privileges of nobility are not in their origin concessions or favors; on the contrary, they are conquests.

– José Ortega y Gasset, *The Revolt of the Masses*

Cualquier destino, por largo y complicado que sea, consta en realidad de un solo momento: el momento en que el hombre sabe para siempre quién es.

– Jorge Luis Borges

TABLE OF CONTENTS

Signature Page	iii
Dedication	iv
Epigraph	v
Table of Contents	vi
List of Figures	viii
List of Tables	xviii
Acknowledgements	xix
Vita, Publications, and Fields of Study	xxiii
Abstract	xxvi
I Introduction	1
A. Electronic Properties of Metals	2
1. Fermi Liquid Theory	2
2. Heavy Fermions	4
3. Magnetism in Metals	5
4. RKKY Interaction and the Kondo Effect	6
5. The Doniach Diagram, Quantum Critical Points and Non-Fermi Liquid Behavior	8
B. Superconductivity	11
C. Charge- and Spin-Density Waves in Low Dimensional Systems	15
1. Charge-density waves	19
2. Spin-density waves	22
D. Rare-Earth Tritellurides and Iron-Based Materials	23
Bibliography	24
II Experimental Methods	27
A. Sample Synthesis	27
B. High Pressure Techniques	28
1. Hydrostatic Piston-Cylinder Clamped Cell	28
2. Bridgman-Anvil Cell	31
3. Diamond-Anvil Cell	34
C. Measurement Methods	36
1. Electrical Resistivity	36
2. Magnetic Measurements	36
3. Calorimetry Measurements	40

Bibliography	43
III Superconductivity, Magnetism and Charge-Density Waves in Rare-Earth Tritellurides ($R\text{Te}_3$)	44
A. Introduction	44
B. Electronic Structure of $R\text{Te}_3$	49
C. Experimental Details	52
D. High-Pressure, Transport, and Thermodynamic Properties of CeTe_3	53
E. Pressure Induced Superconductivity in TbTe_3	62
F. DyTe_3 and GdTe_3	70
G. Discussion	78
1. Pressure Evolution of the Charge-Density Wave State in $R\text{Te}_3$ Single Crystals	78
2. The Superconducting State in $R\text{Te}_3$ Single Crystals	81
H. Summary	97
Bibliography	99
IV Superconductivity and Magnetism in Iron-Pnictide Compounds	103
A. Introduction	103
B. Experimental Details	108
C. Iron-Arsenide Compounds	109
1. The Superconducting $\text{LaFeAsO}_{1-x}\text{F}_x$ and $\text{CeFeAsO}_{1-x}\text{F}_x$ Com- pounds	109
2. Search for Pressure Induced Superconductivity in Undoped Ce- FeAsO	117
D. Iron-Phosphorous Compounds	124
1. Superconductivity in Single Crystals of LaFePO	124
2. High Pressure Stabilization of the Kondo Lattice behavior in Ce- FePO Single Crystals	131
E. Synthesis and High-Pressure Study of CuFeTe_2 Single Crystals	138
F. Summary	148
Bibliography	150

LIST OF FIGURES

Figure I.1: The Doniach phase diagram, in which the Kondo and the RKKY energy scales compete as a function of the tuning parameter $ JN(E_F) $, where J is the exchange coupling constant, and $N(E_F)$ is the density of electronic states at the Fermi energy level. The colored region represents a magnetically ordered phase below the Néel temperature T_N . At the critical value of the tuning parameter, T_N is suppressed to 0 K, and quantum fluctuations become important.	9
Figure I.2: Evolution of the superconducting transition temperature T_c for different materials throughout the years.	12
Figure I.3: (a) Response function χ as a function of wavevector q for a one-, two-, and three-dimensional free electron gas at $T = 0$. (b–d) Fermi surface topology for a 1D, 2D and quasi-1D electron gas. The arrows indicate pairs of states, one full, one empty, differing by the wavevector $q = 2k_F$ (from Ref. [2]).	17
Figure I.4: The single particle band, electron density and lattice distortion in the metallic state above T_{CDW} (<i>left</i>) and in the charge density wave state at $T = 0$ (<i>right</i>) for a half-filled band.	21
Figure II.1: <i>Left:</i> Piston-cylinder hydrostatic clamped cell diagram (from Ref. [7]). (a) Be-Cu clamping nut. (b) Be-Cu/WC load transmitter. (c, d) WC piston. (e) Be-Cu anti-extrusion disk. (f) Teflon capsule (sample space). (g) Be-Cu anti-extrusion sample holder. (h) WC backing piston. (i, j) WC backing plate and nut. (k) Inner cylinder (alloy). (l) Be-Cu body. <i>Right:</i> Photograph of the anti-extrusion sample holder, with two samples connected for electrical resistivity measurements. The tip of a toothpick is shown for size comparison.	30
Figure II.2: Photograph of an anvil utilized in the Bridgman-anvil high-pressure technique.	33
Figure II.3: Diamond-anvil cell technique. The upper diamond is a blank diamond, while the bottom one is a “designer” diamond, with deposited tungsten microprobes encapsulated in high-quality homoepitaxial diamond, for electrical resistivity measurements, as can be seen in more detail in the photograph. The sample is located in the space enclosed by the two diamonds and the hole of the gasket.	35
Figure II.4: Coils system designed for ac-susceptibility measurements in the piston-cylinder clamped cells. The photograph on the right shows the coils mounted on a anti-extrusion sample holder of 0.25” in diameter.	38

Figure II.5: Test of the coil system designed for ac-susceptibility measurements in the hydrostatic cell. For this test, one sample of Pb and another of Sn were placed on each side of the secondary coils. The voltage induced in the coils was pre-amplified before being detected with the lock-in amplifier at 1023 Hz.	39
Figure II.6: Photograph of a TbTe_3 single crystal with three $50\ \mu\text{m}$ Au wires and a thermocouple made of spot-welded Au and $\text{Au}_{0.93}\text{Fe}_{0.07}$ $50\ \mu\text{m}$ wires for electrical resistivity and ac-calorimetry measurements. Underneath the sample, a $1\times 1\ \text{mm}^2$ ruled paper was placed as a reference.	42
Figure III.1: Crystal structure of $R\text{Te}_3$, consisting of alternating double layers of nearly square planar Te sheets and corrugated double $R\text{Te}$ layers. This series of compounds crystallizes in the NdTe_3 structure that belongs to the space group $Cmcm$ (No. 63), with the b -axis oriented perpendicular to the ac -planes. The unit cell is enclosed in the box. Crystal structure created with <i>Vesta</i> [19].	47
Figure III.2: Charge-density wave ordering temperatures $T_{CDW,1}$ and $T_{CDW,2}$ (<i>left axis</i>) and Néel temperature T_N (<i>right axis</i>) plotted as a function of in-plane lattice parameter a for the different $R\text{Te}_3$ compounds. The dashed line serves as a guide to the eye, suggesting that the lighter Nd, Pr, Ce and La compounds would possibly order into the CDW state at $T_{CDW,1}$ larger than 400 K. Lattice parameters were extracted from Ref. [8]. Values of $T_{CDW,1}$ and $T_{CDW,2}$ were obtained from Ref. [10], and T_N values from Refs. [11, 17].	48
Figure III.3: (a): The p_x and p_y orbitals in the single Te square lattice (from Ref. [21]). (b): Angle-resolved photoemission spectroscopy image of CeTe_3 (from Ref. [4]). Solid and dashed black lines outline the Fermi surface. Solid red and blue lines represent the calculated energy dispersions with a Fermi energy fixed according to the filling of the orbitals expected from stoichiometry. The green solid line corresponds to the limit of the 2DBZ, while the yellow solid squares delineate the 3DBZ.	51
Figure III.4: Electrical resistivity versus temperature at various pressures for CeTe_3 single crystals. <i>Upper panel</i> : Hydrostatic cell experimental results. The <i>inset</i> shows the low temperature range, displaying the onset of the magnetic order as $T_{1,\rho}$. <i>Lower panel</i> : Bridgeman-anvil cell results. The <i>inset</i> shows $T_{1,\rho}$, along with the new ordering temperature $T_{2,\rho}$, indicated in the figure for the first Bridgeman run (for the 15.2 GPa curve) and for the second Bridgeman run (<i>in black, dashed curve</i>).	58

Figure III.5: Electronic and magnetic contribution to the specific heat for different magnetic fields applied along the b -axis of the CeTe_3 crystals. $T_{1,C}$ corresponds to the field-independent ordering temperature centered near 3 K, while $T_{2,C}$ denotes the field-dependent feature below 1.5 K. In the lower <i>inset</i> , the solid curve (blue) corresponds to the electronic and magnetic entropy in zero magnetic field and the horizontal dashed line corresponds to the value $R\ln 2 \text{ J/mol-K}$. The upper <i>inset</i> shows a schematic diagram of the crystal structure of CeTe_3 and the direction of the applied magnetic field in the specific heat experiment.	59
Figure III.6: <i>Left</i> : Field dependence of the magnetic ordering temperatures $T_{1,\rho}$ and $T_{2,C}$ of CeTe_3 for magnetic fields applied perpendicular and parallel to the b -axis. A logarithmic temperature scale was chosen to emphasize the curvature of T_2 vs H . <i>Right</i> : Temperature dependence of the electrical resistivity near T_1 for magnetic fields applied parallel (<i>upper-right</i> ; 0, 3, 6 and 9 T) and perpendicular (<i>lower-right</i> ; 0, 0.5, 1, 1.5, 3, 4, 5, 6 and 9 T) to the b -axis of the crystals. The arrows mark the position of T_1 . The numbers on each curve denote the value of the applied magnetic field in tesla. For the lower-right panel, arrows and numbers for fields of 0.5 and 1 T are not displayed for better clarity.	60
Figure III.7: Temperature T versus pressure P phase diagram for CeTe_3 (note the logarithmic temperature scale). T^* - characteristic temperature associated with the hump-like feature in $\rho(T)$, possible origins of which are discussed in the text; T_1 - magnetic ordering temperature; T_2 - ordering temperature (probably magnetic). The vertical dashed line separates the $T - P$ phase diagram into two regions in which T^* , T_1 , and T_2 all have distinctly different pressure dependences. <i>Inset</i> : room temperature evolution of the electrical resistance as the pressure was increased.	61
Figure III.8: Magnetization M versus applied field H at several temperatures. At temperatures below T_N , a change in slope near 1-3 T is suggestive of metamagnetism. At higher fields, hysteretic jumps in the magnetization indicate a first order phase transition. <i>Inset</i> : low temperature region where a clear drop is visible in the susceptibility, consistent with AFM ordering.	65
Figure III.9: Specific heat C versus temperature T for TbTe_3 at ambient pressure and fields up to 5 T. For clarity, the curves have been offset vertically by a constant amount indicated in parentheses near the right side of the curves. Three distinct peaks, indicated by arrows, are visible near the Néel temperature at 6 K. <i>Inset</i> : the field dependence of the specific heat anomalies. The dashed line fits are described in the text.	66

67

Figure III.11: Electrical resistivity measured in the *ac* plane of TbTe_3 at various pressures. The upper panel shows data from the piston-cylinder cell and first Bridgman-anvil cell experiment, while the lower panel shows data taken from the second Bridgman-anvil cell experiment. At several pressures, the resistance becomes negligible below the transition confirming superconductivity. *Upper inset:* Resistivity versus temperature in the vicinity of T_N at selected pressures. The dashed and solid black lines indicate the value of T_N at 0.1 GPa. *Lower inset:* Relative change in the 6 K resistance, taken from the second Bridgman-anvil cell experiment. 68

68

69

73

Figure III.14: Electrical resistivity of DyTe_3 from the hydrostatic experiments, up to pressures to 2.7 GPa. Since DyTe_3 is ordered in the upper CDW state at ambient pressure, the sharp feature at $T_{CDW,1}$ is observed for all the curves. The lower CDW is only observed $T_{CDW,2}$ for the 0.7 GPa derivative of the electrical resistivity with respect to the temperature (not shown here). In the <i>inset</i> , which displays the low temperature region, it is possible to distinguish a small step in the resistivity which corresponds to the onset to the AFM state. The sharp drop in the resistivity at T_c is indicative of the onset of the superconductive state.	74
Figure III.15: <i>Left panels</i> : temperature and magnetic field dependence of the electrical resistivity close to the superconducting transition of GdTe_3 for pressures of 2.5, 1.8 and 1.2 GPa obtained in the hydrostatic cell experiments. Values of T_c were determined as the temperature at which the resistivity dropped by 50% (<i>horizontal dashed lines</i>). The values in Oe displayed in these diagrams were adjusted as described in the main text <i>right panels</i>	75
Figure III.16: <i>Left panels</i> : temperature and magnetic field dependence of the electrical resistivity close to the superconducting transition of DyTe_3 for pressures of 2.5, 1.8 and 1.2 GPa obtained in the hydrostatic cell experiments. Values of T_c were determined as the temperature at which the resistivity dropped by 50% (<i>horizontal dashed lines</i>). The values in Oe displayed in these diagrams were adjusted as described in the main text <i>right panels</i>	76
Figure III.17: Critical field H_c vs. temperature T for GdTe_3 and DyTe_3 at 1.2, 1.8 and 2.5 GPa. The renormalized values of H_c arise from a correction of the magnetic fields applied during the experiment. Solid lines correspond to linear fits to the actual data, while dashed lines are the calculated $H_c(T)$ curves for low T	77
Figure III.18: Pressure dependence of the charge-density wave transition temperatures $T_{CDW,1}$ (<i>larger symbols</i>) and $T_{CDW,2}$ (<i>smaller symbols</i>) for the GdTe_3 , TbTe_3 and DyTe_3 samples. Dashed lines are guides to the eye.	80
Figure III.19: Pressure dependence of the superconducting transition temperatures T_c for the GdTe_3 , TbTe_3 and DyTe_3 samples. Data below 3 GPa were obtained in the hydrostatic clamped-cell experiments, while higher pressure data were obtained from the Bridgman-anvil cell experiments.	89
Figure III.20: Room-temperature electrical resistivity ρ as a function of applied pressure normalized to ambient pressure, obtained during pressurization of the cells. For TbTe_3 , two sets of data are presented since complementary measurements were performed in two separate Bridgman-anvil cell runs.	90

Figure III.21: Lattice parameters (<i>a</i>) and unit cell volume (<i>b</i>) for CeTe ₃ at 300 K as a function of pressure (from Ref. [25]).	91
Figure III.22: The pressure dependence of tellurium. (<i>a</i>) Room-temperature electrical resistance vs. applied load and pressure. The <i>inset</i> shows $R(T)$ at various pressures in the superconducting transition temperature region (from Ref. [37]). (<i>b</i>) High-temperature and high-pressure phase diagram. The line between the Te-I (insulating) and Te-II (metallic) phases suggests that below 300 K, Te metal might be an insulator at pressures below 4 GPa (from Ref. [38]). (<i>c</i>) Superconducting temperature T_c of tellurium metal at various pressures below ~ 25 GPa (from Ref. [36]). (<i>d</i>) More recent T_c vs. P phase diagram of tellurium, up to ~ 40 GPa (from Ref. [39]).	92
Figure III.23: Electrical resistivity of pure tellurium at 1.2 GPa obtained from the experiment carried out in the dilution refrigerator down to ~ 150 mK. The <i>inset</i> shows in more detail the low temperature region for the tellurium and TbTe ₃ samples measured simultaneously in the same pressure cell. From these measurements, no indication of metallic nor superconducting state was found for the tellurium sample at this pressure, whereas the TbTe ₃ sample measured at the same pressure displayed superconductivity.	93
Figure III.24: Electrical resistivity ρ (<i>left axis</i>) and ac-calorimetry heat capacity C (<i>right axis</i>) versus temperature T for a TbTe ₃ single crystal under 2.4 GPa of applied pressure in the hydrostatic clamp. Both measurements were taken with the same sample, in the same set-up. At 6.5 K, the AFM transition at T_N is clearly observed with both techniques. The superconducting transition is observed at T_c in the electrical resistivity only.	94
Figure III.25: <i>Upper panel</i> : AC susceptibility χ (in μ V) for a sample of superconducting Sn and several samples of TbTe ₃ loaded in opposite sides of the secondary coils as it is displayed in the cartoon. <i>Lower panel</i> : The superconducting transition of TbTe ₃ at different applied magnetic fields. The <i>inset</i> displays the resulting H_c vs. T_c phase diagram.	95

Figure III.26: $T - P$ phase diagram for the superconducting $R\text{Te}_3$. The charge-density wave temperature $T_{CDW,1}$ is suppressed with pressure, and its corresponding feature can no longer be distinguished from our measurements above 2.7 GPa. At intermediate temperatures, magnetism from the rare-earth ions is present at T_N . At lower temperatures, a superconducting phase appears at 1.2 GPa and $T_c \sim 0.3$ K, and reaches a maximum value of T_c of 3.5 K at 12 GPa. The possible origins of the superconducting phases are discussed in the main text. The black line corresponds to the Te data from Ref. [36], and red diamonds are from Ref. [38].	96
Figure IV.1: Crystal structure of $R\text{FePnO}$ (R = rare-earth atom, Pn = As, P), consisting of layers of Pn -Fe- Pn tetrahedra and alternating layers of rare-earth and oxygen. Crystal structure created with <i>Vesta</i> [20].	106
Figure IV.2: A comparison of the evolution of the superconducting transition temperature T_c versus lanthanide Ln for the series $Ln\text{FePO}$ (<i>solid squares</i>), the optimally fluorine doped compounds $Ln\text{FeAsO}_{1-x}\text{F}_x$ (<i>solid circles</i>), and the oxygen deficient compounds $Ln\text{FeAsO}_{1-\delta}$ (<i>open circles</i>) (from Ref. [18]).	107
Figure IV.3: Electrical resistance R vs. temperature T of $\text{LaFeAsO}_{0.89}\text{F}_{0.11}$ for different applied pressures. <i>Upper panel</i> : curves corresponding to the hydrostatic clamped-cell technique. <i>Lower panel</i> : diamond-anvil cell experiment.	113
Figure IV.4: Superconducting transition temperature T_c vs. pressure P of $\text{LaFeAsO}_{1-x}\text{F}_x$. Red circles correspond to measurements in the hydrostatic cell, and red diamonds correspond to the diamond-anvil cell experiment, both for a sample containing $\sim 11\%$ of fluorine. The solid red line is a guide to the eye. The black dashed curve represents the data previously published by Takahashi <i>et al.</i> for a sample containing $\sim 11\%$ of F [4]. The black dashed curve represents the data previously published by Garbarino <i>et al.</i> for a sample containing $\sim 10\%$ of F [28].	114
Figure IV.5: Temperature dependence of the electrical resistance R of $\text{CeFeAsO}_{0.88}\text{F}_{0.12}$ for different applied pressures up to 8.6 GPa using the Bridgman-anvil cell technique. The superconducting T_c is defined as the temperature at which the sample resistance reaches 90% of the normal state value. <i>Inset</i> : diamond anvil cell resistance curves for 1.8 and 19 GPa, normalized to their respective base temperature values.	115
Figure IV.6: Superconducting T_c versus pressure P of $\text{CeFeAsO}_{0.88}\text{F}_{0.12}$. The dashed curve is a guide to the eye given by a quadratic fit of the data, extrapolating to zero temperature at ~ 19 GPa.	116

Figure IV.7: (a) Electrical resistivity ρ versus temperature T at various pressures P for CeFeAsO polycrystalline samples, obtained in the hydrostatic clamped cell experiment. (b) Evolution of $T_{N,Ce}$ at low temperatures. (c) $d\rho/dT$ vs. T curves for the hydrostatic experiment. The arrows indicate the position of T^*	121
Figure IV.8: (a) Electrical resistivity ρ versus temperature T at various pressures P for CeFeAsO polycrystalline samples for the Bridgman-anvil cell experiment. The curves are shifted for clarity. The pressure and magnitude of the offset are indicated in parentheses at the right of the curves. (b) Low temperature detail, showing the evolution of $T_{N,Ce}$ at various pressures. (c) $d\rho/dT$ vs. T curves for the Bridgman-anvil cell experiment. (d) Diamond-anvil cell resistivity curves normalized to 270 K. (e) Low temperature detail for the higher pressures.	122
Figure IV.9: T - P phase diagram for CeFeAsO. In (a), data corresponding to the Bridgman-anvil technique are shown shifted to match the hydrostatic cell measurements. In the <i>upper panel</i> , the shaded region indicates the pressure range where the value of T^* is more difficult to determine from the measurements.	123
Figure IV.10: Electrical resistivity ρ versus temperature T of a LaFePO single crystal measured in the <i>ab</i> -plane for an as-grown single crystal and a crystal that was reduced in flowing argon at 700 °C for \sim 12 hours. <i>Left inset</i> : Resistivity over the entire measured temperature range showing T^2 behavior for \sim 10-100 K and linear T behavior for \sim 100-300 K. <i>Right inset</i> : Log-log plot of $\rho - \rho_0$ versus T . The solid red lines are fits to the data which demonstrate the T^2 behavior for 10-100 K for the as grown sample and 10-80 K for the reduced sample.	127
Figure IV.11: Electrical resistivity ρ versus temperature T of a LaFePO single crystal measured in the diamond-anvil cell. The top and bottom panels display the data obtained from two different contact configurations of the six-lead designer diamond.	128
Figure IV.12: <i>Top panels</i> : Electrical resistance normalized to the values at 15 K for two different lead configurations. The onset T_c is defined as the intersection of the dashed lines. Numbers indicate the order in which the pressures were applied. <i>Main panel</i> : Pressure dependence of the onset T_c . The value of the T_c at ambient pressure corresponds to the measurement of R versus T shown in Fig. IV.10, while the high-pressure points correspond to the DAC measurements. The high temperature limit of the vertical bars correspond to the temperature at which $\rho(T)$ deviates from the normal state behavior. Data from three different experiments performed by Igawa <i>et al.</i> are also shown for comparison [43]. . .	129

Figure IV.13: <i>Top panel</i> : AC-magnetic susceptibility of LaFePO at various increasing pressures, indicated beside each measurement. The values of T_c are indicated by the arrows, and correspond to the voltage value at the midpoint of the maximum and minimum voltages observed at the superconducting transition. <i>Bottom panel</i> : Low-pressure evolution of the T_c of LaFePO from the ac-susceptibility experiments (<i>blue and red triangles</i>). The open circles and filled diamonds correspond to previous data by Igawa <i>et al.</i> [43] and Schilling <i>et al.</i> [44].	130
Figure IV.14: Electrical resistivity ρ versus temperature T of CeFePO single crystals at pressures P of 0.01, 0.10, 0.42, 1.07, 1.62, 2.24 and 2.68 GPa, obtained with the hydrostatic clamped cell technique. <i>Inset</i> : low temperature region.	134
Figure IV.15: Evolution of the coherence temeperature of CeFePO as a function of pressure.	135
Figure IV.16: Magnetization M divided by applied magnetic field H versus temperature T of CeFePO. Fields of 1 T were applied perpendicular to the c -axis (<i>blue circles</i>) and parallel to the c -axis (<i>green triangles</i>). The <i>inset</i> displays the $M - H$ measurements performed at 2 K and at 30 K, also for H applied perpendicular and parallel to the c -axis of the samples.	136
Figure IV.17: Low temperature detail of the magnetization and specific heat measurements performed on annealed single crystals of Ce-FePO. The magnetization data shown in (a) was taken with a magnetic field of 1 T applied along the c -axis of the crystals, and the arrows indicate the cooling and warming curves. The Ce-contribution to the specific heat shown in (b) was obtained after subtracting the non-magnetic LaFePO data. The dashed line corresponds to the previous results presented in Ref. [45].	137
Figure IV.18: Crystal structure of CuFeTe ₂ . Cu and Fe atoms (<i>red</i>) occupy the $2a(0\ 0\ 0)$ -sites, with occupancies of the order of 50%, with the Te atoms (<i>green</i>) tetrahedrally coordinated with the Cu/Fe atoms. In the defect Cu ₂ Sb structure, additional sites at $[2c'-(0\ \frac{1}{2}\ z')]$ are partially occupied ($\lesssim 15\%$) by Cu and Fe atoms.	142
Figure IV.19: Photography of a single crystal of CuFeTe ₂ . Typical platelets are $\sim 50\ \mu\text{m}$ thick.	143
Figure IV.20: Powder x-ray diffraction pattern of CuFeTe ₂ ($I_{obs} - I_{bck}$, <i>black squares</i>). The fit to the data was obtained from the Rietveld analysis ($I_{calc} - I_{bck}$, <i>red line</i>). The background was subtracted from the experimental data and the fit. The blue line indicates the difference between observed and calculated data.	144

Figure IV.21: Zero-field cooled and field-cooled magnetization M versus temperature T of CuFeTe_2 obtained with an applied magnetic field of 500 Oe. The prominent feature at 125 K is consistent with the Verway transition found in magnetite (Fe_3O_4) [57].	145
Figure IV.22: Electrical resistivity ρ versus temperature T of CuFeTe_2 obtained in the hydrostatic clamped-cell experiment. The <i>inset</i> shows, in the left axis, the values of resistivity ρ_{4K} measured at 4 K as a function of pressure, and in the right axis, the energy gap values Δ also as a function of pressure, obtained as described in the main text.	146
Figure IV.23: Electrical resistance R versus temperature T of CuFeTe_2 obtained in the diamond-anvil cell experiment. Black curves correspond to the measurements taken during the cooling of the probe, while red, green and blue curves were measured during the warming cycles for pressures of 4, 14 and 34 GPa, respectively. The lower panel displays the resistance curves normalized to their respective values of resistance measured at 270 K. The <i>inset</i> shows in detail the low temperature region of the 34 GPa curve measured during the warm-up cycle.	147

LIST OF TABLES

ACKNOWLEDGEMENTS

First and foremost I would like to thank my advisor Prof. M. Brian Maple for the opportunity he gave me to work in his laboratory. Throughout all these years I have learned from him many things (especially about capybaras), but most importantly, to be always respectful with one's research peers. His exemplary sense of scientific responsibility will remain with me forever.

I infinitely thank everyone I met in Maple's lab: James Hamlin, for having to deal with my personality, for the "let's raise the pressure" musical moments, for the good memories from Croatia; a large part of the work in this dissertation could not have been possible without his knowledge in high-pressure techniques and patience. Jason Jeffries, for teaching me the initial steps in high-pressure. Nick Butch, for the long conversations about research and academia. Ryan (Eagle) Baumbach, for the good moments in the old surface lab office, and all the support and the samples you provided to us during your last years in the group as a postdoc. Johnpierre Paglione, for your great sense of humor, and for sharing your experiences about the field. Ben Taylor, for helping out with the PPMS and MPMS. Pei-Chun Ho, for teaching us all the tricks about dilution refrigerators. Todd Sayles, for running the specific heat in the rare-earth tritellurides experiments. Bill Yuhasz, for the initial lessons about crystal growth. Marc Janoschek and Lei Shu, for the support on the PPMS specific heat measurements, and for sharing with me the foreigner point of view. Noravee Kanchanavatee, I need to thank you for telling me about the amazing thai restaurant; I hope I didn't bother you so much with my necessity of having the gold leads perfectly laid on the samples. Eileen Gonzalez, Xiaoqian Chen, Nicole Crisosto, Kevin Huang, Colin McElroy, Ivy and Soo-joung: I thank you for all the work in sample prep, and for adding the fresh quote of fun to every day. Neil Frederick, Ben Yukich, Columbine Robinson, Tatsuya Yanagisawa, Dan Scanderbeg, and the newer postdocs, Ben White and Duygu Yazici Tütün, for your assistance throughout the last six years. I would also like to thank Brian's assistants: Carolyn Rosado, Audrey Morris and

Christine Coffey, for helping with administrative matters, and Gary Doran, for taking care of all the money-related matters.

Many thanks to the people from the Physics Department at UCSD: Debra Bomar, Hilari Ford, Sharmila Poddar, Charmaine Samahin-Manns, Tracy Williams, Brad Hanson, for their support regarding grad-student matters. Paul Redgate, Jeff Phillips, Dirk Johnson and Lester Brooks of Physics Facilities, for their technical assistance. Allen White, Clem Demmitt and George Kassabian from the Physics Electronics Shop, for quickly repairing the electronics. And Don Johnson and the people from the Campus Research Machine Shop, for carefully machining the small parts for the pressure cells.

I would also like to thank our collaborators: Dr. Sam Weir from Lawrence Livermore National Laboratory and Prof. Yogesh Vohra from University of Alabama at Birmingham, for supplying designer diamonds for the high-pressure diamond anvil cell (DAC) measurements. Prof. Ian Fisher and his research group in Stanford University, for providing the rare-earth tritellurides single crystals and for the enlightening discussions about the high-pressure data. Michael McGuire, Athena Sefat, Brian Sales, Rongying Jin and David Mandrus from Oak Ridge National Laboratory, for providing the iron-arsenide samples. Dr. Ana Celia Mota for her advises on running the dilution refrigerator. From the collaboration in the Bi-2212 paper, I specially thank Tanja Cuk from UC Berkeley. I express my most sincere thanks to Prof. Andrzej Ślebarski for the collaboration in the CeRhSn experiments.

I am in great debt with the people from Los Alamos, everyone in the Magnet Lab, especially with Marcelo Jaime, for giving me the opportunity to work with him during the year before I arrived to San Diego, and with Vivien Zapf, for teaching me how to cool down the dilution refrigerator and for being infinitely patient with my English. I want to dedicate this thesis in particular to the one-of-a-kind group of friends I met there: Alejandro Silhanek and La Euge, Boris Maiorov, Leonardo Civale, Ross and Rebecca McDonald, Paul Goddard and

Eleanor, and my soul friend Kelly Nguyen.

I would like to express my most sincere thanks to my friends in Argentina who feed me every time I go back to visit, in particular Fer, César and María Luz who I miss a lot. And to Cecilia, with whom I shared many years full of experiences in the US; I hope we can continue sharing new ones in the future. I also thank the friends I made from my physics class: Misha, for all the years living together, for all the travels and adventures, I wish you the best; to Dave, Sara, Mikas and Mariano; to all the Arovas' Madmen Physics' soccer team, especially Matt LeBourgeois, Alex High, Jonathan Whitmore, Frank Golf, Ryan and Randy Kelley, Toby Webber, Chris Schroeder, and Jeff Noel (the only unitedstatian who was willing to drink mate with me), for all the good and bad games and the after-games at the happy hour.

A Milda, gracias por todo lo vivido en los últimos dos años. Sigo aprendiendo mucho de tu forma dionisíaca de ver las cosas. Te agradezo por los pies descalzos, por la música, por entenderme, por las conversaciones y los tiempos de lectura en silencio, por los silencios, por ser mi enciclopedia de historia, por las tortuguitas, por los atardeceres y las caminatas en la playa, por los escapes y los viajes a los lugares más simples de la Tierra.

Lastly and most importantly, I thank to my parents, Ángel and Lidia, and my sister, Laura, for their unconditional support they offered me throughout all these years I have been geographically far from them. Thank you for understanding my necessities. Los quiero mucho.

A portion of the text and data presented in Chapter III are reprints of material that appears in “High-pressure, transport, and thermodynamic properties of CeTe₃,” D. A. Zocco, J. J. Hamlin, T. A. Sayles, M. B. Maple, J. -H. Chu, and I. R. Fisher, Phys. Rev. B **79**, 134428 (2009), “Pressure-induced superconducting phase in the charge-density-wave compound terbium tritelluride,” J. J. Hamlin, D. A. Zocco, T. A. Sayles, M. B. Maple, J. -H. Chu, and I. R. Fisher, Phys. Rev. Lett. **102**, 177002 (2009), and “Superconductivity in rare-earth tritellurides,” D.

A. Zocco, J. J. Hamlin, M. B. Maple, J. -H. Chu, and I. R. Fisher, *in preparation*. The dissertation author is a primary researcher and first author of the first and third articles and primary researcher and second author of the second article.

A portion of the text and data presented in Chapter IV are reprints of material that appears in “Effect of pressure on the superconducting critical temperature of $\text{La}[\text{O}_{0.89}\text{F}_{0.11}]\text{FeAs}$ and $\text{Ce}[\text{O}_{0.88}\text{F}_{0.12}]\text{FeAs}$,” D. A. Zocco, J. J. Hamlin, R. E. Baumbach, M. B. Maple, M. A. McGuire, A. S. Sefat, B. C. Sales, R. Jin, D. Mandrus, J. R. Jeffries, S. T. Weir, and Y. K. Vohra, *Physica C* **468**, 2229 (2008), “Superconductivity in single crystals of LaFePO ,” J. J. Hamlin, R. E. Baumbach, D. A. Zocco, T. A. Sayles, and M. B. Maple, *Journal of Physics: Condensed Matter* **20**, 365220 (2008), “Superconductivity in LnFePO ($\text{Ln} = \text{La, Pr, and Nd}$) single crystals,” R. E. Baumbach, J. J. Hamlin, L. Shu, D. A. Zocco, N. Crisosto, and M. B. Maple, *New J. of Phys.* **11**, 025018 (2009), and “Search for pressure induced superconductivity in CeFeAsO and CeFePO iron pnictides,” D. A. Zocco, R. E. Baumbach, J. J. Hamlin, M. Janoschek, I. K. Lum, M. A. McGuire, A. S. Sefat, B. C. Sales, R. Jin, D. Mandrus, J. R. Jeffries, S. T. Weir, Y. K. Vohra, and M. B. Maple, *Phys. Rev. B* **83**, 094528 (2011). The dissertation author is a primary researcher and first author of the first and fourth articles, primary researcher and third author of the second article, and co-author of the third article.

Funding for this research was provided by the United States Department of Energy (DOE) and the National Science Foundation (NSF). Part of this work overlaps with a project partially funded by the National Nuclear Security Administration under the auspices of the Stewardship Stockpile Academic Alliances program (NNSA/SSAA).

VITA

2001–2003	Teaching Assistant, Department of Physics Universidad de Buenos Aires, Buenos Aires, Argentina
2003	Licenciado en Ciencias Físicas, Universidad de Buenos Aires, Buenos Aires, Argentina
2004–2005	Graduate Research Assistant Los Alamos National Laboratory, Los Alamos, New Mexico, USA Advisor: M. Jaime – V. Zapf
2005–2006	Teaching Assistant, Department of Physics University of California, San Diego, California, USA
2005–2011	Graduate Research Assistant University of California, San Diego, California, USA Advisor: M. Brian Maple
2006	Master of Science, Physics University of California, San Diego, California, USA
2011	Doctor of Philosophy, Physics University of California, San Diego, California, USA

PUBLICATIONS

- D. A. Zocco, J. J. Hamlin, M. B. Maple, J. -H. Chu and I. R. Fisher, “Superconductivity in rare-earth tritellurides,” *in preparation*.
- D. A. Zocco, A. Ślebarski, and M. B. Maple, “High-pressure study of non-Fermi liquid behavior and spin glass order in CeRhSn,” *submitted to Phys. Rev. B*.
- J. J. Hamlin, K. Huang, N. Kanchanavatee, R. E. Baumbach, M. Janoschek, C. McElroy, D. A. Zocco, and M. B. Maple, “Evolution of the magnetic and superconducting states in UCoGe with Fe and Ni substitution,” *submitted to Phys. Rev. B*.
- J. J. Hamlin, J. R. Jeffries, G. Samudrala, Y. K. Vohra, S. T. Weir, D. A. Zocco, and M. B. Maple, “Low temperature electrical resistivity of praseodymium at pressures up to 120 GPa,” *accepted in Phys. Rev. B Brief Reports*.
- L. Shu, R. E. Baumbach, M. Janoschek, E. Gonzales, K. Huang, T. A. Sayles, J. P. Paglione, J. OBrien, J. J. Hamlin, D. A. Zocco, P.-C. Ho, C. A. McElroy, and M. B. Maple, “Superconductivity and non-Fermi-liquid behavior in $\text{Ce}_{1-x}\text{Yb}_x\text{CoIn}_5$,” *Phys. Rev. Lett.* **106**, 156403 (2011).

- D. A. Zocco, R. E. Baumbach, J. J. Hamlin, M. Janoschek, I. K. Lum, M. A. McGuire, A. S. Sefat, B. C. Sales, R. Jin, D. Mandrus, J. R. Jeffries, S. T. Weir, Y. K. Vohra, and M. B. Maple, “Search for pressure induced superconductivity in CeFeAsO and CeFePO iron pnictides,” *Phys. Rev. B* **83**, 094528 (2011).
- R. E. Baumbach, J. J. Hamlin, L. Shu, D. A. Zocco, J. R. OBrien, P.-C. Ho, and M. B. Maple, “Unconventional T-H Phase Diagram in the Noncentrosymmetric Compound Yb₂Fe₁₂P₇,” *Phys. Rev. Lett.* **105**, 106403 (2010).
- T. Cuk, D. A. Zocco, H. Eisaki, V. Struzhkin, M. Grosche, M. B. Maple, and Z.-X. Shen, “Signatures of pressure induced superconductivity in insulating Bi2212,” *Phys. Rev. B* **81**, 184509 (2010).
- J. J. Hamlin, D. A. Zocco, T. A. Sayles, M. B. Maple, J. -H. Chu and I. R. Fisher, “Pressure induced superconductivity in the charge density wave compound TbTe₃,” *Phys. Rev. Lett.* **102**, 177002 (2009).
- D. A. Zocco, J. J. Hamlin, T. A. Sayles, M. B. Maple, J. -H. Chu and I. R. Fisher, “High-pressure, transport, and thermodynamic properties of CeTe₃,” *Phys. Rev. B* **79**, 134428 (2009).
- N. P. Butch, J. R. Jeffries, D. A. Zocco, and M. B. Maple, “Hydrostaticity and hidden order: effects of experimental conditions on the temperature-pressure phase diagram of URu₂Si₂,” *High Pressure Res.* **29**, Issue 2, 335 - 343 (2009).
- R. E. Baumbach, J. J. Hamlin, L. Shu, D. A. Zocco, N. Crisosto, and M. B. Maple, “Superconductivity in LnFePO (Ln = La, Pr, and Nd) single crystals,” *New J. Phys.* **11**, 025018 (2009).
- J. J. Hamlin, R. E. Baumbach, D. A. Zocco, T. A. Sayles, and M. B. Maple, “Superconductivity in single crystals of LaFePO,” *J. Phys.: Condens. Matter* **20**, 365220 (2008).
- D. A. Zocco, J. J. Hamlin, R. E. Baumbach, M. B. Maple, M. A. McGuire, A. S. Sefat, B. C. Sales, R. Jin, D. Mandrus, J. R. Jeffries, S. T. Weir, and Y. K. Vohra, “Effect of pressure on the superconducting critical temperature of La[O_{0.89}F_{0.11}]FeAs and Ce[O_{0.88}F_{0.12}]FeAs,” *Physica C* **468**, 2229 (2008).
- V. S. Zapf, D. Zocco, B. R. Hansen, M. Jaime, N. Harrison, C. D. Batista, M. Kenzelmann, C. Niedermayer, A. Lacerda, and A. Paduan-Filho, “Bose-Einstein Condensation of S = 1 Ni spin degrees of freedom in NiCl₂-4SC(NH₂)₂,” *Phys. Rev. Lett.* **96**, 077204 (2006).
- A. V. Silhanek, D. Zocco, M. Jaime, N. Harrison, T. Ebihara, “Approaching field tuned quantum criticality in CeIn_{3-x}Sn_x,” *Physica B* **378-380**, pp. 90 - 91 (2006).
- D. Zocco, M. Monteverde, M. Núñez-Regueiro and C. Acha, “Uniaxial pressure dependence of the dynamical properties of vortex lines in Bi-2212 single crystals,” *Physica B* **354**, pp. 261 - 265 (2004).

FIELDS OF STUDY

Major Field: Physics

Studies in strongly correlated electron materials

M. Brian Maple, Bernd T. Matthias Professor of Physics,
University of California, San Diego

ABSTRACT OF THE DISSERTATION

Interplay of Superconductivity, Magnetism, and Density Waves
in Rare-Earth Tritellurides and Iron-Based Superconducting Materials

by

Diego Andrés Zocco
Doctor of Philosophy in Physics
University of California, San Diego, 2011
Professor M. Brian Maple, Chair

Superconductivity, charge- and spin-density waves are collective electronic phenomena that originate from electron-electron and electron-phonon interactions, and the concept of Fermi surface competition between these collective states is one of the most fundamental problems of condensed matter physics. High pressures provide a clean method to tune the electronic properties that determine the superconducting, magnetic or charge-ordered ground states of complex materials. The charge-density wave, magnetic and superconducting ordered states of the rare-earth tritellurides system, and the interplay between the spin-density wave, localized magnetism and superconductivity in the recently discovered Fe-based high-temperature superconductors, have been investigated under extreme conditions of pressure, magnetic field and low temperatures.

I

Introduction

A broken symmetry appears when a property of some material transforms from a disordered phase to an ordered phase. The broken symmetry is characterized by an order parameter. For example, the magnetization M is the order parameter for a magnet, which characterizes the broken rotational symmetry of the material. Common states with broken symmetries in condensed matter physics include magnetism, superconductivity (SC), spin- and charge-density-wave states (SDW, CDW), to cite some. Among the states of broken symmetry in a solid, SC and CDW are two prominent ones which require an attractive electron-electron interaction mediated by phonons [1, 2, 3]. These collective ground states are often found to coexist or compete for electronic energy states [4, 5]. For example, materials that present the interplay between SC and CDW include the single element actinide α -U [10], layered transition-metal chalcogenides, such as NbSe_3 [6], $2H\text{-TaSe}_2$ [7], $1T\text{-TaS}_2$ [8] and $1T\text{-TiSe}_2$ [9], the $A15$ compounds V_3Si [11] and Nb_3Sn [12], and even the cuprate high-temperature superconductors [13]. The interplay of SC and SDW order is, however, more difficult to identify, as it will be explained in the following sections. It was first observed in the quasi-1D organic substance $(\text{TMTSF})_2\text{ClO}_4$ (Bechgaard salts) at ambient pressure [14]. The heavy fermion superconducting compound URu_2Si_2 presents a large anomaly in the specific heat at 17.5 K which has been associated with the formation of a SDW

[15], although its order parameter has not been identified yet (“hidden order” phase) [16]. Recently, a new class of high-temperature iron-based superconductors has been discovered, in which superconductivity emerges when a SDW phase is suppressed with the chemical substitution or the application of pressure (see the Bibliography presented in Chapter IV).

The following Sections will briefly describe the main properties that characterize the superconducting, magnetic and density-waves ground states, which will serve as the background needed to interpret the results of the experiments presented in Chapters III and IV.

I.A Electronic Properties of Metals

I.A.1 Fermi Liquid Theory

At the beginning of the last century, Drude formulated the free electron model to describe the properties of metals [17]. In this model, the valence electrons of the atoms in a metal are described as a gas of non-interacting conduction electrons. They are non-interacting in the sense that no forces are assumed to act between the particles, or between the particles (electrons) and the positively charged ions of the lattice. In this context, the electrons of this gas travel ballistically (in straight lines) until they collide elastically with one another. The Drude model is successful in calculating the resistivity of different metals at room temperature, via the well-known Ohm’s law: $\rho = \frac{m_e}{ne^2\tau}$, where τ is the characteristic time between collisions, and is defined as the mean free path distance divided by the average velocity of the electrons. In Drude’s time, it was reasonable to assume that the electronic velocity distribution was given in equilibrium at a temperature T by the Maxwell-Bolzmann distribution. This leads to good agreement with the resistivity values measured at room temperature, and with the Wiedermann-Franz law of thermal conductivity, but also predicts a contribution to the specific heat of a metal of $3/2k_B$ per electron that was not observed for all T . The success of

the Drude model in predicting the Wiedemann-Franz law is a consequence of the cancelation of two errors: at room temperature, the actual electronic specific heat is 100 times smaller than the Drude's prediction, but the velocity of the particles taken into account is 10 times larger. This problem was solved by replacing the Maxwell-Bolzmann distribution with the Fermi-Dirac distribution function, which takes into account Pauli exclusion principle. Under this model, the average velocity of the electrons is replaced by the Fermi velocity, and this substitution gives us a good representation of the free electron gas in a wide range of temperatures, in good agreement with the experiments. The Sommerfeld theory has problems in describing the properties of some metals at low temperature. For example, it accounts reasonably well for the size of the term linear in T in the low temperature specific heat of the alkali metals (Li, Na, K, etc, all with ns^1 electronic configuration), but very poorly for transition metals such as Fe and Mn, and much worse for Bi and Sb (poor metals) [18].

Landau's Fermi liquid theory treats this problem, introducing the concept of quasiparticle. Fermi liquids have spin 1/2 excitations and obey Fermi statistics, and applies to liquid ${}^3\text{He}$, electrons in metals and heavy nuclei. For electrons in a metal, we imagine that each electron collects around itself a "screening cloud" of other electrons, thereby becoming a "quasiparticle" with some effective mass m^* . The number of quasiparticles is equal to the number N of free electrons in the metal; like them, the quasiparticles occupy plane wave states of momentum $\mathbf{p} = \hbar\mathbf{k}$ and spin projection $\pm 1/2$, and must obey the Pauli exclusion principle. Consequently, in the ground state, the quasiparticles fill the Fermi sea up to the Fermi momentum, but the energy of a single quasiparticle state is now $\varepsilon_{(p)} = \frac{p^2}{2m^*}$. The quasiparticles are associated with low-energy excitations of the interacting system of electrons with a long lifetime near the Fermi energy, and hence it was created to explain the low-temperature ($T \ll T_{Fermi}$) properties of a Fermi system. The predictions for the temperature dependence of the magnetic susceptibility χ [17, 19], specific heat C [19] and electrical resistivity ρ [20] at low temperatures

($T \sim 1 - 10$ K, $T \ll T_{Fermi}$) in the Fermi liquid scenario for an isotropic, 3-dimensional system, are given by

$$\chi = \chi_0, \quad \chi_0 = \chi_0(m^*) \quad (\text{I.1})$$

$$C = \gamma_0 T, \quad \gamma_0 = \gamma_0(m^*) \quad (\text{I.2})$$

$$\rho = \rho_0 + A T^2, \quad A = A(m^*) \quad (\text{I.3})$$

where ρ_0 is the residual resistivity. The prediction for the electrical resistivity is very difficult to observe in most normal metals, provided that the contribution ρ_0 due to impurities in the samples at low temperatures is in general very large and the coefficient A is too small. In recent years, experiments performed on a new class of materials called heavy fermions allowed us to confirm the Fermi liquid resistivity law.

The Fermi liquid theory does not take into account other effects from the lattice, such as the electron-phonon interaction, or the effect of magnetic impurities. In general, a better description of the temperature dependence of the electrical resistivity in the absence of magnetic impurities is given by the Bloch-Grüneisen formula:

$$\rho = \rho_0 + A \left(\frac{T}{\Theta} \right)^n \int_0^{\frac{\Theta}{T}} \frac{x^n}{(e^x - 1)(1 - e^{-x})} dx, \quad (\text{I.4})$$

where Θ is the Debye temperature, and n is an integer that depends upon the nature of the interaction ($n = 2$ implies electron-electron interaction, $n = 5$ implies electron-phonon scattering).

I.A.2 Heavy Fermions

Heavy fermion (HF) materials are intermetallic compounds that usually contain a rare earth or actinide atom (U, Ce, Yb, e.g. URu₂Si₂ is a HF superconductor below $T_c = 1.5$ K) that has a partially filled 4f or 5f electron shell. At low temperatures, the f-electrons couple strongly to the conduction band which results in enhancements of the effective mass m^* to values 100 – 1000 times larger

than the electron mass. As a consequence of this, $\gamma_0(m^*)$, $\chi_0(m^*)$ and $A(m^{*2})$ are also enhanced. For example, a regular metal has $\gamma_0^{metal} \sim 1 - 10 \frac{mJ}{molK^2}$, while, for a heavy fermion metal, $\gamma_0^{HF} \sim 100 - 1000 \frac{mJ}{molK^2}$.

It is also worth to mention that there is a universal relation between the large magnitude of A and the enhanced electronic specific heat coefficient γ_0 in heavy fermions materials, as was found by Kadowaki and Woods [21]. They observed that most of heavy-fermion compounds obeyed the relation $A/\gamma_0^2 = 1 \times 10^{-5} \mu\Omega\text{cm} (molK/mJ)^2$.

I.A.3 Magnetism in Metals

Magnetism in materials is usually attributed to unpaired spins in partially filled d - or f -electron orbitals of ions, but it can also arise from conduction electrons in a metal. The way these ionic orbitals populate is defined by Hund's rules: 1*st*, maximize the total spin angular momentum S to minimize the Coulomb energy because of the Pauli exclusion principle; 2*nd*, maximize the total orbital angular momentum L , which also minimizes Coulomb repulsion; and 3*rd*, find the total angular momentum J using $J = |L - S|$ if the shell is less than half-full and $J = |L + S|$ if the shell is more than half-full, to minimize spin-orbit energy. The effective magnetic moment of an isolated ion obtained from Hund's rules is given by

$$\mu_{eff} = g_J \mu_B \sqrt{J(J+1)}, \quad (\text{I.5})$$

$$g_J = 1 + \frac{J(J+1) + S(S+1) - L(L+1)}{2J(J+1)}, \quad (\text{I.6})$$

where μ_B is the Bohr magneton and g_J is the Landé g -value. The predictions of the magnetic ground state given by Hund's rules are very precise with isolated magnetic moments from localized f -shells, although it disagrees with experiments when the free-ion approximation fails, for example, due to the effects of crystalline electric fields (CEF) or to Kondo screening of the magnetic moments by conduction electrons. P. W. Anderson [22] formulated a more complete description, using a

Hamiltonian of the form:

$$\mathcal{H}_A = \sum_{k,\sigma} \varepsilon_k c_{k\sigma}^\dagger c_{k\sigma} + \sum_{m,\sigma} \varepsilon_m c_{m\sigma}^\dagger c_{m\sigma} + U c_{m\uparrow}^\dagger c_{m\uparrow} c_{m\downarrow}^\dagger c_{m\downarrow} + \sum_{k,m,\sigma} \left(V_{km} c_{m\sigma}^\dagger c_{m\sigma} + V_{km}^* c_{m\sigma}^\dagger c_{m\sigma} \right) \quad (\text{I.7})$$

where σ can be for spin $+1/2$ (\uparrow) or $-1/2$ (\downarrow). The first term corresponds to the free conduction electron contribution (labeled by k), with energy states separated by ε_k from the Fermi level. The second term accounts for the magnetic states (labeled by m), *i.e.*, from $3d$, $4f$ or $5f$ levels, with energy states separated by ε_m from the Fermi level. The third term is the Coulomb repulsion U between magnetic orbitals. The fourth term describes the hybridization between conduction and magnetic electron states, with coupling constant V_{km} , and allows the localized electrons to hop into the conduction electron states. The hybridization between d - or f -electrons with conduction electron bands produces a broadening of the d - or f -magnetic level according to Fermi's Golden Rule, with a width $\Delta \sim \pi N(E_F) \langle V_{km}^2 \rangle$, where $N(E_F)$ is the conduction band density of states per spin at the Fermi energy E_F . The Anderson scenario leads to a criterion for local moment formation: if the lower (upper) magnetic m -level lies below (above) the Fermi energy by an amount greater than the broadening Δ , then local moments can form. If the hybridization is not too strong, Schrieffer and Wolff [23] showed that the Anderson Hamiltonian \mathcal{H}_A reduces to the exchange Hamiltonian $\mathcal{H}_{ex} = -2JS_k \cdot S_m$ for an antiferromagnet, where $J \sim -\frac{\langle V_{km}^2 \rangle}{\varepsilon_m}$ for the limit of very strong hybridization, $U \rightarrow \infty$. The magnitude and presence of these local and/or itinerant moments is responsible for behaviors such as magnetic susceptibility, magnetic ordering, and the Kondo effect. A more complete picture, which includes the orbital angular momentum is given by the Coqblin-Schrieffer model [24].

I.A.4 RKKY Interaction and the Kondo Effect

Two sufficiently close magnetic impurity ions in a metal can couple via the conduction electron spin polarization through the oscillatory long-range Rudermann-

Kittel-Kasuya-Yosida RKKY interaction [25, 26, 27]:

$$J_{RKKY} \propto -J^2 N(E_F) \frac{\cos(2k_F r)}{|k_F r|^3} \quad (\text{I.8})$$

where r is the position in real space. Oscillations in the charge density in non-magnetic metallic alloys are also produced by a similar mechanism, and are known as Friedel oscillations [28]. The RKKY interaction provides an important mechanism for magnetic coupling between localized electronic moments in metals, and it can give rise to either FM or AFM coupling between neighboring impurities, depending on the separating distance between the two moments.

For non-magnetic metals, such as Cu or Au, the electrical resistivity decreases as temperature is decreased, as it was explained in previous sections. In the presence of small amounts of magnetic impurities, such is the case of an alloy of Au with less than 0.02% of Fe, an upturn in the resistivity below 10 K was observed [29], and with the position of the minimum depending on the impurity concentration. After three decades of investigation, a theoretical description of the resistance minimum was finally developed by J. Kondo in 1964 [30], using the exchange Hamiltonian as a starting point. Kondo computed the magnetic resistivity up to third order in J , obtaining:

$$\rho(T) \propto \rho_0 + AT^n - \rho_K \ln\left(\frac{T}{T_K}\right) \quad \text{for } T \gg T_K \quad (\text{I.9})$$

where the first two terms correspond to the Fermi-liquid predictions for an electron-electron and electron-phonon interacting system, and the third term is the Kondo term, with ρ_K depending on the impurity concentration x . The position of the minimum was then found to be $T_{min} = \left(\frac{\rho_K T_K}{nA}\right)^{\frac{1}{n}}$, so for a leading electron-phonon scattering, $n = 5$ and $T_{min} \propto x^{\frac{1}{5}}$. The upturn in the electrical resistivity is a result of the enhanced scattering occurring when the conduction electrons form a cloud of opposite spin polarization around the magnetic impurity spin, resulting in a quasi-bound state which screens the impurity magnetic moment. A Kondo temperature is defined by:

$$T_K \sim T_F e^{-\frac{1}{|JN(E_F)|}} \quad (\text{I.10})$$

which separates the non-magnetic low- T behavior, where $\chi(T)$ saturates to a constant value, from the high- T behavior, where the magnetic susceptibility $\chi(T)$ follows a Curie-Weiss law of the form $\chi \propto (T - \Theta_{CW})^{-1}$, where $\Theta_{CW} \approx T_K/3$ is approximately equal to the ferromagnetic (FM) ordering Curie temperature T_C or the antiferromagnetic (AFM) ordering Néel temperature T_N , depending on its sign. The Kondo temperature is an energy scale that characterizes the Kondo system, rather than a transition temperature. It can be estimated from the electrical resistivity, not as the minimum, but as the temperature at which it deviates from the logarithmic behavior (the phonon contribution must first be subtracted from the total electrical resistivity). The above description is only valid for $T \gtrsim T_K$, since the magnetic resistivity diverges for $T \ll T_K$, so the total electrical resistivity saturates to a value proportional to $1 - \xi(T/T_K)^2$, where ξ is a constant that depends on the total spin of the magnetic impurity.

In some heavy-fermion compounds, particularly those based on Ce or Yb, high concentrations of magnetic ions lead to an effect known as “Kondo coherence”. A downturn is observed at intermediate temperatures rather than a minimum and a $\ln T$ increase. As temperature is lowered, the interaction between magnetic ions becomes important, and the scattering of conduction electrons becomes coherent, resulting in an overall decrease of the resistivity [31].

I.A.5 The Doniach Diagram, Quantum Critical Points and Non-Fermi Liquid Behavior

The competition between the Kondo effect on each atom, which tends to suppress the magnetic moment with decreasing temperature, and the RKKY interaction, which, on the contrary, tends to give a magnetic ordering between different rare-earth atoms is described by the well-known “Doniach diagram” [32], as shown in Fig. I.1. It describes the competition between the RKKY interaction and the Kondo screening of the magnetic moments in terms of a “tuning” parameter, $|JN(E_F)|$. The Néel temperature (or the Curie temperature in few cases),

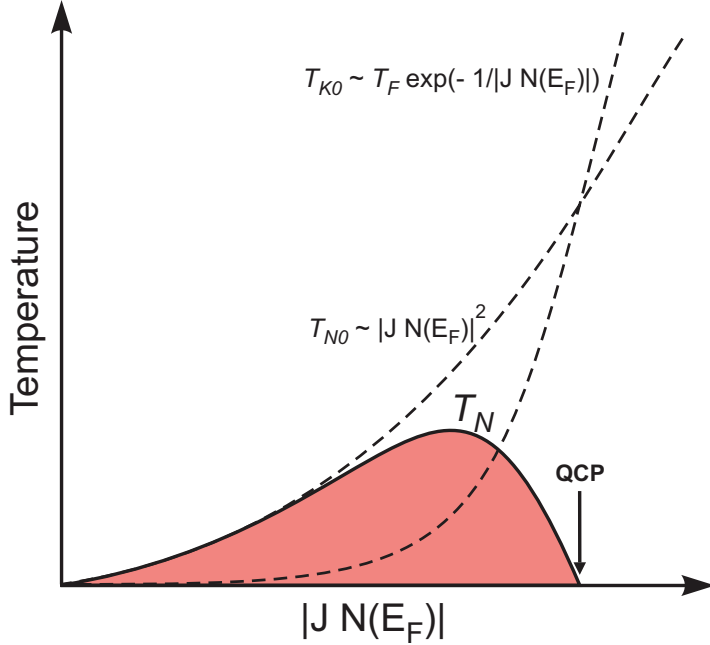


Figure I.1: The Doniach phase diagram, in which the Kondo and the RKKY energy scales compete as a function of the tuning parameter $|JN(E_F)|$, where J is the exchange coupling constant, and $N(E_F)$ is the density of electronic states at the Fermi energy level. The colored region represents a magnetically ordered phase below the Néel temperature T_N . At the critical value of the tuning parameter, T_N is suppressed to 0 K, and quantum fluctuations become important.

in the case that no Kondo effect is present, has the form $T_{N0} \propto |JN(E_F)|$, while the Kondo temperature for a single impurity $T_{K0} \propto \exp[-1/|JN(E_F)|]$. For small values of $|JN(E_F)|$, T_{N0} is larger than T_{K0} and the system tends to order magnetically, usually with a reduction of the magnetic moment due to the Kondo effect. On the other hand, for large values of $|JN(E_F)|$, T_{K0} is larger than T_{N0} and the system tends to become non-magnetic and does not order magnetically. The actual Néel temperature T_N increases first with $|JN(E_F)|$, and reaches a maximum, after which is suppressed to zero at a critical value of $|JN(E_F)|$ (colored region in Fig. I.1). This zero-temperature point at the critical $|JN(E_F)|$ is usually referred as the quantum critical point (QCP). Above this QCP, only quantum fluctuations

are possible (instead of the thermal fluctuations that usually drive classical phase transitions), for which the relevant length and time scales are coupled via the uncertainty principle. A complete review of magnetic quantum critical points can be found in Ref. [33]. This behavior is found in many *f*-electron compounds, when a second order phase transition is suppressed to 0 K at a critical $|JN(E_F)|$ tuning parameter, which is usually pressure (P_c), magnetic field (H_c) or chemical composition (x_c). For example, both CeIn₃ and CePd₂Si₂ exhibit AFM order with a Néel temperature of the order of 10 K at ambient pressure, and the application of external pressure suppresses T_N smoothly to 0 K at $P_c \approx 2.8$ GPa [49]. In some cases, such in this two previous examples, a superconducting phase emerges in the form of a dome above the QCP. In the region above the QCP, quantum fluctuations can affect the physical properties of a system at finite but usually low temperatures, and this breakdown of the Fermi liquid properties is called “non-Fermi liquid” behavior (NFL) [50]. The NFL system is characterized by weak power-law or logarithmic temperature dependences of the physical properties, and can be summarized as follows:

$$C(T)/T \sim -\ln T \text{ or } -T^a \text{ or } T^{-a}, \quad (\text{I.11})$$

$$\chi(T) \sim -\ln T \text{ or } T^{-a}, \quad (\text{I.12})$$

$$\rho(T) \sim \rho_0 + A'T^n, \quad (\text{I.13})$$

where usually $a < 1$ and $n < 2$ [51]. A number of models have been developed to explain the origin of NFL behavior. The underlying bases for these models revolve around one or a combination of three principal themes: a) multichannel Kondo models, b) disorder that can induce a distribution of Kondo temperatures, and c) vicinity to a $T = 0$ K phase transition (QCP) [51]. There is a large number of materials in which the NFL properties occurs far away from the QCP, for which the “classic” V-shaped QCP picture fails [34], and for which an specific treatment must be utilized to describe them.

I.B Superconductivity

Exactly 100 years ago, H. Kamerlingh Onnes and his assistant Gilles Holst in Leiden discovered that the electrical resistivity of mercury dropped to zero at $T_c = 4.15$ K [35], few years after helium was first liquefied in the same laboratory in Leiden. Shortly thereafter, the same effect was found in indium (3.4 K), tin (3.72 K) and in lead (7.19 K). In the 50's, superconductivity in the A15 compounds was found and higher T_c 's appeared up to ~ 20 K in Nb_3Ge [36]. In 1986, Bednorz and Müller found superconductivity in $(\text{La},\text{Sr})_2\text{CuO}_4$ with $T_c = 36$ K [37], which set a new record and the beginning of the high-temperature cuprate superconductor era. Values of T_c up to 160 K were found in $\text{HgBa}_2\text{Ca}_2\text{Cu}_3\text{O}_8$ at high pressures [38]. Very recently, high-temperature superconductivity was found in Fe-based compounds, with T_c 's as high as 55 K in $\text{SmFeAsO}_{1-x}\text{F}_x$ [39], where magnetism from Fe and rare-earth atoms competes with the superconducting state. Fig. I.2 displays the evolution of the superconducting critical temperature T_c throughout the years. Superconductors not only can transport electrical current without dissipation, but also they expel the magnetic field from their interior, that is, they are perfect diamagnets. This effect is known as the Meissner effect, after the discovery by W. Meissner and R. Ochsenfeld in 1933 [40]. Superconductors can then be classified in two categories: type-I superconductors, if the magnetic field is *completely* displaced from the interior of the material, or type-II, if the material allow partial penetration of magnetic flux.

The superconducting state was first described by the London brothers in 1935 [42] using electrodynamic relations

$$\begin{aligned}\vec{E} &= \frac{\partial}{\partial t}(\Lambda \vec{j}_s) \\ \vec{H} &= -\frac{\partial}{\partial \vec{r}} \times (\Lambda \vec{j}_s)\end{aligned}\tag{I.14}$$

where $\Lambda = 4\pi\lambda^2/c^2 = m/n_s e^2$, \vec{j}_s is the supercurrent density and n_s is the density of superconducting carriers. The first equation says that the charge in a superconductor accelerates without resistance when an electric field is applied, while the

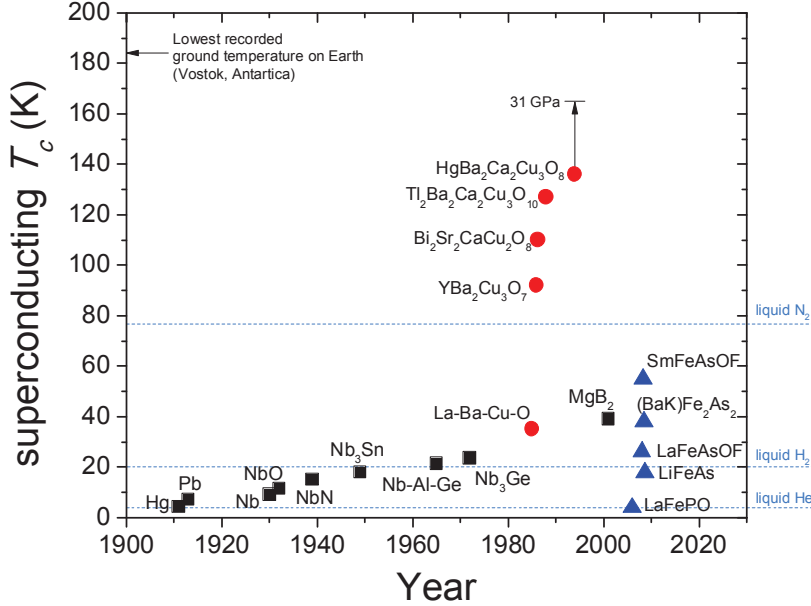


Figure I.2: Evolution of the superconducting transition temperature T_c for different materials throughout the years.

second equation gives, using $\vec{H} = 4\pi\vec{j}/c$:

$$\nabla^2 \vec{H} = \frac{\vec{H}}{\lambda^2} \quad \rightarrow \quad H(x) = H_0 e^{-x/\lambda} \quad (\text{I.15})$$

which indicates that the magnetic field is screened inside the material at a characteristic distance λ . The parameter λ is denoted “penetration length”, and it is inversely proportional to the density of superconducting carriers n_s .

According to the Ginzburg-Landau (GL) theory of second order phase transitions [43], there is a thermodynamic quantity called the “order parameter” which is zero above T_c , and becomes continuously non-zero below T_c . The complex order parameter is defined as

$$\Delta = |\Delta| e^{i\phi} \quad (\text{I.16})$$

which is related with the density of superconducting carriers via $n_s = |\Delta|^2$, which gives Eq. I.16 a macroscopic character that describes the superconducting state in the interior of the material. The parameter ξ is called the “coherence length”,

and it corresponds to the characteristic length of the fluctuations of $|\Delta|$. The Ginzburg-Landau parameter $\kappa \equiv \lambda/\xi$ is associated to the surface energy at the interface between the normal and the superconducting material. If $\kappa^2 > 1/2$, that energy is positive and the superconducting state disappears continuously at the critical field line $H_c(T)$, as occurs in type-I superconductors. On the other hand, if $\kappa^2 < 1/2$, the surface energy is negative, and normal-state domains form inside the superconducting state. This “mixed” state is characteristic of the type-II superconductors, in which a Meissner region exists below the critical field curve $H_{c1}(T)$, as in the type-I materials, and in the region delineated by $H_{c1}(T)$ and the upper critical field line $H_{c2}(T)$, the wave function of the superconducting state is modulated, the mixed state develops, and magnetic field penetrates the material through normal domains of the form of tubes of magnetic flux called “vortices”, each of them carrying a quantum of magnetic flux $\Phi_0 = hc/2e = 2.07 \times 10^{-7}$ gauss, where h is the Planck’s constant, c is the speed of light in vacuum, and e is the charge of the electron. Above $H_{c2}(T)$, the superconducting state is destroyed, and the material becomes continuously normal. These flux quanta have a core of radius equal to the coherence length ξ , around which superconducting currents extend to a distance of the order of the penetration length λ . Abrikosov [44] described the system of vortices as a lattice of triangular symmetry, which formed due to the repulsive magnetic interaction between the magnetic flux quanta. A single element type-I superconductor has a Ginzburg-Landau parameter κ of the order of 0.1, while for a “low-temperature” type-II superconductor, such as Nb, $\kappa \sim 2$. The cuprate high-temperature superconductors are characterized by large values of the Ginzburg-Landau parameter κ , reaching values of the order of 100.

The first microscopic theory of superconductivity appeared in 1957, developed by Bardeen, Cooper and Schrieffer (BCS) [1]. The paper they presented showed calculations of the temperature dependence of the energy gap, thermodynamic critical field, specific heat, coherence length, penetration length, ultrasonic attenuation, and nuclear relaxation rate. The central idea of the BCS theory is

that even a weak attraction can bind pairs of electrons into a bound state (“Cooper pairs”), showing that the Fermi sea of electrons is unstable against the formation of bound pairs, regardless of how weak the interaction is, as long as it is attractive. The mechanism they proposed for the attractive interaction was based in an electron-phonon interaction that overcomes the repulsive Coulomb interaction between electrons, where an electron positively polarizes the ionic lattice, attracting a second electron. This prediction was later confirmed experimentally with the verification of the isotope effect. The pairing obtained by this mechanism requires that the electrons forming the Cooper pairs have opposite spin and momentum ($\vec{p}\uparrow, -\vec{p}\downarrow$), that is, the electrons form a spin-singlet *s*-wave pair.

The BCS paper presented a brilliant ansatz for the wave functions of the ground state and the excited states. In the BCS ground state, the Cooper pairs form a condensate, and open an isotropic gap at the fermi level. The authors showed that the single-particle energy gap represents the amplitude of the order parameter, $|\Delta|$, and it relates to the critical temperature with the relation $2\Delta = 3.52k_B T_c$, where k_B is the Boltzmann constant.

The Cooper pairs of a BCS superconductor can be broken via Zeeman interaction of the form $\vec{s} \cdot \vec{H}$ when an external magnetic field \vec{H} is applied to the sample or when magnetic moments $\vec{\mu}$ of magnetic impurities are present inside the sample, or via the interaction of the vector potential \vec{A} associated with \vec{H} or $\vec{\mu}$ with the momentum \vec{p} of the electrons ($\vec{p} \cdot \vec{A}$ term in the Hamiltonian). Both of these interactions raise the energy of one of the electrons of the pair and lowers the energy of the other, producing the “pair breaking” mechanism that suppresses T_c . The rapid suppression of T_c with paramagnetic impurity concentration give rise to unexpected phenomena, such as gapless superconductivity, and reentrant superconductivity associated with the Kondo effect [45]. In 1958, Matthias, Suhl and Corenzwit [46] carried experiments where T_c was suppressed linearly with the magnetic impurity concentration. It was found that the depression of T_c scaled well with the de Gennes factor $\mathcal{G}_J = (g_J - 1)^2 J(J + 1)$ of the rare-earth impurity.

Abrikosov and Gor'kov (AG) showed that, for magnetic impurities that break time-reversal symmetry, the critical temperature and the energy gap are strongly depressed owing to a change in the BCS density of states [47].

The term “unconventional superconductivity” is applied to superconducting materials that violate some of the properties expected from the BCS theory. High-temperature superconductors, heavy-fermion superconductors and magnetic superconductors are some examples of materials that present unconventional superconductivity. Heavy-fermion compounds have T_c 's of the order of 2 K, and the superconducting state often coexists with antiferromagnetic order, with a T_c smaller than the Néel temperature T_N . At temperatures well below T_c , the superconducting properties usually present power-law temperature dependences rather than exponential dependences, which provide evidence of anisotropic superconductivity (as opposed to an isotropic gap). In these materials, the mechanism that provides the “glue” for the Cooper pairs is different than the electron-phonon mechanism, and there is evidence of superconductivity mediated by magnetic dipole or even electric quadrupole excitations. In the recently discovered Fe-based superconductors, coexistence of spin-density waves (SDW, see Section I.C.2) and superconductivity has been observed, where the SDW-like AFM state involves the d -electrons of the Fe sublattice [48]. There is also evidence that spin fluctuations are responsible for the pairing mechanism of electrons on different Fermi surface sheets, giving an unconventional $d\pm$ -type of pairing.

I.C Charge- and Spin-Density Waves in Low Dimensional Systems

There is a large variety of low-dimensional materials that are possible to study in the laboratory, such as the type of one-dimensional (1D) inorganic chain $K_2Pt(CN)_2Br_{0.33}H_2O$ (Krogmanns salt or KCP), which become metallic due to charge transfer from the bromine-water reservoirs, or the organic linear chains

like $(\text{TMTSF})_2\text{PF}_6$ which is a metallic member of the Bechgaard salts, and the quasi-1D metals such as the transition metal chalcogenides. As mentioned at the beginning of this Chapter, these systems present a wide variety of competing ground states, such as superconductivity, magnetism and spin- and charge-density waves among others, which can be accessed by tuning the structure, or applying magnetic field or pressure. In these low-dimensional materials, the electrons are confined along the chains. It is easy to imagine that the electrons have less space to move freely, so they have to interact more with the lattice or other electrons, via Coulomb or magnetic interactions. The reduction of phase space in low dimensional systems has important consequences. In one dimension, the dispersion relation of a Fermi gas is simply $\varepsilon_{(k)} = \frac{\hbar^2 k^2}{2m}$, and the Fermi surface is very simple, consisting of only two points at $\pm k_F$. In the framework of linear response theory [2], the rearrangement of the density of charge $\rho^{ind}(\vec{q})$ of the electron gas in the presence of a time independent potential $\Phi(\vec{q})$ can be studied via a response function $\chi(\vec{q})$ through the expression

$$\rho^{ind}(\vec{q}) = \chi(\vec{q})\Phi(\vec{q}), \quad (\text{I.17})$$

with

$$\rho^{ind}(\vec{r}) = \int_q \rho^{ind}(\vec{q}) e^{i\vec{q}\cdot\vec{r}} d\vec{q} \quad (\text{I.18})$$

$$\Phi(\vec{r}) = \int_q \Phi(\vec{q}) e^{i\vec{q}\cdot\vec{r}} d\vec{q} \quad (\text{I.19})$$

$$\chi(\vec{q}) = \int \frac{d\vec{k}}{(2\pi)^d} \frac{f_k - f_{k+q}}{\varepsilon_k - \varepsilon_{k+q}} \quad (\text{I.20})$$

where q is the momentum transfer and $f_k = f(\varepsilon_k)$ is the Fermi distribution function. In one dimension, assuming a linear dispersion relation $\varepsilon_k = \varepsilon_F + \hbar v_F(k - k_F)$ for values of k in the vicinity of the only two points of the Fermi energy that are separated by $2k_F$, the last integral gives:

$$\chi(\vec{q}) = -e^2 n(\varepsilon_F) \ln \left| \frac{q + 2k_F}{q - 2k_F} \right|. \quad (\text{I.21})$$

Clearly, the response function of a 1D-electron gas diverges at $q = 2k_F$, as it is displayed in Fig. I.2a. As a consequence, in 1D an external perturbation leads to a

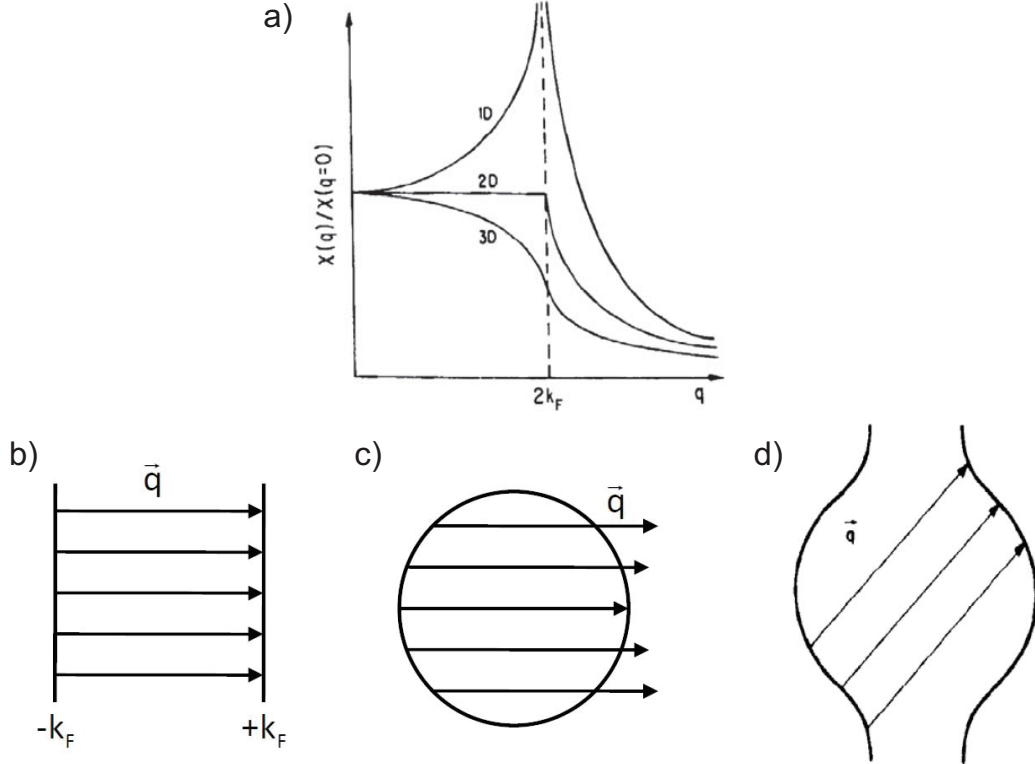


Figure I.3: (a) Response function χ as a function of wavevector q for a one-, two-, and three-dimensional free electron gas at $T = 0$. (b – d) Fermi surface topology for a 1D, 2D and quasi-1D electron gas. The arrows indicate pairs of states, one full, one empty, differing by the wavevector $q = 2k_F$ (from Ref. [2]).

divergent charge redistribution, and due to the definition of $\rho^{ind}(\vec{r})$ [52], the electron gas itself is unstable with respect to the formation of a *periodically* varying electron charge or spin density. The period of the “density wave” is given by $\lambda_0 = \frac{\pi}{k_F}$. The divergence of the response function at $q = 2k_F$ is due to a particular topology of the Fermi surface, called *perfect nesting*. Looking at Eq. I.20, the most significant contribution to the integral come from pairs of states which differ by $q = 2k_F$ and have the same energy (Fig. I.3b), thus giving a divergent behavior of Eq. I.21. In more than one dimension, the number of such states is highly reduced, leading to a removal of the singularity at $q = 2k_F$. However, it is possible to find special cases where the perfect nesting condition is also satisfied for some states. In Fig. I.3c is

shown the case of a 2D electron gas, and Fig. I.3d shows the case of a quasi-one-dimensional gas, where pairs of states are connected in some particular direction. Since the number of connected states is reduced in higher dimensional systems, the divergence of the response function is suppressed to a soft step in higher dimensions (Fig. I.3a), and the gapping of the Fermi surface is not complete, as is found in highly anisotropic quasi-1D or 2D materials.

In 1D, $\rho^{ind}(\vec{q})$ reflects the formation of pairs of particles (electron-electron or electron-hole). In mean field theory, the selection rules then connect the electron and hole states give only four possible configurations, two with $q = 0$, for a front-scattering process (*i.e.* $\vec{k}_2 = -\vec{k}_1$), and two with $q = 2k_F$, for a back-scattering process (*i.e.* $\vec{k}_2 = \vec{k}_1 = \vec{k}_F$), resulting in four possible channels:

$$\begin{array}{lll}
 e_{\rightarrow}, +\sigma ; e_{\leftarrow}, -\sigma & \left\{ \begin{array}{ll} q = 0 \\ S = 0 \end{array} \right. & (\text{singlet } SC) \\
 e_{\rightarrow}, +\sigma ; e_{\leftarrow}, +\sigma & \left\{ \begin{array}{ll} q = 0 \\ S = 1 \end{array} \right. & (\text{triplet } SC) \\
 e_{\rightarrow}, +\sigma ; h_{\leftarrow}, +\sigma & \left\{ \begin{array}{ll} q = 2k_F \\ S = 0 \end{array} \right. & (CDW) \\
 e_{\rightarrow}, +\sigma ; h_{\leftarrow}, -\sigma & \left\{ \begin{array}{ll} q = 2k_F \\ S = 1 \end{array} \right. & (SDW)
 \end{array} \tag{I.22}$$

Depending on the nature of the electron-electron and electron-phonon interactions, it is possible to have either a superconducting ground state or a density-wave ground state. This is usually modeled using two coupling constants, with the order parameter being a combination of the two, and with the possible ground state depending on their mixture [53].

The various broken symmetry ground states have several common characteristics. For all condensates, the order parameter is complex, and can be written as in Eq. I.16. The amplitude $|\Delta|$ can be defined as the single particle gap. For the superconducting ground states, gauge symmetry is broken, since the phase is invariant under gauge transformation. For the density wave ground states, the

translational symmetry is broken. This difference leads to different collective excitations and also to differences in the coupling constants. For a superconductor, the collective excitations are called *bogoliubons* (due to the Bogoliubov-Valatin transformation that diagonalizes the BCS Hamiltonian). For charge and spin density waves, the collective excitations are called *phasons* and *amplitudons*. For the SDW ground state, the spin rotational symmetry is also broken, leading to additional collective excitations called *magnons*, similar to those of the antiferromagnets.

I.C.1 Charge-density waves

The formation of charge-density waves (CDW) is due to the electron-phonon interaction, and the Hamiltonian that describes it in one dimension is known as the Frölich Hamiltonian:

$$\mathcal{H}_{CDW} = \mathcal{H}_{el} + \mathcal{H}_{ph} + \mathcal{H}_{el-ph}. \quad (\text{I.23})$$

The first term corresponds to the free electron gas,

$$\mathcal{H}_{el} = \sum_k \varepsilon_k a_k^\dagger a_k, \quad \varepsilon_k = \frac{\hbar^2 k^2}{2m}, \quad (\text{I.24})$$

with the well known quadratic energy dispersion relation ε_k . The lattice term is basically the sum of the harmonic oscillators associated with each lattice normal mode (phonons), which can be written in the second-quantized form:

$$\begin{aligned} \mathcal{H}_{ph} &= \sum_k \left(\frac{P_q P_{-q}}{2M} + \frac{M\omega_q^2}{2} Q_q Q_{-q} \right) = \sum_q \hbar\omega_q \left(b_q^\dagger b_q + \frac{1}{2} \right), \\ u_q(x) &= \sum_q \left(\frac{\hbar}{2NM\omega_q} \right)^{1/2} (b_q + b_{-q}^\dagger) e^{iqx}, \end{aligned} \quad (\text{I.25})$$

where $u_q(x)$ are the lattice displacement which clearly depends on the phonon mode q . The electron-phonon interaction term connects pairs of states k and k' via the electron-phonon potential V , which plays the role of the external potential that rearranges the charge distribution in the linear response theory:

$$\mathcal{H}_{el-ph} = \sum_{k,k',l} \langle k | V(r - l - u_q) | k' \rangle a_{k+q}^\dagger a_k. \quad (\text{I.26})$$

For small lattice distortion, \mathcal{H}_{el-ph} is reduced to two terms: the first one corresponds to the Bloch term, which is responsible for opening the gap at the Brillouin zone boundaries, and which can be neglected since it is far away from the Fermi surface edges; the second term can be written in this form (after performing some algebra):

$$\mathcal{H}_{el-ph} \simeq \sum_{k,q} g_q (b_{-q}^\dagger + b_q) a_{k+q}^\dagger a_k, \quad g_q = i \left(\frac{\hbar}{2NM\omega_q} \right)^{1/2} |q| V_q \quad (\text{I.27})$$

where the electron-phonon coupling constant g_q is introduced, which depends on the mass of the ions (*isotope effect*). The transition to the CDW state occurs when the vibrations of the lattice “freeze” in a particular mode, with $q = 2k_F$, and $\langle b_{2k_F} \rangle = \langle b_{-2k_F}^\dagger \rangle$. This effect is known as the Kohn anomaly, and can be seen as an energy *softening* in the phonon dispersion [54]. The order parameter of the phase transition is then defined in term of this particular phonon mode:

$$|\Delta| e^{i\phi} = g \left(\langle b_{2k_F} \rangle + \langle b_{-2k_F}^\dagger \rangle \right) \quad (\text{I.28})$$

where the amplitude Δ corresponds to the gap opening at the fermi surface. With the order parameter defined in this way, it is possible to express the transition temperature to the CDW state in the mean-field form

$$k_B T_{CDW}^{MF} = 1.14 \varepsilon_0 e^{-1/\lambda}, \quad \lambda_{CDW} \equiv \frac{g^2 n(\varepsilon_F)}{\hbar \omega_{2k_F}}, \quad (\text{I.29})$$

where in the expression for λ is contained the electron-phonon coupling constant g and the density of states at the Fermi level, $n(\varepsilon_F)$. The gap Δ and T_{CDW} are related via the familiar BCS-like expression:

$$2\Delta = 3.52 k_B T_{CDW}. \quad (\text{I.30})$$

The redistribution of charge density $\rho^{ind}(r)$ can be calculated after finding the wavefunctions of the Frölich Hamiltonian, which in the mean-field approximation gets reduced to

$$\mathcal{H}_{CDW}^{MF} = \sum_k \left[\varepsilon_k a_k^\dagger a_k + |\Delta| e^{i\phi} a_{k+2k_F}^\dagger a_k + |\Delta| e^{-i\phi} a_{k-2k_F}^\dagger a_k \right] + \frac{\hbar \omega_{2k_F} \Delta^2}{2g^2}. \quad (\text{I.31})$$

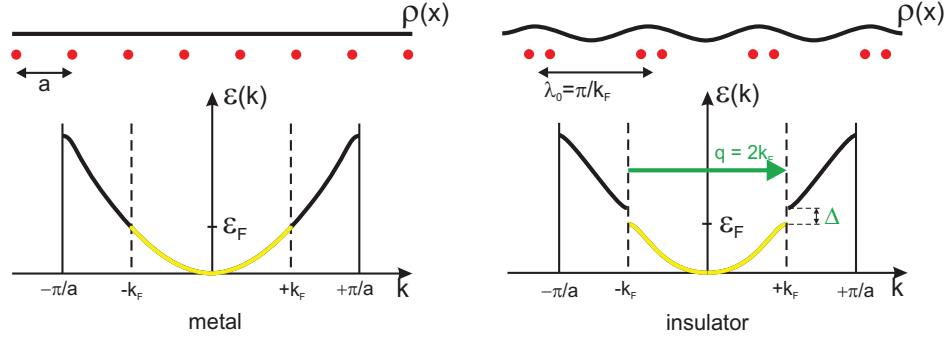


Figure I.4: The single particle band, electron density and lattice distortion in the metallic state above T_{CDW} (*left*) and in the charge density wave state at $T = 0$ (*right*) for a half-filled band.

In the nearly free electron approximation, states that are too separated from the Fermi level can be omitted, and it is possible to diagonalize this mean-field Hamiltonian by a canonical transformation. With the ground state wavefunctions, the charge-density obtained is

$$\rho^{ind}(x) = \rho_0 \left[1 + \frac{\Delta}{\hbar v_F k_F \lambda} \cos(2k_F x + \phi) \right] \quad (\text{I.32})$$

where ρ_0 corresponds to the constant electronic density in the metallic state. This charge-density redistribution produces a distortion in the ionic lattice, which brings the Brillouin zone boundaries to the Fermi surface edges, opening an energy gap Δ , which lowers the overall energy of the occupied electronic states. In one dimension, all the states at the Fermi surface are connected by $q = 2k_F$ and have the same energy (Fig. I.3b), and due to this single particle gap at the Fermi surface, the material transforms from a metal to an insulator, as it is exhibited in Fig. I.4, where the energy dispersion is drawn for a half-filled band, for which $\lambda_0 = 2a$ and the density wave is commensurate with the underlying lattice. This transition is generally referred to as the Peierls transition, since it was first suggested by Peierls in 1955 [55].

I.C.2 Spin-density waves

The formation of a spin-density wave (SDW) is due to an electron-electron interaction, and the Hamiltonian that describes it is known as the Hubbard Hamiltonian

$$\mathcal{H}_{SDW} = \sum_{k,\sigma} \varepsilon_k a_{k,\sigma}^\dagger a_{k,\sigma} + \frac{U}{N} \sum_{k,k',q} a_{k,\sigma}^\dagger a_{k+q,\sigma} a_{k',-\sigma}^\dagger a_{k'-q,-\sigma} \quad (\text{I.33})$$

which is composed of a kinetic term and the electron-electron interaction term, where U is the Coulomb interaction parameter and σ labels the spin state of the electrons. In the mean-field approximation and in the weak-coupling limit (*i.e.* $U \ll \varepsilon_F$), this Hamiltonian can be also canonically transformed to a form that can be easily diagonalized, as in the CDW case:

$$\mathcal{H}_{SDW}^{MF} = \sum_{k,\sigma} E_k \gamma_{k,\sigma}^\dagger \gamma_{k,\sigma} + \frac{2\Delta^2 N}{U}, \quad (\text{I.34})$$

where $\gamma_{k,\sigma}^\dagger$ and $\gamma_{k,\sigma}$ are the creation and annihilation operators of the SDW quasi-particles, respectively, and Δ is also defined as the amplitude of the complex order parameter, $\Delta = |\Delta|e^{i\phi}$. The system enters the SDW state below a transition temperature defined in the mean-field form similarly as in the CDW case:

$$k_B T_{SDW}^{MF} = 1.14 \varepsilon_0 e^{-1/\lambda}, \quad \lambda_{SDW} \equiv Un(\varepsilon_F). \quad (\text{I.35})$$

The Coulomb parameter U now plays the role of the electron-electron coupling constant, as can be seen from the definition of λ_{SDW} . The spin density can be calculated as

$$\langle S(x) \rangle = 2|S| \cos(2k_F x + \phi). \quad (\text{I.36})$$

The order parameter is then related to the Coulomb parameter, giving $\Delta = |\Delta|e^{i\phi} = U|S|e^{i\phi}$. Crudely speaking, the SDW ground state can be seen as two CDW states, one for the “spin up” and another for the “spin down” sub-bands, with charge density wave modulations of equal amplitude and wavevector, but differing by a phase of π , giving an overall homogeneous charge distribution plus the oscillating spin density wave.

I.D Rare-Earth Tritellurides and Iron-Based Materials

It has long been known that layered compounds with a high degree of structural anisotropy offer a promising avenue in the search for materials with high superconducting critical temperatures T_c . The highest temperature superconductors known today, the copper-oxide based high- T_c materials, are strongly layered. Very recently, the pace of the search for layered compounds possessing high superconducting critical temperatures has greatly accelerated following the discovery of superconductivity (SC) at temperatures as high as 55 K in a class of layered materials containing FeAs planes. Interestingly, the parent compounds of the cuprate and FeAs-based high temperature superconductors display antiferromagnetic Mott insulating and spin density wave instabilities, respectively, and only become superconducting when the instability is suppressed towards zero temperature through pressure or doping. Indeed, over the past several decades it has become clear that SC very often appears when a second order phase transition is driven towards zero temperature near a so-called quantum critical point.

Chapters III and IV describe the results of high-pressure experiments carried out on two families of layered compounds, the rare-earth tritellurides, and the Fe-based superconductors. The rare-earth tritellurides are layered compounds in which two orthogonal charge-density waves form in the Te-Te sublattice, which are incommensurate with the underlying ionic structure. The competition between the pressure-suppressed CDW state with the pressure induced superconducting state is presented. For the Fe-based materials, the temperature-pressure phase diagrams of several superconducting and non-superconducting As- and P-based compounds are presented. In the As-based compounds, a spin-density wave appears at room temperature, which can be suppressed by either the application of pressure or chemical substitution, giving rise to the superconducting state. The P-based compounds, on the other hand, do not exhibit the SDW order, and superconductivity is observed below 10 K in some of the compounds.

Bibliography

- [1] J. Bardeen, L. N. Cooper, and J. R. Schrieffer, Phys. Rev. **108**, 1175 (1957).
- [2] G. Grüner, *Density Waves in Solids* (Addison-Wesley, Reading, MA, 1994).
- [3] C. A. Balseiro and L. M. Falicov, Phys. Rev. **20**, 4457 (1979).
- [4] G. Bilbro and W. L. McMillan, Phys. Rev. B **14**, 1887 (1976).
- [5] A. M. Gabovich, A. I. Voitenko, and M. Ausloos. Physics Reports **367**, 583-709 (2002).
- [6] P. Monceau and J. Richard, Physica B+C **108B**, 1237 (1981).
- [7] D. Jérôme, C. Berthier, P. Molinié, and J. Rouxel, J. Phys. (Paris) Colloq. **4** (37) C125 (1976).
- [8] B. Sipos, A. F. Kusmartseva, A. Akrap, H. Berger, L. Forró, and E. Tutiš, Nature Mater. **7**, 960 (2008).
- [9] A. F. Kusmartseva, B. Sipos, H. Berger, L. Forró, and E. Tutiš, Phys. Rev. Lett. **103**, 236401 (2009).
- [10] G. H. Lander, J. Magn. Magn. Mater. **29**, 271 (1982).
- [11] G. F. Hardy and J. K. Hulm, Phys. Rev. **89**, 884 (1953).
- [12] B. T. Matthias, T. H. Geballe, S. Geller, and E. Corenzwit, Phys. Rev. **95**, 1435 (1954).
- [13] S. A. Kivelson, I. P. Bindloss, E. Fradkin, V. Oganesyan, J. M. Tranquada, A. Kapitulnik, and C. Howald, Rev. Mod. Phys. **75**, 1201 (2003).
- [14] H. Schwenk, K. Andres, and F. Wudl: Phys. Rev. B **29** (1984).
- [15] M. B. Maple, J. W. Chen, Y. Dalichaouch, T. Kohara, C. Rossel, M. S. Torikachvili, M. W. McElfresh, and J. D. Thompson, Phys. Rev. Lett. **56**, 185 (1986).
- [16] M. B. Maple, R. E. Baumbach, J. J. Hamlin, D. A. Zocco, B. J. Taylor, N. P. Butch, J. R. Jeffries, S. T. Weir, B. C. Sales, D. Mandrus, M. A. McGuire, A. S. Sefat, R. Jin, Y. K. Vohra, J. -H. Chu, and I. R. Fisher, Physica B **404**, 2924 (2009).
- [17] N. W. Ashcroft and N. D. Mermin, *Solid State Physics* (1976).
- [18] N. W. Ashcroft and N. D. Mermin, *Solid State Physics*, Chapter 2, pp. 48-49 (1976).
- [19] A. A. Abrikosov and I. M. Khalatnikov, Rep. Prog. Phys. **22**, 329 (1959).

- [20] M. Kaveh and N. Wiser, Advances in Physics **33**, 257 (1984).
- [21] K. Kadowaki and S. B. Woods, Solid State Commun. **58**, 507 (1986).
- [22] P. W. Anderson, Phys. Rev. **124**, 41 (1961).
- [23] J. R. Schrieffer and P. A. Wolff, Phys. Rev. **149**, 491 (1966).
- [24] B. Coqblin and J. R. Schrieffer, Phys. Rev. **185**, 847 (1969).
- [25] M. A. Ruderman and C. Kittel, Phys. Rev. **96**, 99 (1954).
- [26] T. Kasuya, Prog. Theoret. Phys. **16**, 45 (1956).
- [27] K. Yosida, Phys. Rev. **106**, 893 (1959).
- [28] J. Friedel, Adv. Phys. **3**, 446 (1954).
- [29] W. J. de Haas, J. de Boer, and G. J. van den Berg, Physica **1**, 1115 (1934).
- [30] J. Kondo, Prog. Theoret. Phys. **32**, 37 (1964).
- [31] A. Sumiyama, Y. Oda, H. Nagano, Y. Onuki, K. Shibutani, and T. Komatsubara, J. Phys. Soc. Jpn. **55**, 1294 (1986).
- [32] S. Doniach, Physica B **91**, 231 (1977).
- [33] H. V. Löhneysen, A. Rosch, M. Vojta, and P. Wolfle, Rev. Mod. Phys. **79**, 1015 (2007).
- [34] M. B. Maple, R. E. Baumbach, N. P. Butch, J. J. Hamlin, and M. Janoschek, J. Low Temp. Phys. **161**, 4 (2010).
- [35] H. K. Onnes, Leiden Comm. **120b**, **122b**, **124c** (1911).
- [36] B. T. Matthias, T. H. Geballe, R. H. Willens, E. Corenzwit, and G. W. Hull Jr., Phys. Rev. **139**, A1501 (1965).
- [37] J. G. Bednorz and K. A. Müller, Z. Phys. B 64, **189** (1986)
- [38] M. Núñez-Regueiro, J. -L. Tholence, E. V. Antipov, J. -J. Capponi, M. Marezio, Science **262**, 97 (1993).
- [39] Z. -A. Ren, W. Lu, J. Yang, W. Yi, X. -L. Shen, Z. -C. Li, G. -C. Che, X. -L. Dong, L. -L. Sun, F. Zhou, and Z. -X. Zhao, Chin. Phys. Lett. **25**, 2215 (2008).
- [40] W. Meissner and R. Ochsenfeld, Naturwiss. **21**, 787 (1933).
- [41] Z. -A. Ren, W. Lu, J. Yang, W. Yi, X. -L. Shen, Z. -C. Li, G. -C. Che, X. -L. Dong, L. -L. Sun, F. Zhou, and Z. -X. Zhao, Chin. Phys. Lett. **25**, 2215 (2008).

- [42] F. London and H. London, Proc. Roy. Soc. (London) **A149**, 71 (1935).
- [43] V. L. Ginzburg and L. D. Landau, Zh. Eksperim. i Teor. Fiz. **20**, 1064 (1950).
- [44] A. A. Abrikosov, Sov. Phys. JETP **5**, 1174 (1957).
- [45] M. B. Maple, in Magnetism: A Treatise on Modern Theory and Materials, ed. H. Suhl (Academic Press, New York, 1973) Vol. V, Chapter 10; and references cited therein.
- [46] B. T. Matthias, H. Suhl, E. Corenzwit, Phys. Rev. Lett. **1**, 92 (1958).
- [47] A. A. Abrikosov and L. P. Gor'kov, Soviet Phys. JETP **12**, 1243 (1961).
- [48] D. C. Johnston, Advances in Physics **59**, Issue 6, 803 (2010).
- [49] N. D. Mathur, F. M. Grosche, S. R. Julian, I. R. Walker, D. M. Freye, R. K. W. Haselwimmer, and G. G. Lonzarich, Nature **394**, 39 (1998).
- [50] C. L. Seaman, M. B. Maple, B. W. Lee, S. Ghamaty, M. S. Torikachvili, J. S. Kang, L. Z. Liu, J. W. Allen, and D. L. Cox, Phys. Rev. Lett. **67**, 2882 (1991).
- [51] G. R. Stewart, Rev. Mod. Phys. **73**, 797 (2001).
- [52] The periodicity of the charge or spin density can be extracted from the Fourier transform definition of $\rho^{ind}(\vec{r})$. For a delta-Dirac-like response function, then, at $q = 2k_F$, the Fourier transform results in $\rho^{ind}(\vec{r}) \sim \exp(i2k_F r)$.
- [53] D. Baeriswyl and J. J. Forney, J. Phys. C: Solid St. Phys. **13**, 3203 (1980).
- [54] M. Lavagnini, M. Baldini, A. Sacchetti, D. Di Castro, B. Delley, R. Monnier, J. -H. Chu, N. Ru, I. R. Fisher, P. Postorino, and L. Degiorgi, Phys. Rev. B **78**, 201101(R) (2008).
- [55] R. E. Peierls, *Quantum Theory of Solids*, Oxford University Press, New York (1955).

II

Experimental Methods

II.A Sample Synthesis

The samples utilized in this work were prepared at different institutions. Single crystals of rare-earth tritellurides ($R\text{Te}_3$) were provided by Prof. Ian R. Fisher's group in Stanford University, and they were grown using a standard Te-flux technique [1] described in Section III.C and references therein. Polycrystalline samples of $\text{LaFeAsO}_{0.89}\text{F}_{0.11}$, $\text{CeFeAsO}_{0.88}\text{F}_{0.12}$ and CeFeAsO were prepared at Oak Ridge National Laboratory described in Section IV.B. Single crystals of LaFePO and CeFePO were grown at UCSD, using the molten Sn:P flux technique described also in Section IV.B. Single crystals of CuFeTe_2 were grown at UCSD using a standard melt technique, as described in Section IV.E.

The samples were cut with a razor blade to fit the sample space of the different high-pressure techniques utilized in the experiments. For electrical resistivity measurements, good electrical contacts were achieved after obtaining a clean, flat surface in the samples. For the $R\text{Te}_3$ and CuFeTe_2 single crystals, a good surface was obtained after cleaving the samples with an adhesive tape. For the iron-pnictide samples, the surfaces were polished using 600 grit sand paper and 9 micron polishing paper.

II.B High Pressure Techniques

High pressure provides scientists a powerful method of changing in a controlled and reversible manner the volume of a sample, affecting the electronic and structural properties of the materials. For example, 24 of the 53 superconducting elements of the periodic table become superconductors only at high pressures [2]. High-pressure techniques are currently applied in many branches of physics, chemistry and biology, achieving maximum pressures of up to 400 GPa (4 megabars), which is larger than the pressure at the Earth's core (3.5 Mbar), in a wide range of temperatures due to the possibility of fabricating high-pressure devices of small dimensions that can be cooled in commercially available cryostats. The modern era of high-pressure physics started at the beginning of the 20th century with the work led by P. W. Bridgman at Harvard University, where he developed the technique that carries his name, and set the grounds for the implementation of the diamond-anvil cell technique. Bridgman received the Nobel prize in Physics in 1946, “*for the invention of an apparatus to produce extremely high pressures, and for the discoveries he made therewith in the field of high pressure physics*”.

In the following Chapters, a series of high-pressure experiments are presented, where three different techniques were utilized, which will be described below. For a very complete compendium of high pressure techniques, see for instance the book “High Pressure Experimental Methods” by M. Emerets (Ref. [3]).

II.B.1 Hydrostatic Piston-Cylinder Clamped Cell

A diagram of a typical hydrostatic piston-cylinder clamped cell is shown in Fig. II.1. The load is applied with a hydraulic press to a tungsten-carbide (WC) piston (c) which transmits the load to the sample space (f) (0.25” O.D.). The sample space is embodied in a pressure-medium-containing capsule made of a soft-material (usually Teflon), which seals against an anti-extrusion sample holder (AESH) made of a non-magnetic beryllium-copper alloy Berylco-25 (g). The cylin-

der (k) is made of a high-yield strength material (Berylco-25 or the Ni-Co-Cr-Mo alloy MP35N) of 1" of outer diameter, and an axial cylindrical hole of 0.25" of internal diameter that allows a perfect fit with the teflon capsule-AESH array. A backing WC piston (h) and plate (i) are used to keep the AESH inside the cylinder. The applied load is then maintained in the piston-cylinder by the outer main body of the cell (l) and the two clamping nuts (a,j), all made of non-magnetic Berylco-25. The pressure limit for a piston-cylinder apparatus is about 5 GPa. The practical pressure limit (when a steel cell is operating for a long time with some safety coefficient) is about 3 GPa for a cell that would fit in a small sample space such as the inner diameter of a superconducting magnet.

The interior of the sample space is filled with a pressure-transmitting medium, which is selected depending on the maximum hydrostatic pressure that one desires to attain. For a piston-cylinder clamped cell, a liquid medium is commonly utilized, with appropriate seals around the Teflon capsule designed to withstand the high pressures applied. In recent work [4], we found that the physical properties of an URu_2Si_2 single crystal were not reversible upon application and release of the pressure when the commonly used mixture of 1:1 Fluorinert FC70/FC77 and pure FC75 were used. In contrast, no hysteresis was observed when the pressure medium was a 1:1 mixture of n-pentane/isoamyl alcohol, which remains hydrostatic up to 3 GPa. For this reason, the experiments reported herein were done using the latter pressure medium.

The measurement of the electrical resistivity of samples in the hydrostatic cell requires the wires to reach the interior of the sample space through a small hole in the AESH. In order to prevent the loss of pressure medium during pressurization and consequent temperature cycles, this hole was sealed using Styccast 2850FT epoxy (catalyst 11), cured at 100°C for 3 hours. The right-hand photograph of Fig. II.1 displays an AESH containing 8 copper wires for measuring standard 4-lead electrical resistivity of two samples. At the bottom part of the sample space, on top of the black Styccast epoxy, a ring-shaped manometer was placed for that

particular experiment. The manometer is made of pure Pb or Sn, which have well-known calibrations of their superconducting critical temperature as a function of pressure [5, 6]. The superconductivity of the manometer is measured at low temperature with a set of ac-susceptibility coils embedded in the main body of the cell. Approximately 10000 pounds of force applied with the hydraulic press at room temperature resulted in a pressure of approximately 1 GPa at low temperature.

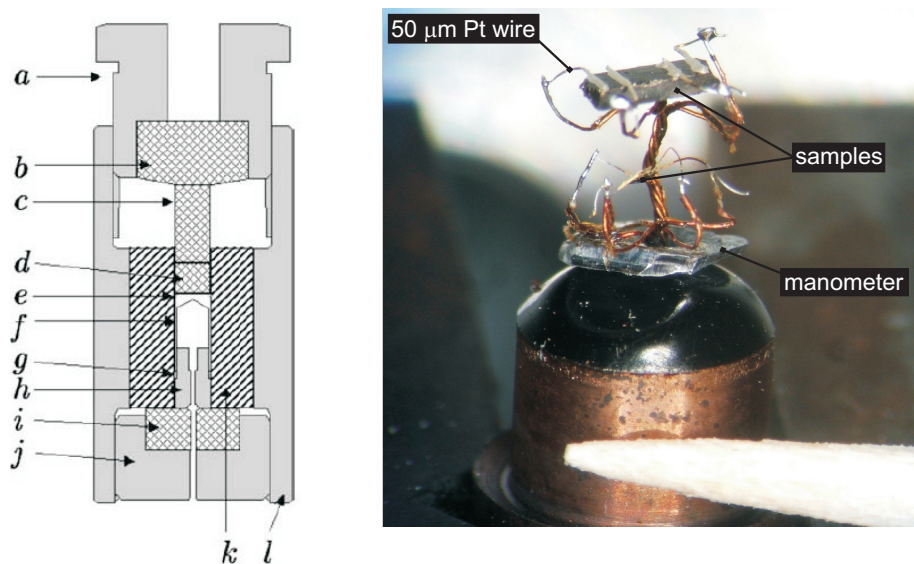


Figure II.1: *Left:* Piston-cylinder hydrostatic clamped cell diagram (from Ref. [7]). (a) Be-Cu clamping nut. (b) Be-Cu/WC load transmitter. (c, d) WC piston. (e) Be-Cu anti-extrusion disk. (f) Teflon capsule (sample space). (g) Be-Cu anti-extrusion sample holder. (h) WC backing piston. (i, j) WC backing plate and nut. (k) Inner cylinder (alloy). (l) Be-Cu body. *Right:* Photograph of the anti-extrusion sample holder, with two samples connected for electrical resistivity measurements. The tip of a toothpick is shown for size comparison.

II.B.2 Bridgman-Anvil Cell

When a material is compressed between anvils, the pressure achieved is much higher than that in piston-cylinder cells, for the following reasons: a) the material of the anvils is working mainly under compression, and very hard materials such as diamond, sapphire and tungsten-carbide (WC) can be used, which have compressive yield strengths three or more times the tensile yield strength σ_y ; 2) pressures much higher than σ_y are generated when anvils are made in the form of a truncated cone, because the loaded area is supported by the surrounding material; c) multiplication of pressure occurs, which means that the pressure between the anvils is not uniform and maximal pressure in the center of the anvils may be much higher than the applied load divided by the contact area.

In a Bridgman-anvil cell device, pressures up to 16 GPa were achieved. The application of load method is similar to the one described for the hydrostatic piston-cylinder technique, *i.e.*, the load is applied with a hydraulic press and maintained by the main body and clamping nuts of the cell. The difference resides in the absence of a piston and a cylinder. Instead, two opposite Berylco-25 anvils with an insert of hard WC compress the sample and the surrounding medium, both contained within a gasket. The gasket also supports the edges of the anvils, and critically determines the pressure distribution on the anvil. Figure II.2 displays a photograph of a Bridgman anvil utilized in this work. The outer beryllium-copper ring contains the inner tungsten-carbide anvil (grey color), which has a conical shape and ends with a flat surface of 3.5 mm in diameter. The flat region is shown in more detail in the magnified view. The gasket is composed of a 3.5 mm outside diameter pyrophyllite $[Al_2Si_4O_10(OH)_2]$ ring with a 2 mm inner diameter, and a thickness of 0.25 mm. The pyrophyllite ring provides radial support to the sample chamber, preventing the contents of the chamber from extruding outward, and the inner diameter comprises the sample chamber, where the sample and manometer are located. Two disks made of pressed steatite powder [*soapstone*, $Mg_3Si_4O_10(OH)_2$], one at the bottom and another at the top of the sample chamber

(only the bottom one is displayed in Fig. II.2), serve as quasi-hydrostatic pressure transmitting medium.

Electrical contacts on the samples are obtained by compressing 25 or 50 μm annealed Pt wires onto the samples, which reach the sample chamber through grooves cut in the pyrophyllite ring by hand with a razor blade. In the photograph of Fig. II.2, a sample (black) and a strip of Pb (grey) are located in the sample chamber, with eight Pt leads for the measurement of the resistance of the sample, and the superconducting transition of the Pb manometer. After a steatite disk is placed at the top, the upper anvil is brought against the lower one, and load is applied, creating the electrical contacts. Pressures generated with this technique can yield to strong pressure gradients along the sample. These gradients create a distribution of superconducting T_c 's in the manometer, so the width of the superconducting transition of the manometer is a good measure of the pressure gradients inside the sample space.

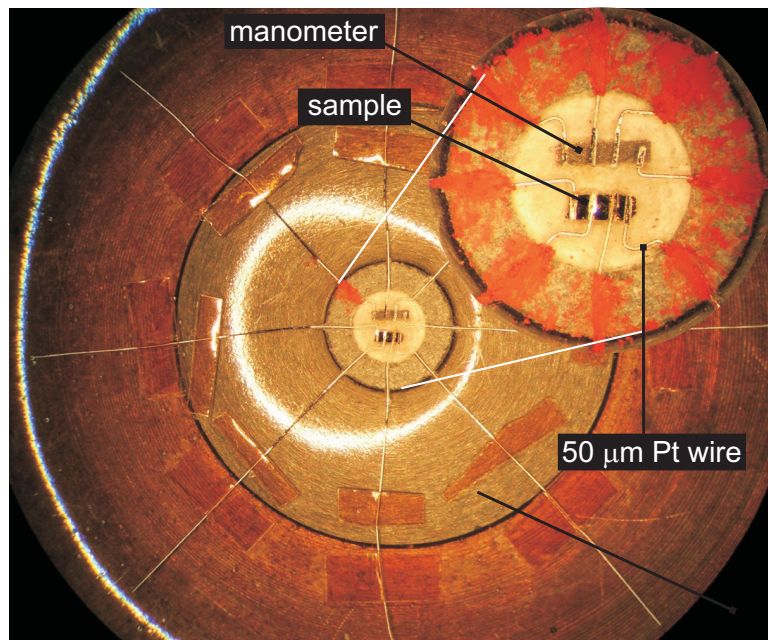


Figure II.2: Photograph of an anvil utilized in the Bridgman-anvil high-pressure technique.

II.B.3 Diamond-Anvil Cell

Maximal static pressures have now been achieved with the diamond anvil cell (DAC) technique. From the mechanical point of view, a DAC is a Bridgman-anvil cell, but using the strongest material (diamond) to build the anvils. The highest pressures can be achieved with anvils of nearly conical form. The working faces of multimegarabar anvils are of truncated conical form with a small diameter at the tip of the diamond. The DAC employed in the experiments reported in Chapter IV is a mechanically loaded commercial model, manufactured by Kyowa Seisakusho Ltd.. Fig. II.3 shows a diagram of a DAC. The upper anvil consists of a blank diamond (usually non-bevelled, with a tip of $\sim 300 \mu\text{m}$ in diameter), while the diamond used at the bottom is called “designer” diamond, since it contains four, six or eight deposited tungsten microprobes encapsulated in high-quality homoepitaxial diamond, for electrical resistivity measurements. The designer diamonds were obtained from a collaboration with Dr. S. T. Weir from Lawrence Livermore National Laboratory and Prof. Y. K. Vohra from University of Alabama at Birmingham [8], and they have culet sizes of $\sim 500 \mu\text{m}$ and bevelled to a tip of $\sim 250 \mu\text{m}$. The gasket was made from a $200 \mu\text{m}$ thick MP35N foil pre-indented to $40\text{-}50 \mu\text{m}$ and a $85\text{-}120 \mu\text{m}$ diameter hole was drilled through the center of the indentation using an electrical discharge machine (EDM). The pre-indented thickness should be approximately $1/9$ of the culet diameter and $1/3$ of the hole diameter. Depending on the sample and pressure medium, the initial diameter of the hole should be adjusted so that it reaches $1/3$ of the culet diameter at high pressure. The sample space corresponds to the volume enclosed by the hole in the gasket and the flat tips of the two diamonds. In the DAC experiments, pressure is inferred from the fluorescence spectrum of several $\sim 5 \mu\text{m}$ diameter ruby spheres loaded into the hole in the gasket, and using the calibration by Chijoike *et al.* [9] and the formula

$$P(\text{GPa}) = \frac{1876}{10.71} \left[\left(\frac{\lambda}{\lambda_0} \right)^{10.71} - 1 \right] \quad (\text{II.1})$$

where λ and λ_0 are the measured wavelength of the R_1 line of ruby at high pressure and at ambient pressure, respectively. The remaining space in the hole was filled with sample, that is, no pressure transmitting medium was utilized, although in some cases solid steatite was used.

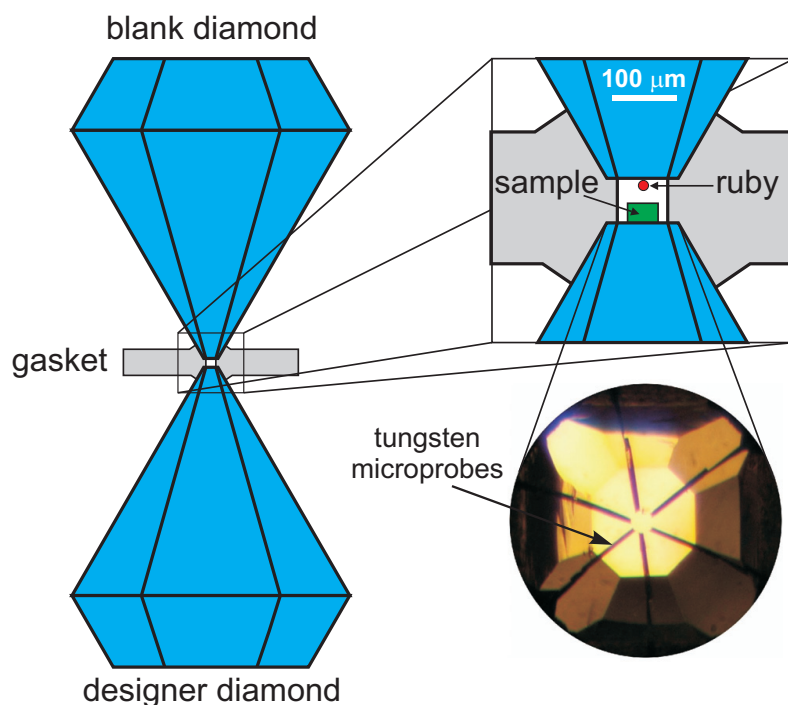


Figure II.3: Diamond-anvil cell technique. The upper diamond is a blank diamond, while the bottom one is a “designer” diamond, with deposited tungsten microprobes encapsulated in high-quality homoepitaxial diamond, for electrical resistivity measurements, as can be seen in more detail in the photograph. The sample is located in the space enclosed by the two diamonds and the hole of the gasket.

II.C Measurement Methods

II.C.1 Electrical Resistivity

The electrical resistivity was measured using the standard 4-lead technique. Contacts of $\sim 2 \Omega$ were obtained after evaporating gold pads onto the surface of the samples. Platinum or gold leads ($50 \mu\text{m}$) were attached to the gold pads with five minute silver epoxy (Epotek H20E) cured at 200°C for $3 - 5$ minutes. In the case of Bridgman-anvil high-pressure studies, electrical contact was made by pressing platinum wires directly onto the samples.

Electrical resistivity measurements at ambient pressure were obtained using a Quantum Design Physical Property Measurement System (PPMS) throughout the temperature range $1.8 \text{ K} \leq T \leq 20 \text{ K}$ and for magnetic fields ranging from 0 to 9 T.

For the high pressure experiments, the electrical resistance was measured using a Linear Research Inc. LR-700 AC resistance bridge operating at 16 Hz. The experiments at high pressure were done in two different cryostats: from room temperature to 1.2 K, a conventional ^4He bucket connected to a pumping system was used, and for temperatures ranging from $0.05 \text{ K} \leq T \leq 2 \text{ K}$, an Oxford Kelvinox MX100 ^3He - ^4He dilution refrigerator was utilized, equipped with a 9 T wide bore superconducting magnet that fits the high pressure cells.

II.C.2 Magnetic Measurements

DC-Magnetic Susceptibility at Ambient Pressure

Magnetization measurements were performed using a commercial Quantum Design Magnetic Properties Measurement System (MPMS) Superconducting Quantum Interference Device (SQUID) magnetometer. The sample chamber of the MPMS was cooled by a ^4He flow cryostat capable controlling temperature from 1.8 - 400 K. The MPMS is also equipped with a 9 T superconducting magnet.

AC-Magnetic Susceptibility at High Pressure

In some cases, ac-susceptibility measurements were performed in the hydrostatic piston-cylinder clamps. As it was mentioned before, these clamps have built-in primary and secondary coils in the main body of the cells for detecting the superconducting transition of the Pb or Sn manometer located inside the teflon capsule. This coil system is sensitive enough for measuring the full shielding of these relatively large manometers. However, for experiments in which small single crystals are utilized, a secondary coil surrounding the sample is preferable for higher sensitivity. For this reason, a set of secondary coils was designed to fit inside the 1/4"- and 3/8"-diameter teflon capsules (Fig. II.4). The spools of the coils were fabricated using Vespel, a hard plastic which is relatively easy to machine in small dimensions. The voltage induced in the secondary coils is given by the formula

$$S(V) = \frac{\pi f H V N \alpha}{R(1 - D)} \chi, \quad \alpha \equiv \left[1 + \left(\frac{2L}{R} \right)^2 \right]^{-1/2} \quad (\text{II.2})$$

where f is the frequency of the excitation voltage at the primary coils in Hz, H is the magnetic field created by the primary coils at the position of the secondary coils (in tesla), V is the volume of the sample located in one of the two coils of the secondary, and N , R and L are the number of turns, average radius and height of one of the secondary coils, respectively. D corresponds to the demagnetization factor of the sample ($D = 0.75$ for a disk), while $\chi = -1$ for a type-I superconductor. In order to maximize the number of turns N , a thin Cu wire of gauge AWG50 was utilized, which has a bare nominal diameter of 25 μm and it is insulated with a $\sim 1.5 \mu\text{m}$ layer of Formvar varnish (MWS Wire Industries). With this wire it was possible to wind ~ 500 turns on each coil of the secondary, 19 layers each, with a total electrical resistance of $\sim 210 \Omega$. For an excitation frequency of 1023 Hz and an applied field of ~ 5 Oe, an induced voltage of $\sim 100 \mu\text{V}$ was estimated to arise from the shielding of a 100 μm -thick type-I superconducting sample that would fit in the 1 mm-diameter space of the spools. After compensating the coils to give approximately zero voltage without samples, the x100 pre-amplified signal

measured by the lock-in amplifier gave a very good signal-to-noise ratio for the detection of a superconducting transition of a Sn and Pb samples located in the center of each of the secondary coils (Fig. II.5).

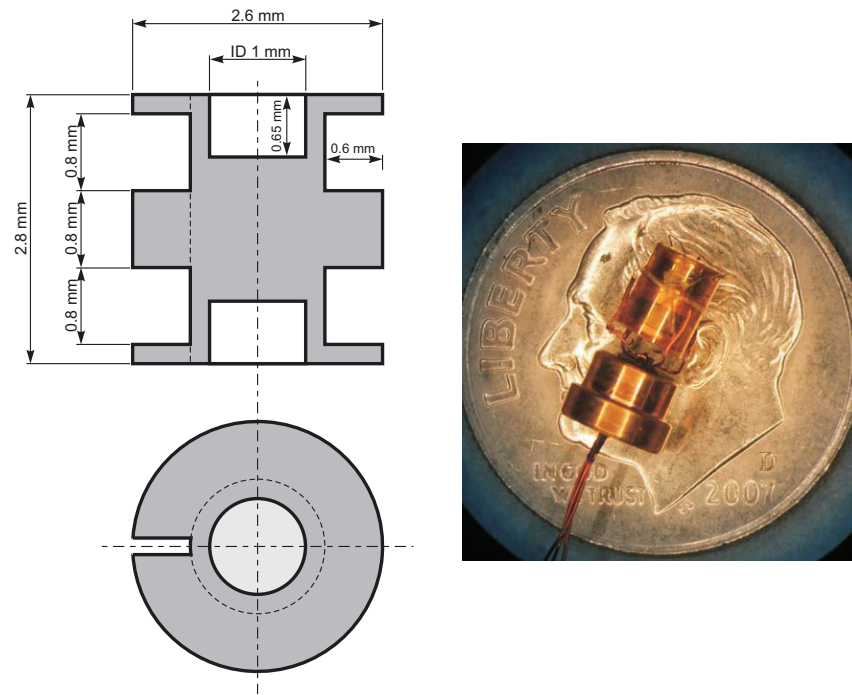


Figure II.4: Coils system designed for ac-susceptibility measurements in the piston-cylinder clamped cells. The photograph on the right shows the coils mounted on a anti-extrusion sample holder of 0.25" in diameter.

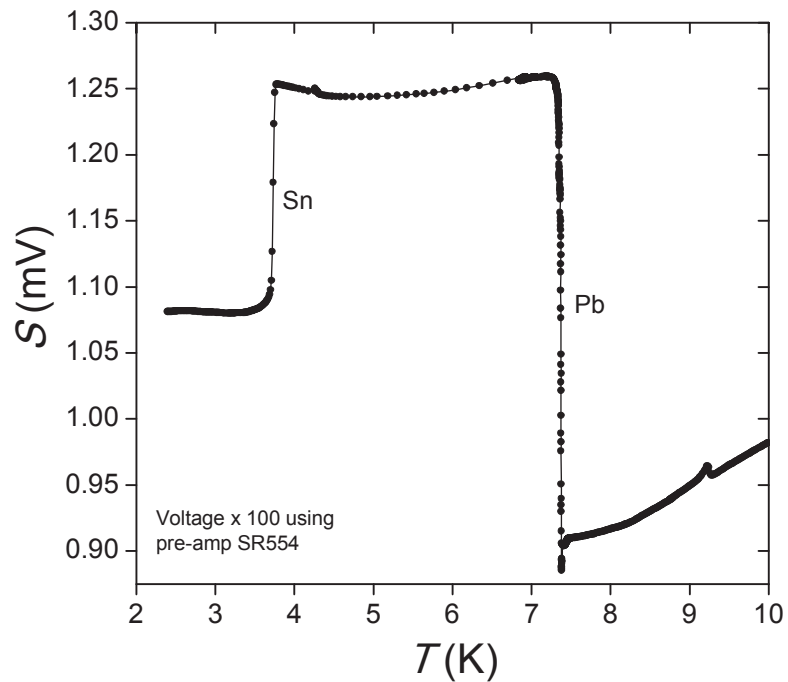


Figure II.5: Test of the coil system designed for ac-susceptibility measurements in the hydrostatic cell. For this test, one sample of Pb and another of Sn were placed on each side of the secondary coils. The voltage induced in the coils was pre-amplified before being detected with the lock-in amplifier at 1023 Hz.

II.C.3 Calorimetry Measurements

Heat-Pulse-Relaxation at Ambient Pressure

The specific heat C was measured as a function of temperature T from 0.35 to 300 K using a ^3He semiadiabatic calorimeter and a standard heat pulse technique for magnetic fields up to 5 T. Samples were mounted in Apiezon N-Grease on top of a sapphire substrate suspended by fine strings. The heater and the thermometer were attached to the substrate.

AC-Calorimetry at High Pressure

In many cases, a direct experimental measurement of the pressure dependence of the specific heat is highly desired. Calorimetry measurements at high pressures are extremely difficult to achieve due to the fact that the sample is thermally connected through the pressure medium to the massive addenda given by the pressure cell. Thus, the heat capacity of the total pressure device will always be measured if the standard adiabatic calorimetry technique is employed. The ac method was first described by Sullivan and Seidel in 1968 [10] and applied later in 1979 to high pressure experiments by Eichler and Gey [11], and in principle permits the determination of the heat capacity of the sample alone, even when it is not completely thermally decoupled from the temperature bath. For the pressure experiments, a heater and a thermometer (usually a thermocouple) are attached directly onto the surface of the sample. If an ac power of the form $P(t) = P_0(1 - \sin\omega t)$ is applied to the heater, the temperature of the sample T will change accordingly to $T - T_0 = \Delta T_{dc} + \Delta T_{ac}(t)$, where T_0 is the temperature of the bath, and $\Delta T_{ac}(t) \equiv \tilde{T}\sin(\omega t + \phi)$. Sullivan and Seidel gave a simple formula for the amplitude \tilde{T} from which the heat capacity of the sample can be derived:

$$\tilde{T} = \frac{P_0}{\omega C} \left[1 + \frac{1}{(\omega\tau_1)^2} + \frac{1}{(\omega\tau_2)^2} \right]^{-1/2} \equiv \frac{P_0}{\omega C} F(\omega), \quad (\text{II.3})$$

where τ_1 and τ_2 are the characteristic time constants describing the thermal coupling of the sample with the bath and with the heater-thermometer, respectively.

These characteristic constants must be determined in each experiment, and the aim is to find a frequency ω such that

$$(\omega\tau_1)^2 \gg 1, \quad (\omega\tau_2)^2 \ll 1, \quad (\text{II.4})$$

that is, a frequency for which the sample is poorly thermally connected to the bath and very well connected to the heater-thermometer array. For this frequency, $F(\omega) = 1$ is a good approximation, and the heat capacity of the sample would be inversely proportional to the amplitude of the temperature oscillations \tilde{T} . A plot of $\omega\tilde{T}$ versus ω would give the form of the response function $F(\omega)$, which should be frequency independent in the range $1/\tau_1 \ll \omega \ll 1/\tau_2$ [12].

In the tests described in Section III.G.2, the thermometer was made of spot-welded Au and $\text{Au}_{0.93}\text{Fe}_{0.07}$ 50 μm wires and the ac-power was applied to the sample through two other Au wires, all attached to the sample using silver epoxy (Fig. II.6). The sample was then connected to an anti-extrusion sample holder as described in Section II.B.1.

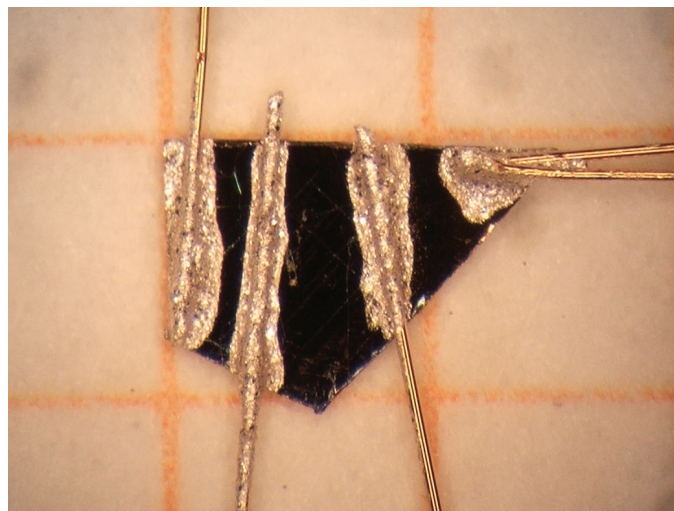


Figure II.6: Photograph of a TbTe_3 single crystal with three 50 μm Au wires and a thermocouple made of spot-welded Au and $\text{Au}_{0.93}\text{Fe}_{0.07}$ 50 μm wires for electrical resistivity and ac-calorimetry measurements. Underneath the sample, a 1 \times 1 mm² ruled paper was placed as a reference.

Bibliography

- [1] Z. Fisk and J. P. Remeika, "Handbook on the Physics and Chemistry of Rare Earths," Vol 12, edited by K. A. Gschneidner, Jr. and L. Eyring (Elsevier Science Publishing Company, Inc., New York, New York, 1989) pp. 53-70.
- [2] J. S. Schilling, "Periodic Table of Superconductivity," (<http://physics.wustl.edu/~jss/NewPeriodicTable.pdf>).
- [3] M. Eremets, "High Pressure Experimental Methods," Oxford University Press, Oxford (1996).
- [4] N. P. Butch, J. R. Jeffries, D. A. Zocco, and M. B. Maple, High Pressure Res. **29**, 335 (2009).
- [5] B. Bireckoven and J. Wittig, J. Phys. E **21**, 841 (1988).
- [6] T. F. Smith, C. W. Chu, and M. B. Maple, Cryogenics **9**, 53 (1969).
- [7] H. Taniguchi, S. Takeda, R. Satoh, A. Taniguchi, H. Komatsu, and K. Satoh, Rev. Sci. Instrum. **81**, 033903 (2010).
- [8] S. T. Weir, J. Akella, C. Aracne-Ruddle, Y. K. Vohra, and S. A. Catledge, Appl. Phys. Lett. **77**, 3400 (2000).
- [9] A. D. Chijioke, W. J. Nellis, A. Soldatov, I. F. Silvera, J. Appl. Phys. **98** (11), 114905 (2005).
- [10] P. F. Sullivan and G. Seidel, Phys. Rev. **173**, 679 (1968).
- [11] A. Eichler and W. Gey, Rev. Sci. Instrum. **50**, 11 (1979).
- [12] Y. Kohama, C. Marcenat, T. Klein, and M. Jaime, Rev. Sci. Instrum., **81** 104902 (2010).

III

Superconductivity, Magnetism and Charge-Density Waves in Rare-Earth Tritellurides ($R\text{Te}_3$)

III.A Introduction

Charge- and spin-density waves (CDWs and SDWs) frequently occur in low-dimensional materials, and are driven by electron-phonon and electron-electron interactions. These phases are formed by nesting of the Fermi surface, which can be perfect in one-dimensional systems [1]. A perfect nesting CDW system refers to the situation where all the electrons near the Fermi surface are excited with the same q vector of a particular phonon mode. On the other hand, incomplete nesting takes place for higher dimensional materials, for which a density wave gap opens only over certain regions of the Fermi surface. Rare-earth tritellurides $R\text{Te}_3$ ($R = \text{La-Tm}$, except for Eu) constitute a class of quasi-two-dimensional materials that has recently attracted a considerable amount of attention as the first system in which nominal square-planar symmetry is broken by the formation of a unidirectional charge density wave (CDW) [2], and because the electronic properties of these materials can be changed by substituting one rare-earth element for an-

other, making them ideal candidates for investigating the properties of the CDW state [3, 4, 5]. The rare-earth tritellurides crystallize in the NdTe_3 structure that belongs to the space group *Cmcm* (No. 63); the structure consists of alternating double layers of nearly square-planar Te sheets and corrugated double $R\text{Te}$ layers and forms a weakly orthorhombic lattice above the CDW transition temperature [6]. In this standard space group denomination, the *b*-axis is oriented perpendicular to the *ac*-planes (Fig. III.1), and the average lattice parameters for all the lanthanide series are $(a, b, c) \sim (4, 26, 4)$ Å. It is evident that these compounds are electronically anisotropic, with the Te planes quite decoupled from the $R\text{Te}$ slabs [7, 8]. Because large areas of Fermi surface are parallel and may be connected by a single nesting vector, these compounds are unstable to the formation of an incommensurate CDW within the *ac*-planes. For this family of materials, the lattice modulation is characterized by a single in-plane wave vector q_1 , which has approximately the same value for all the rare earths ($q_1 \approx 2c^*/7$, with $c^* = 2\pi/c$) [3].

It has been shown that the application of chemical pressure reduces the CDW ordering temperature from values above 450 K for the lighter La, Ce, Nd and Pr rare-earth tritellurides, to 244 K for the heaviest TmTe_3 compound [9, 10, 11], as it is shown in Fig. III.2 (filled square symbols). Moreover, a reduction with chemical pressure of the single particle excitation frequency characteristic of the CDW state is accompanied by a decrease in the fraction of the Fermi surface that remains gapped, driving the samples towards a state of enhanced metallicity. This behavior was also observed in CeTe_3 with the application of external pressure [12, 13], extending the study of the above mentioned phenomenon to even smaller lattice parameters than attainable through chemical pressure.

A second CDW ordering temperature has recently been discovered for the heavier compounds with smaller lattice parameters (Tm, Er, Ho, Dy) [10]. In this case, the CDW is characterized by a wave vector q_2 transverse to the first one, and of larger value ($q_2 \approx a^*/3$). This phase occurs at lower temperatures,

dropping below 50 K for DyTe_3 , and it increases with the application of chemical pressure. The shift of our attention to CDW formation at low temperatures allows us to consider the effects caused on this state by other competing types of order. Also, CeTe_3 is interesting itself, since cerium-based compounds frequently display an enhancement of their electronic effective mass at low temperatures caused by the strong hybridization of the localized $4f$ and conduction electron states and produce a variety of ground states, such as localized moment magnetic order [14] and superconductivity [15], with many of these phases induced at high pressures [16]. In fact, the $R\text{Te}_3$ compounds also display magnetic order at or below ~ 10 K [11, 17], as it is also shown in Fig. III.2 (filled circular symbols). The competing interaction of the CDW with some of these strongly correlated electron states by tuning chemical composition, pressure or magnetic field is of particular interest in these materials [18]. The following sections describe the study of the influence of external pressure on the various ordering temperatures of CeTe_3 , GdTe_3 , TbTe_3 and DyTe_3 compounds and the investigation of the possibility that superconductivity might appear if any of these ordering temperatures could be driven towards zero temperature.

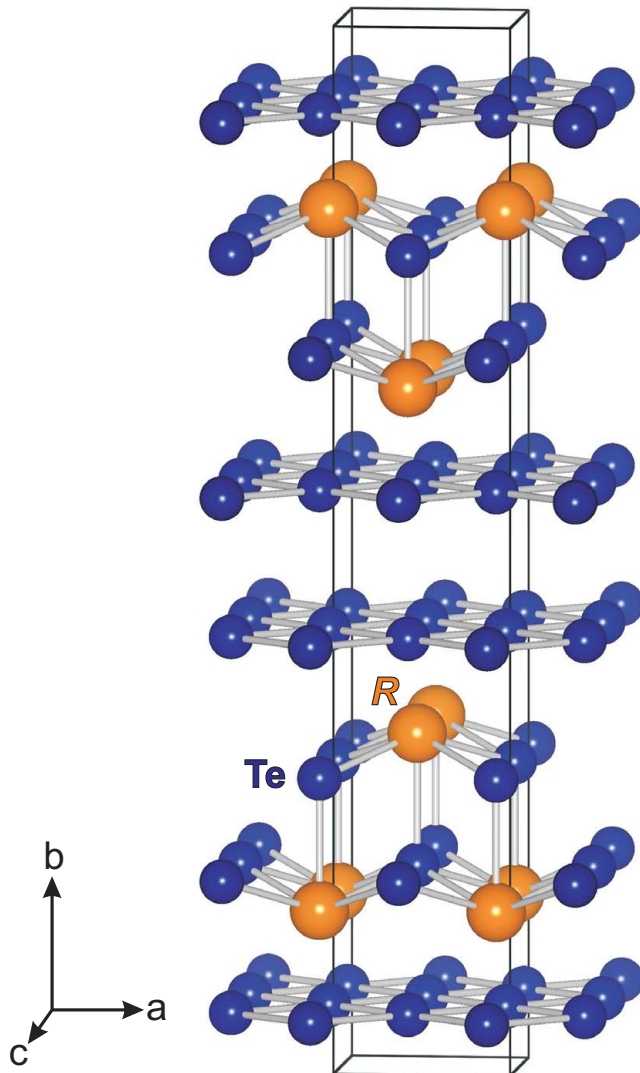


Figure III.1: Crystal structure of RTe_3 , consisting of alternating double layers of nearly square planar Te sheets and corrugated double RTe layers. This series of compounds crystallizes in the $NdTe_3$ structure that belongs to the space group $Cmcm$ (No. 63), with the b -axis oriented perpendicular to the ac -planes. The unit cell is enclosed in the box. Crystal structure created with *Vesta* [19].

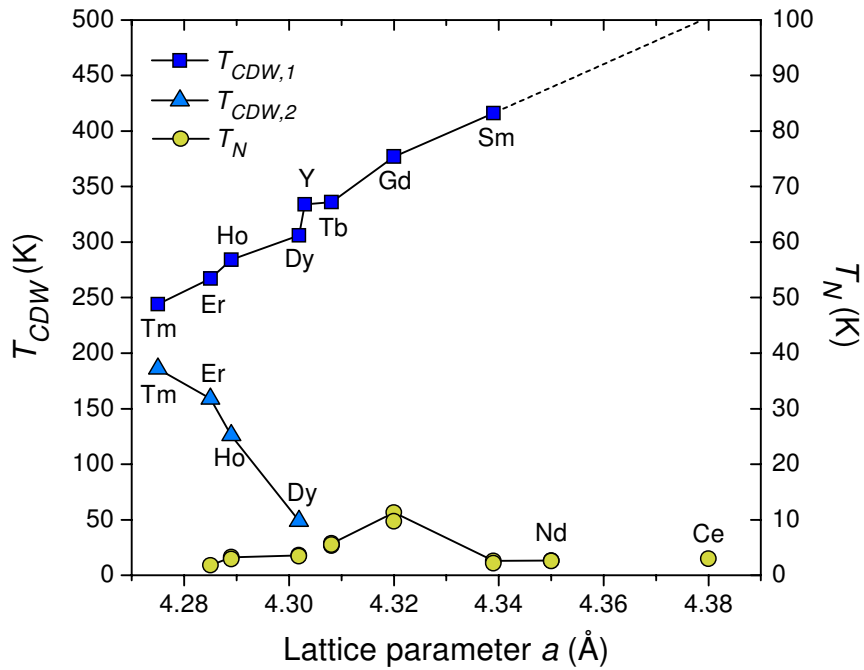


Figure III.2: Charge-density wave ordering temperatures $T_{CDW,1}$ and $T_{CDW,2}$ (*left axis*) and Néel temperature T_N (*right axis*) plotted as a function of in-plane lattice parameter a for the different RTe_3 compounds. The dashed line serves as a guide to the eye, suggesting that the lighter Nd, Pr, Ce and La compounds would possibly order into the CDW state at $T_{CDW,1}$ larger than 400 K. Lattice parameters were extracted from Ref. [8]. Values of $T_{CDW,1}$ and $T_{CDW,2}$ were obtained from Ref. [10], and T_N values from Refs. [11, 17].

III.B Electronic Structure of $R\text{Te}_3$

For the rare-earth tritellurides, the rare-earth atoms ionize to the 3+ valence state, leaving the $4f$ shell as the only unfilled atomic shell. The $4f$ orbitals lie much closer to the nuclei than the completely filled $5s^2$ and $5p^6$ orbitals, from which the magnetic moment arising from the unfilled $4f$ shell can be considered as localized, and with the ground state configuration determined by Hund's rules [20].

The electronic structure of the $R\text{Te}_3$ system was previously studied by several authors [3, 4, 5, 21]. The tight-binding model considers the p bands of a single square-planar Te sheet, but including also the electrons donated by the $R\text{-Te}$ corrugated layers. The Te atoms ionize in the 2– state and the rare-earths in the 3+ state, so the $R\text{-Te}$ sheets donate one electron to the two tellurium atoms ($1/2$ electron/Te). Since neutral Te atoms have the [Kr] $4d^{10}5s^25p^4$ electronic configuration, the donated $1/2$ electron leaves the ionic Te with 4.5 p electrons, which are distributed among the p_x , p_y and p_z orbitals. In our representation, p_y are the out-of-plane orbitals which are completely filled, since they are energetically more favorable than p_x and p_z , leaving the remaining 2.5 electrons to be distributed between the remaining p_x and p_z orbitals ($2.5/4 = 5/8$ filling).

The tight-binding model considers three types of hopping energy scales in the $a - c$ plane: t_{\parallel} is the coupling parameter along the orbital chains, t_{\perp} is the coupling parameter perpendicular to the chains, and t' is a $p_x - p_z$ mixing parameter, much smaller than the other two, so it is neglected (Fig. III.3a). The energy bands obtained with the tight-binding model in the 3D Brillouin zone (BZ) are described by:

$$E_{p_x}(k_x, k_z) = -2t_{\parallel}\cos\left[(k_x + k_z)\frac{a}{2}\right] - 2t_{\perp}\cos\left[(k_x - k_z)\frac{a}{2}\right] - E_F \quad (\text{III.1})$$

$$E_{p_z}(k_x, k_z) = -2t_{\parallel}\cos\left[(k_x - k_z)\frac{a}{2}\right] - 2t_{\perp}\cos\left[(k_x + k_z)\frac{a}{2}\right] - E_F \quad (\text{III.2})$$

where k_x and k_z are the wave-vectors along the x and z directions, respectively, and E_F is the Fermi energy. Figure III.3b shows the angle resolved photoemission

spectroscopy (ARPES) image of the Fermi surface (FS) of CeTe₃ at 25 K (from Ref. [4]). The solid and dashed black lines outline the FS, while the red and blue solid lines represent the calculated energy dispersions with a Fermi energy E_F fixed according to the filling of the orbitals expected from stoichiometry. The yellow solid squares represent the limits of the reduced BZ obtained from considering the square unit cell of a 2D Te plane, and the 45° rotated green squares represent the limits of the extended BZ obtained from the 3D unit cell. The intensity-colored regions represent ungapped portions of the FS, and the $q_{CDW} \approx 5/7c^*$ vector connects regions of gapped FS that lie outside the first Brillouin zone.

As the curvature of the Fermi surface is given by t_\perp/t_\parallel , changes in the lattice constant will cause minimal changes to the topology of the Fermi surface. However, the bandwidth, which is related to the density of states at the Fermi level $N(E_F)$, is directly proportional to t_\parallel , so $N(E_F)$ is expected to decrease with the contraction of the lattice. It is then expected that the application of pressure will reduce the lattice parameters and decrease $N(E_F)$, and consequently suppress the CDW ordering temperature, as inferred from the mean-field Equation I.29.

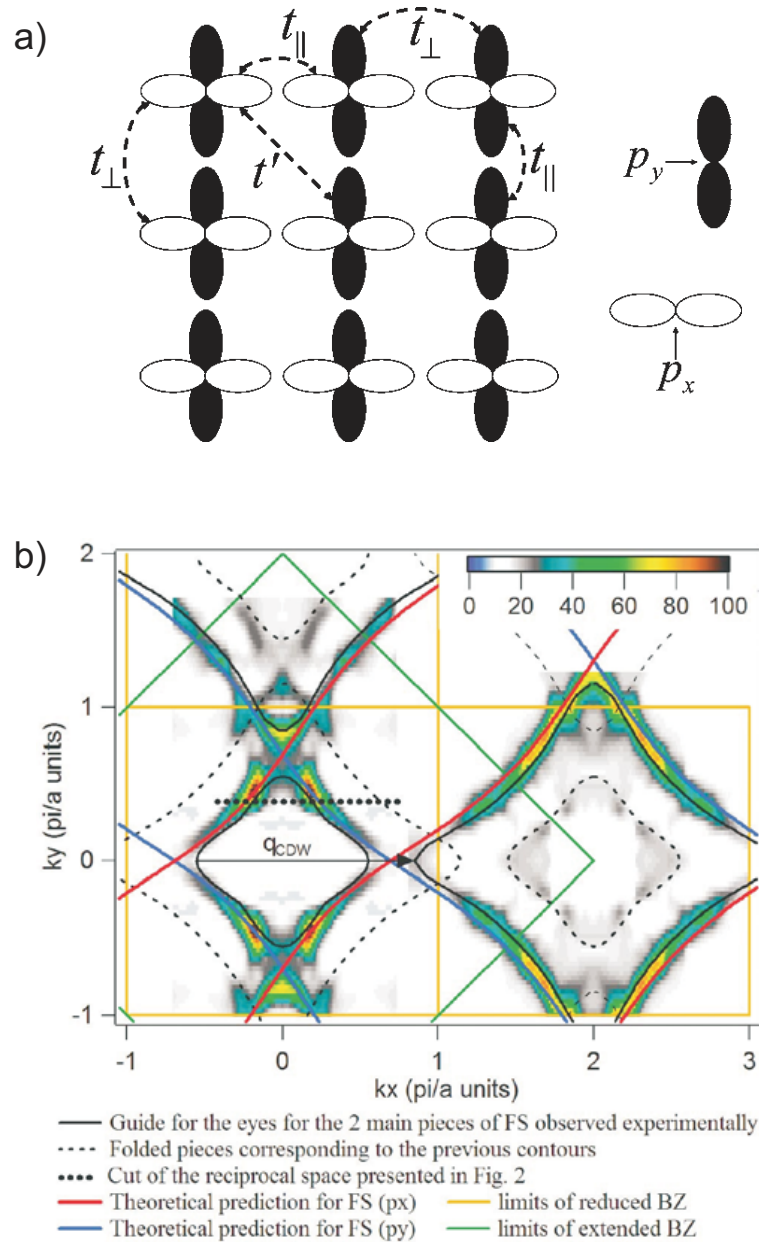


Figure III.3: (a): The p_x and p_y orbitals in the single Te square lattice (from Ref. [21]). (b): Angle-resolved photoemission spectroscopy image of CeTe₃ (from Ref. [4]). Solid and dashed black lines outline the Fermi surface. Solid red and blue lines represent the calculated energy dispersions with a Fermi energy fixed according to the filling of the orbitals expected from stoichiometry. The green solid line corresponds to the limit of the 2DBZ, while the yellow solid squares delineate the 3DBZ.

III.C Experimental Details

Single crystals of $R\text{Te}_3$ were grown in an excess of tellurium via a self flux technique [22]. The resulting crystals were malleable, micaceous millimeter-size plates, of golden color. The material is somewhat air-sensitive, and crystals must be stored in an oxygen and moisture-free environment.

Electrical resistivity measurements under pressure were performed employing two different techniques. In the first technique, pressure was applied with a beryllium-copper, piston-cylinder clamped cell using a Teflon capsule filled with a 1:1 mixture of n-pentane:isoamyl alcohol as the pressure transmitting medium to ensure hydrostatic conditions during pressurization at room temperature. The pressure in the sample chamber was inferred from the inductively determined, pressure-dependent superconducting critical temperature of a lead or tin manometers [23, 24], and reached a maximum value of 2.7 GPa. In the second technique, pressure was applied in a beryllium-copper Bridgman anvil clamped cell using solid steatite as the quasi-hydrostatic pressure transmitting medium. The pressure was determined from the superconducting transition of a strip of lead foil placed adjacent to the sample and measured using a 4-lead resistive method. With this technique, a maximum pressure of ~ 16 GPa was attained. Pressure gradients were inferred from the width of the manometer superconducting transition. These gradients were as large as 2% and 10% of the total pressure for the piston-cylinder and the Bridgman-anvil cell experiments, respectively. In all cases, the electrical resistance in the *ac*-plane was measured using a 4-lead technique and a Linear Research Inc. LR-700 AC resistance bridge operating at 16 Hz. Contacts of $\sim 2 \Omega$ were obtained after evaporating gold pads onto the surface of the samples, which also served as protection against the effect of air. Platinum or gold leads ($50 \mu\text{m}$) were attached to the gold pads with five minute silver epoxy.

The experiments at high pressure were done in two different cryostats: from room temperature to 1.2 K, a conventional ^4He bucket connected to a pump-

ing system was used, and for temperatures ranging from $0.1 \text{ K} \leq T \leq 2 \text{ K}$, an Oxford Kelvinox MX100 ^3He - ^4He dilution refrigerator was utilized, equipped with a 9 T wide bore superconducting magnet for high pressure cells.

Resistivity measurements at ambient pressure were obtained using a Quantum Design Physical Property Measurement System (PPMS) throughout the temperature range $1.8 \text{ K} \leq T \leq 20 \text{ K}$ and for magnetic fields ranging from 0 to 9 T, applied both parallel and perpendicular to the *b*-axis of the crystals.

The specific heat C was measured as a function of temperature T from 0.65 to 200 K using a ^3He semiadiabatic calorimeter and a standard heat pulse technique for magnetic fields up to 5 T applied along the *b*-axis.

III.D High-Pressure, Transport, and Thermodynamic Properties of CeTe₃

CeTe₃ is one of the light members of the rare-earth tritelluride series. At ambient pressure, an incommensurate charge-density wave forms below $T_{CDW,1}$, opening a large 400 meV gap in optimally nested regions of the Fermi surface, whereas other sections with poorer nesting remain ungapped [4]. For this reason, it was not expected to observe the onset of the CDW in the measurements of the electrical resistivity of CeTe₃ at ambient pressure.

Electrical resistivity measurements as a function of temperature for different values of applied pressure are plotted in Fig. III.4. The upper panel shows data obtained from the hydrostatic cell experiment for pressures up to 2.3 GPa, while the lower panel displays data taken in the Bridgman cell experiments described in the previous section and for pressures up to 15.2 GPa. At low pressures (hydrostatic cell, upper panel), the sample behaves as previously reported by Ru *et al.* [22], although no appreciable local minimum at 10 K has been seen for these initial values of pressure. The resistivity decreases monotonically throughout the entire temperature range, which is more evident for the highest pressures obtained

in the Bridgman-anvil cell (lower panel). Below 100 K, a broad hump denoted as T_{ρ}^* , which is clearly noticeable for the higher pressures, moves to lower temperatures to a value of 55 K at 5 GPa, after which it remains mostly unchanged for the higher pressures. This feature occurring at T_{ρ}^* is suggestive of the appearance of the charge-density-wave (CDW) order, which is supported by recent x-ray diffraction data obtained for CeTe₃ under pressure [25], where it is clearly seen that the onset of the CDW state occurs below room temperature at 3 GPa. Nevertheless, the effects of the crystalline electric field or the onset of Kondo coherence should not be ruled out, taking into account the strong hybridization of the localized 4f orbitals with the conduction band that usually takes place in cerium-based compounds. A lower temperature feature, labeled as $T_{1,\rho}$, was first reported by Iyeiri *et al.* [17] and later in the above mentioned work by Ru *et al.*. They attribute this feature to a transition to an antiferromagnetic state, given the negative Curie-Weiss temperatures obtained from magnetic susceptibility measurements. We found that this ordering temperature increases from 3 to 13 K under pressure, as can be seen in the *insets* of the upper and lower panels of Fig. III.4. No appreciable change in $T_{1,\rho}$ is observed for pressures above 5 GPa. For pressures below 2.3 GPa, power-law fits to the resistivity curves below $T_{1,\rho}$ yielded exponent values averaging 2.2 ± 0.1 .

A feature, occurring at a temperature denoted $T_{2,\rho}$, was discovered above 7 GPa for the two crystals measured in the two Bridgman experiments (Fig. III.4, lower *inset*). The features are truncated at the base temperature of 1.1 K, where the resistivity has dropped by 65% of its value at the onset of the transition. In the first Bridgman cell experiment, the drop of the resistivity was detected at 2.7 K and 15.2 GPa and it was seen again at 2.4 K and 7.5 GPa. For the second Bridgman run, $T_{2,\rho}$ remained at a value of 5.5 ± 0.1 K while increasing the pressure from 8.6 to 12.4 GPa. This suggests a possible new phase emerging at lower pressures and below the temperature range covered in this experiment. Fig. III.7 summarizes the different regions of the $T - P$ phase diagram studied in the present work.

Figure III.5 displays the electronic and magnetic contributions to the spe-

cific heat of CeTe₃ for magnetic fields up to 5 T applied along the *b*-axis of two single crystals with total mass of 7.5 mg, obtained after subtracting the phonon contribution estimated from the high temperature $C(T)$ data. The C/T versus T^2 fits yielded a Debye temperature of 161 K, comparable to previous values for LaTe₃, and an electronic specific heat coefficient γ of 52 mJ/mol-K², substantially larger than is observed for LaTe₃ [22], implying a moderately enhanced admixture of the localized 4*f* electron states of Ce with conduction electron states, as suggested in previously reported angle-resolved photoemission spectroscopy (ARPES) experiments [5, 7]. A broad feature in $C(T)$ characterizing the magnetic order that occurs at $T_{1,C}$ corresponds directly to the transition temperature $T_{1,\rho}$ obtained from electrical resistivity measurements at ambient pressure (~ 3 K). This anomaly in the specific heat remains unchanged by the magnetic fields used in this experiment. The lower *inset* in Fig. III.5 shows the electronic and magnetic contributions to the entropy at zero magnetic field, which adds up to Rln2 (indicated by a horizontal dashed line) at temperatures right above $T_{1,C}$, consistent with what is expected for a Ce³⁺-doublet ground state.

At even lower temperatures, a sharper feature is observed in the $C(T)$ data that exhibits a rather weak field dependence. This transition was not detected in the electrical resistivity experiments (down to 1.1 K). This suggests this new phase also has a magnetic origin. The transition temperature $T_{2,C}$ (defined after performing an equal-entropy analysis of the data) increases to a value of ~ 1.3 K at 2 T, and then decreases for the higher applied fields. The left panel of Fig. III.6 illustrates the evolution of this feature throughout the range of applied magnetic fields in which the specific heat measurements were made.

The above evidence associated with the low-temperature transition below 1.5 K, and the apparent lack of field dependence for the 3 K ordering temperature revealed by the specific heat data led us to inquire further into the origin of these magnetic transitions. The work by Iyeiri and co-workers previously mentioned, foretells a strong dependence of the magnetic phases of CeTe₃ with the orientation

of the applied magnetic field with respect to the crystalline axes. In order to test the angle dependence of T_1 , electrical resistivity measurements were performed down to 2 K in magnetic fields ≤ 9 T applied perpendicular and parallel to the b -axis of the crystals, and perpendicular to the direction of the current passing through the the ac -planes of the samples, utilizing a commercial Quantum Design PPMS sample rotator. The two *right* panels of Fig. III.6 show these results. With magnetic fields applied perpendicular to the planes ($H \parallel b$, *upper-right* panel), the transition temperature T_1 does not shift with applied magnetic field, consistent with the specific heat measurements, although a rather strong magnetoresistance was found ($(R_{9T} - R_0)/R_0 = 1.43$ at 10 K). On the other hand, for fields applied parallel to the ac -planes (*lower-right* panel), a negative magnetoresistance is observed, and the transition temperature T_1 moves towards zero as indicated by the arrows. The *left* panel in Fig. III.6 combines the field dependencies of $T_{1,\rho}$ for $H \parallel b$ and $H \perp b$, with the field dependence of $T_{2,C}$ with $H \parallel b$.

Although not shown in Fig. III.6 for clarity, the local Kondo-like minimum around 10 K mentioned earlier [5, 22] has been seen in this set of measurements at ambient pressure. For $H \parallel b$, this minimum appears at 9.8 K without applied magnetic field, and increases to 10.5, 12 and 13 K for 3, 6 and 9 T. For $H \perp b$, the minimum observed at zero field at 9.8 K remains unchanged for fields below 1.5 T, and then disappears for magnetic fields above 3 T.

The specific heat and transport data presented in Figs. III.5 and III.6 suggest that T_1 characterizes the onset of the transition to a magnetic phase with the *easy* magnetic axis contained in the ac -planes. The b -axis would then play the role of a *hard* axis for this magnetic phase, consistent with magnetic susceptibility measurements [17]. In the case of the transition at $T_{2,C}$, we did not measure the specific heat with the magnetic field applied parallel to the basal plane, but we can conclude that the $T_{2,C}$ magnetic *easy* axis is not parallel to the T_1 easy axis, as can be found in other anisotropic magnetic f -electron systems reported elsewhere [26], in which ferromagnetic and antiferromagnetic phases occur at different ordering

temperatures, with non-collinear ordering directions, due to the interaction of the localized f -electrons with the conduction electrons (intra-atomic exchange) and with nearby ions (inter-atomic exchange), and to the effect of crystalline electric fields.

The temperature vs. pressure phase diagram is presented in Fig. III.7. It is clearly seen that the curve $T_1(P)$ saturates to a rather constant value above 5 GPa. $T^*(P)$ also shows a kink around the same pressure, and then attains a constant value of ~ 55 K. This particular value of pressure separates the phase diagram in two regions: a low pressure region where the phase characterized by $T^*(P)$ competes with the phases below $T_1(P)$, and a high-pressure region where these three phases may coexist. The *inset* of Fig. III.7 shows the room-temperature dependence of the electrical resistance with applied pressure (compression only). An abrupt drop of the resistance occurs around 4.5 GPa. Despite the fact that this feature in the electrical resistance was observed at room temperature, the value of this pressure coincides with the kinks in the $T^*(P)$ and $T_1(P)$ curves at 5 GPa, and with the emergence of the critical temperature $T_{2,\rho}$ above 6 GPa. As we previously mentioned, in a recent work by Sacchetti *et al.* [25], x-ray diffraction experiments performed under pressure showed that the satellite peaks associated with the CDW lattice distortion disappear at room temperature when an external pressure of 3 GPa is applied. This suggests that the onset of the CDW transition is driven to lower temperatures when high enough pressures are applied to the rare-earth tritellurides. In the same report, the authors showed that the a and c lattice parameters become equal at room temperature and for pressures above 3 GPa which is indicative that a structural phase transition might be taking place near that value of pressure. Unfortunately, no x-ray data under pressure and at low temperatures has yet been reported for CeTe₃, which would definitely clarify the origin of T^* that we found in our Bridgman-anvil cell experiments.

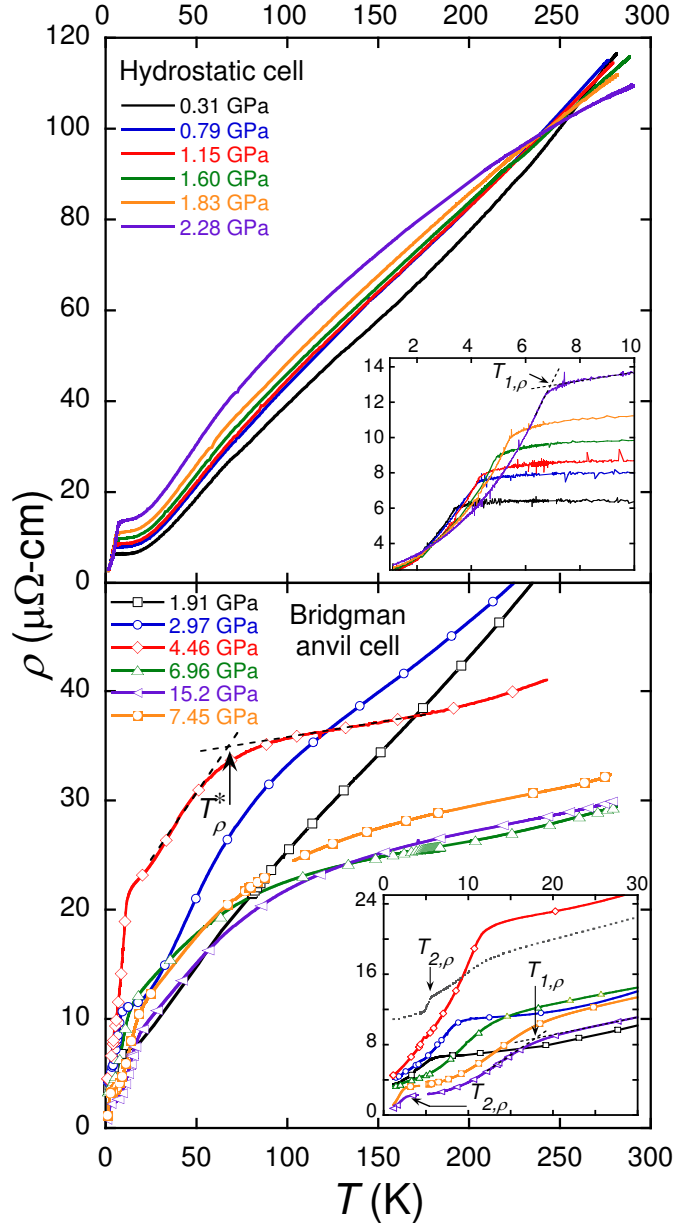


Figure III.4: Electrical resistivity versus temperature at various pressures for CeTe_3 single crystals. *Upper panel:* Hydrostatic cell experimental results. The *inset* shows the low temperature range, displaying the onset of the magnetic order as $T_{1,\rho}$. *Lower panel:* Bridgman-anvil cell results. The *inset* shows $T_{1,\rho}$, along with the new ordering temperature $T_{2,\rho}$, indicated in the figure for the first Bridgman run (for the 15.2 GPa curve) and for the second Bridgman run (*in black, dashed curve*).

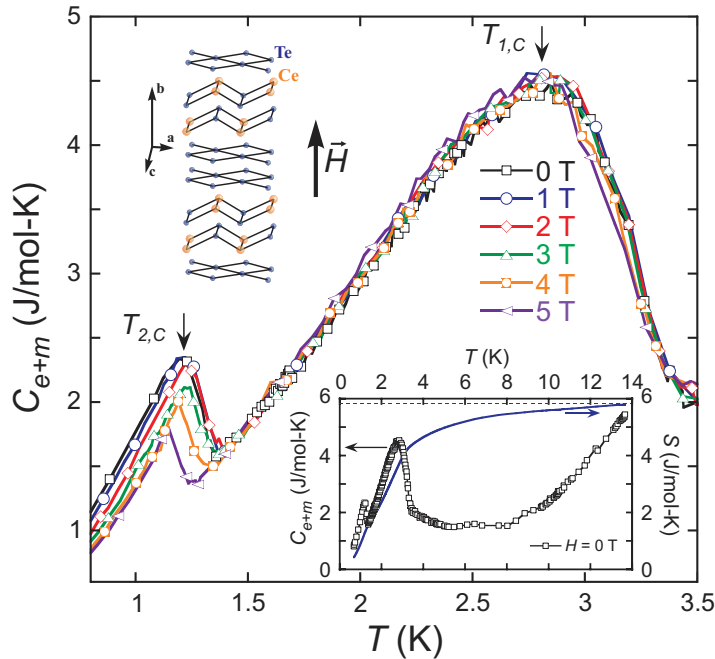


Figure III.5: Electronic and magnetic contribution to the specific heat for different magnetic fields applied along the b -axis of the CeTe₃ crystals. $T_{1,C}$ corresponds to the field-independent ordering temperature centered near 3 K, while $T_{2,C}$ denotes the field-dependent feature below 1.5 K. In the lower *inset*, the solid curve (*blue*) corresponds to the electronic and magnetic entropy in zero magnetic field and the horizontal dashed line corresponds to the value $R \ln 2$ J/mol-K. The upper *inset* shows a schematic diagram of the crystal structure of CeTe₃ and the direction of the applied magnetic field in the specific heat experiment.

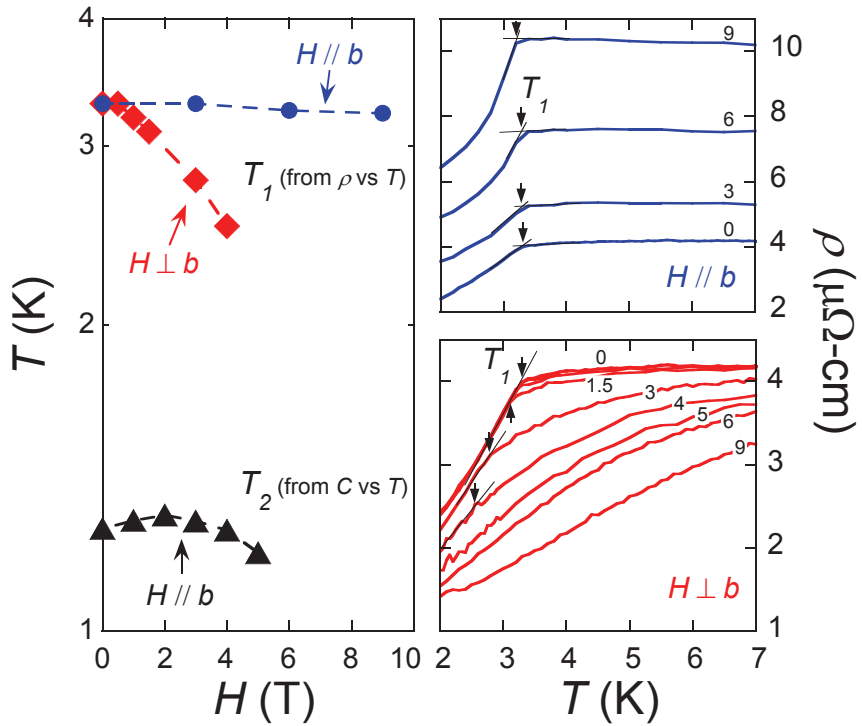


Figure III.6: *Left:* Field dependence of the magnetic ordering temperatures $T_{1,\rho}$ and $T_{2,C}$ of CeTe₃ for magnetic fields applied perpendicular and parallel to the b -axis. A logarithmic temperature scale was chosen to emphasize the curvature of T_2 vs H . *Right:* Temperature dependence of the electrical resistivity near T_1 for magnetic fields applied parallel (*upper-right*; 0, 3, 6 and 9 T) and perpendicular (*lower-right*; 0, 0.5, 1, 1.5, 3, 4, 5, 6 and 9 T) to the b -axis of the crystals. The arrows mark the position of T_1 . The numbers on each curve denote the value of the applied magnetic field in tesla. For the lower-right panel, arrows and numbers for fields of 0.5 and 1 T are not displayed for better clarity.

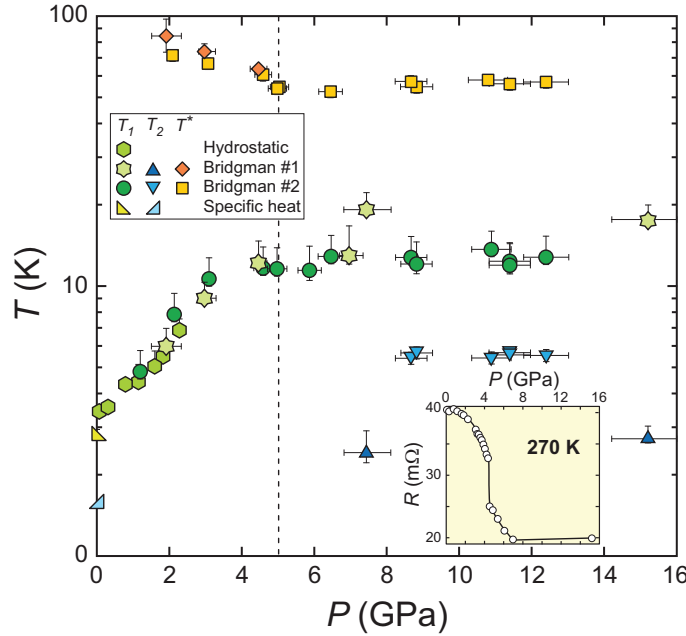


Figure III.7: Temperature T versus pressure P phase diagram for CeTe₃ (note the logarithmic temperature scale). T^* - characteristic temperature associated with the hump-like feature in $\rho(T)$, possible origins of which are discussed in the text; T_1 - magnetic ordering temperature; T_2 - ordering temperature (probably magnetic). The vertical dashed line separates the $T - P$ phase diagram into two regions in which T^* , T_1 , and T_2 all have distinctly different pressure dependences. *Inset:* room temperature evolution of the electrical resistance as the pressure was increased.

III.E Pressure Induced Superconductivity in TbTe₃

Figure III.8 displays the results of the measurements of magnetization M vs. T for TbTe₃. The upper inset to figure III.8 shows the magnetic susceptibility in the vicinity of the Néel temperature, T_N . The main panel of Fig. III.8 shows magnetization M versus applied field H measured at several temperatures both above and below T_N . For the measurements at 1.9 and 4.3 K, well below T_N , clear slope changes between 1-3 tesla appear to be associated with metamagnetic reorientation of the Tb magnetic moments. These measurements further reinforce the notion that the magnetic ordering in TbTe₃ is AFM [11]. At higher magnetic fields, we observe hysteretic jumps in the magnetization which indicate a field-induced first order phase transition.

The results of the specific heat C experiment are shown in Figure III.9. Similar to recently reported results [11], several peaks are observed near T_N . A weak upturn at the lowest temperatures is most likely due to a nuclear Schottky anomaly. Under applied magnetic fields, all three of the peaks become smaller and move down in temperature with increasing field at differing rates. The inset to Fig. III.9 shows the field dependence of these peaks. In a molecular field approximation analysis of the magnetic phase diagram of an antiferromagnet, the ordering temperature T is expected to depend on the applied field H as $T = T_N - b \cdot (H^2/T_N)$, where b is a constant [27]. The dashed lines shown in the inset to Fig. III.9 show that the data are well fitted by the above equation. Extrapolation of the fits implies that these transitions would be suppressed to zero temperature at 8.6, 6.4 and 3.6 tesla, respectively.

Figure III.10 shows the result of the nearly-hydrostatic piston-cylinder cell high-pressure measurements on TbTe₃. The onset of CDW ordering, T_{CDW} , first becomes visible at 0.3 GPa as a kink in the resistivity just below room temperature. Upon further increasing the pressure, T_{CDW} decreases monotonically to ~ 140 K at 2.3 GPa. A measurement taken on unloading the pressure from 2.3 to 1.2 GPa

indicates that the pressure dependence of T_{CDW} is reversible. A second feature below T_{CDW} is visible as a minimum in the temperature derivative of the resistivity $d\rho/dT$ (*inset* of Fig. III.10). This feature is denoted T^* . Under pressure, T^* moves to higher temperatures until, near 2.3 GPa, T_{CDW} and T^* can no longer be distinguished. It is possible that the feature at T^* is related to the appearance of a second CDW, perpendicular to the first, as observed at ambient pressure for the heavy rare earth tritellurides [11], although this will have to be confirmed through direct measurements of the lattice under pressure. Also at 2.3 GPa, a sharp drop in the resistivity, suggestive of SC, appeared near 2 K.

In order to further investigate the possibility of pressure induced SC in TbTe_3 , additional high-pressure experiments in a Bridgman-anvil cell were performed. In these measurements it was not possible to track T_{CDW} , T^* , or T_N to higher pressures because appreciable pressure gradients in the Bridgman-anvil cell lead to a broadening of the already weak resistive anomalies so that the transitions could not be unambiguously pinpointed. However, it was possible to confirm and further explore the superconducting state with the Bridgman-anvil cell data. Figure III.11 illustrates the low temperature behavior of the resistivity of TbTe_3 from both the piston-cylinder and first Bridgman anvil cell experiments. The measurement at 7.5 GPa displays a complete resistive transition to an immeasurably small resistivity below T_c , providing clear evidence that TbTe_3 becomes superconducting under pressure. Several of the measurements from the second Bridgman-anvil cell experiment also display complete resistive transitions. As determined from the transition onset, T_c reaches values as high as 3.5 K. The inset of Fig. III.11 shows the resistivity versus temperature in the vicinity of T_N at several pressures measured in the piston-cylinder cell. The Néel temperature increases monotonically with pressure over the measured pressure range. At 2.3 GPa (red curves in Fig. III.11), the AFM resistive anomaly and SC are both present.

Figure III.12 presents a summary of all the data in the form of a pressure-temperature phase diagram. The vertical dashed line near 2.3 GPa indicates the

upper pressure limit for our hydrostatic piston-cylinder cell experiments; points beyond this line were measured using the Bridgman-anvil cell technique. The lack of T_{CDW} , T^* , and T_N data points at pressures above this dashed line is due to the inability to resolve these transitions in the Bridgman cell, as discussed above, and does not necessarily indicate that the transitions are completely suppressed in this pressure region. No evidence for SC was found at ambient pressure and pressures below 2.3 GPa down to 600 mK and ~ 1.1 K, respectively. At 2.3 GPa, CDW, AFM and SC order all appear upon progressively cooling the sample.

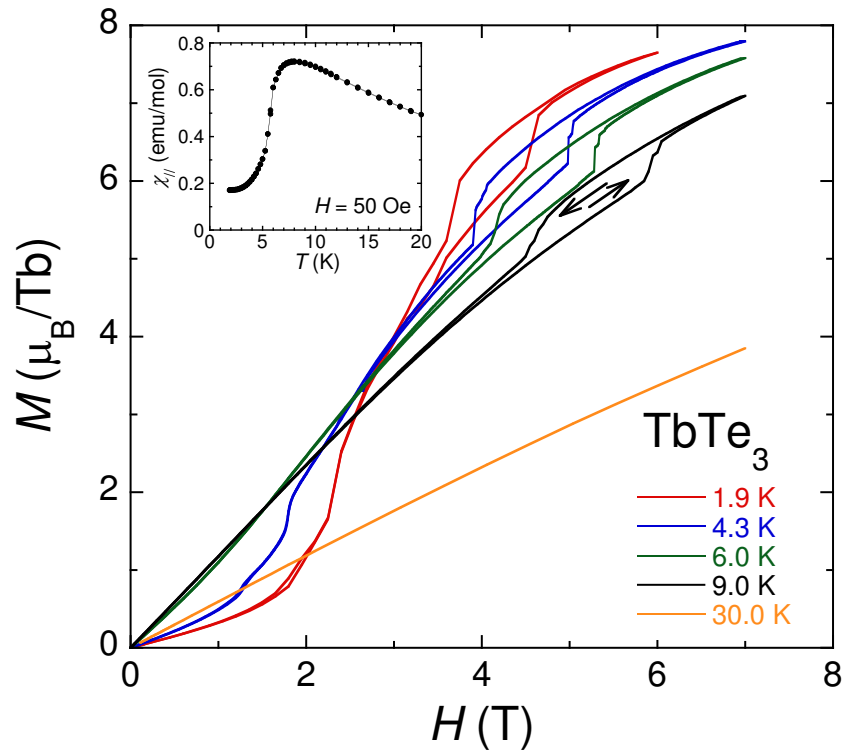


Figure III.8: Magnetization M versus applied field H at several temperatures. At temperatures below T_N , a change in slope near 1-3 T is suggestive of metamagnetism. At higher fields, hysteretic jumps in the magnetization indicate a first order phase transition. *Inset:* low temperature region where a clear drop is visible in the susceptibility, consistent with AFM ordering.

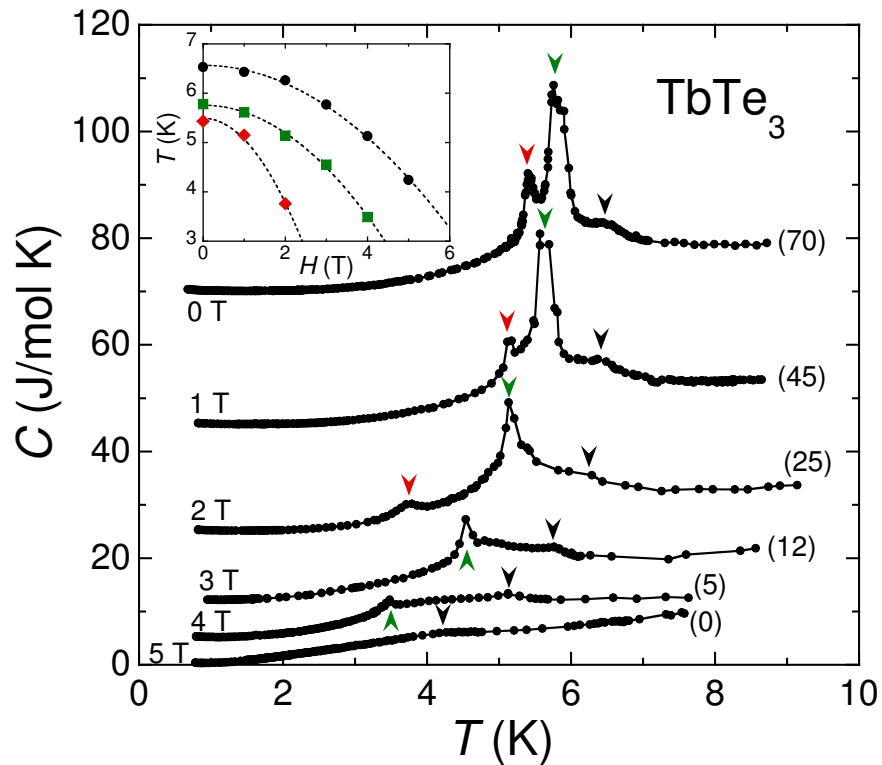


Figure III.9: Specific heat C versus temperature T for TbTe_3 at ambient pressure and fields up to 5 T. For clarity, the curves have been offset vertically by a constant amount indicated in parentheses near the right side of the curves. Three distinct peaks, indicated by arrows, are visible near the Néel temperature at 6 K. *Inset:* the field dependence of the specific heat anomalies. The dashed line fits are described in the text.

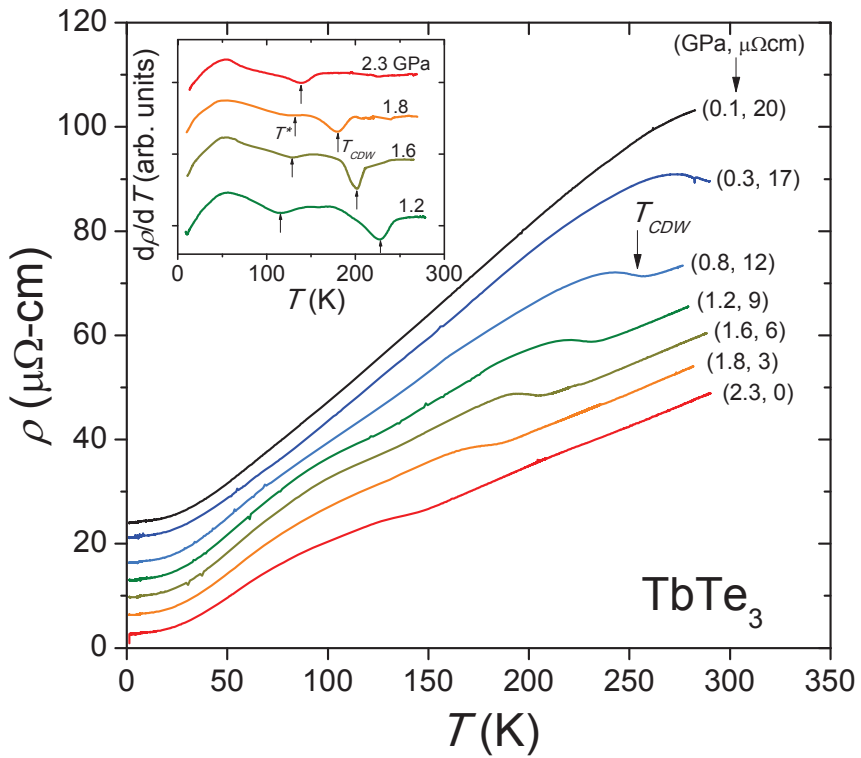


Figure III.10: Electrical resistivity measured in the *ac*-plane of TbTe_3 under nearly-hydrostatic pressures to 2.3 GPa. The curves have been offset vertically for clarity. The pressure and magnitude of the offset are indicated in parentheses at the right of the curves. The onset of the CDW at T_{CDW} is clearly seen to shift downward with pressure. At and above 1.2 GPa, a second feature in the resistivity is clearly visible at T^* as a minimum in the slope $d\rho/dT$ (*inset*). At 2.3 GPa, the two transitions T_{CDW} and T^* appear to be nearly coincident.

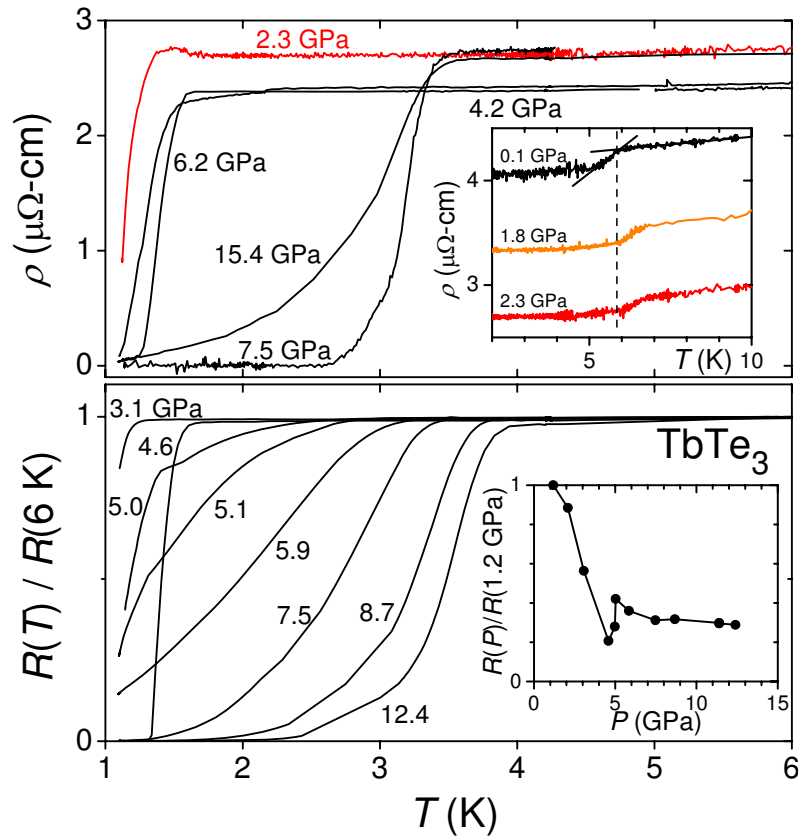


Figure III.11: Electrical resistivity measured in the *ac* plane of TbTe_3 at various pressures. The upper panel shows data from the piston-cylinder cell and first Bridgman-anvil cell experiment, while the lower panel shows data taken from the second Bridgman-anvil cell experiment. At several pressures, the resistance becomes negligible below the transition confirming superconductivity. *Upper inset:* Resistivity versus temperature in the vicinity of T_N at selected pressures. The dashed and solid black lines indicate the value of T_N at 0.1 GPa. *Lower inset:* Relative change in the 6 K resistance, taken from the second Bridgman-anvil cell experiment.

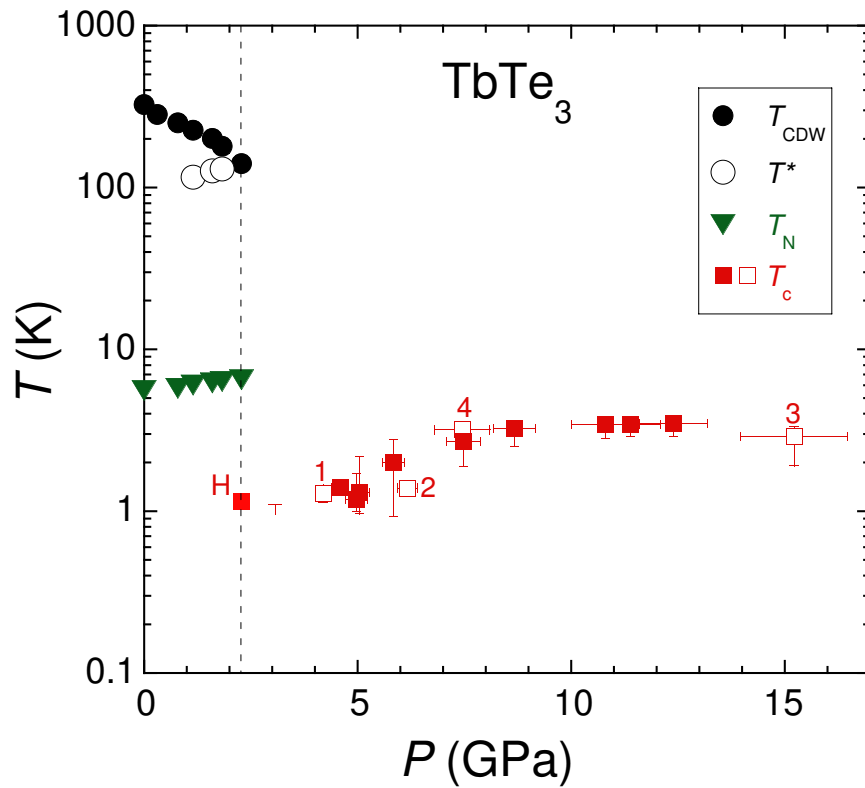


Figure III.12: Pressure dependence of the transition temperatures of the phases observed in TbTe₃. The value of T_c is given by the transition midpoint and the vertical error bars are determined by the 10% - 90% width of the transition. The point labeled 'H' is from the hydrostatic cell run. The numbers indicate the order of measurement for the first Bridgeman-anvil cell run. Open squares are from the second Bridgeman-anvil cell run.

III.F DyTe₃ and GdTe₃

Following the discovery of the pressure-induced superconductivity in the TbTe₃ samples at high pressure and its possible competition with the two charge-density-waves and magnetism, the two close neighbors of this compound were studied. At ambient pressure, the lighter GdTe₃ enters the CDW state below $T_{CDW,1} \sim 377$ K and orders magnetically at 11.3 K and 9.7 K, which are the highest Néel temperatures of the R Te₃ series. Similarly to TbTe₃, GdTe₃ does not present the second CDW order at ambient pressure. On the other hand, the heavier DyTe₃, which also develops two consecutive magnetic phases below 3.6 K and 3.44 K, shows at ambient pressure the two orthogonal CDWs below $T_{CDW,1} \sim 306$ K and $T_{CDW,2} \sim 49$ K. This suggests that superconductivity could be induced in this compound at even lower applied pressures, following the results shown in Figure III.12, where the superconducting state only emerged after the appearance of the second CDW at $T_{CDW,2}$, and its consequent shift with pressure towards $T_{CDW,1}$.

Figures III.13 and III.14 show the electrical resistivity measurements of GdTe₃ and DyTe₃, respectively, obtained from the hydrostatic clamped cell experiment up to 2.7 GPa and down to 1.2 K. For GdTe₃, a shoulder above 250 K develops for the pressures of 0.1, 0.2 and 0.7 GPa, and it appears as the clear onset to the upper CDW at $T_{CDW,1}$ for the higher pressures. Pressure shifts $T_{CDW,1}$ towards lower temperatures, reaching a value of about 150 K at 2.7 GPa. At 1.8 GPa (blue curve), a second feature below 150 K is indicative of the onset to the second charge-density-wave ($T_{CDW,2}$). It is not possible to observe the onset to the AFM state in the electrical resistivity measurements for any of the applied pressures. DyTe₃, on the other hand, displays for the lowest applied pressure of 0.1 GPa a pronounced increase in the resistivity at $T_{CDW,1}$. For this sample, the second CDW can be clearly extracted from the ρ vs. T and the $d\rho/dT$ vs. T (not shown here) curves, but only for the 0.7 GPa measurement. In the *inset* of Fig. III.14, the

onset to the antiferromagnetic order at T_N of the Dy magnetic moments appears as a low step below 4 K, similarly to TbTe_3 , although for DyTe_3 there is no clear pressure dependence of T_N .

At 2.7 GPa, both GdTe_3 and DyTe_3 display a sharp feature near 1.25 K and 1.45 K, respectively, suggesting that pressure also induces superconductivity in these compounds (Fig. III.13 and Fig. III.14, *insets*), with an approximately 100 mK-wide full transition for the DyTe_3 sample. These values of T_c are similar to the one found for TbTe_3 at a similar pressure (Section III.E). These measurements were carried out in a ${}^4\text{He}$ cryostat in which a minimum temperature of ~ 1.2 K is attainable. Lower temperatures were necessary for studying the pressure dependence of the superconducting critical temperature T_c , since at 2.7 GPa, the clamp was at the limit of maximum pressure that it is capable to withstand. Figures III.15 and III.16 present the electrical resistivity measurements for GdTe_3 and DyTe_3 , respectively, obtained in a ${}^3\text{He}-{}^4\text{He}$ dilution refrigerator for three different pressures (2.5, 1.8 and 1.2 GPa) accessed by decreasing the applied load to the clamp. In this case, it was also possible to apply magnetic field parallel to the c -axes of the samples. As it can be seen from the left-hand panels of figures III.15 and III.16, magnetic fields of the order of 50 Oe were enough to fully suppress the superconducting transition in the temperature range covered in the experiments. T_c values were determined as the temperature at which the resistivity dropped by 50%, as indicated by the horizontal dashed lines. Since it is very difficult to tune magnetic fields of the order of 10^{-4} T (1 Oe) with a large 9 T superconducting magnet, the highest T_c occurred somehow for fields other than zero, possibly due to an intrinsic offset of the magnet current supply or to remnant fields in the superconducting magnet. The values of magnetic field shown on the ρ vs. T figures are offset by the value obtained from the analysis shown on the right-hand-side panels of figures III.15 and III.16, where offset values of ~ 17 Oe were obtained after finding the symmetry line between positive and negative “renormalized” magnetic fields (within $\sim \pm 2$ Oe error). Figure III.17 displays the renormalized critical

Table III.1: Critical temperature T_c and calculated critical fields $H_c(0)$ at 1.2, 1.8 and 2.5 GPa of DyTe₃ and GdTe₃.

	P (GPa)	T_c (K)	$H_c(0)$ (Oe)
DyTe ₃	1.2	0.65	21.0
	1.8	0.86	26.2
	2.5	1.19	42.4
GdTe ₃	1.2	0.30	25.3
	1.8	0.80	16.6
	2.5	1.03	43.4

fields for DyTe₃ (*upper panel*) and GdTe₃ (*lower panel*) at different pressures. The superconducting transition widths were defined as the difference in the temperatures where the resistivity attained 10% and 90% of its normal state value right above T_c . Close to $T = 0$, BCS theory predicts [28] that the upper critical field of a type-II superconductor decreases with temperature as:

$$H_c(T) \approx H_c(0) \left[1 - 1.07 \left(\frac{T}{T_c} \right)^2 \right] \quad (\text{III.3})$$

The values of $H_c(0)$ at each pressure can be estimated using the data close to T_c and the expression $H_c(0) = -0.693(dH_c/dT)_{T_c}T_c$ [29]. The solid lines in Figure III.17 are linear fits to the actual data, while the dashed lines in the same figure correspond to the calculated $H_c(T)$ curves at low T using Equation III.3, although this treatment would only be valid if the samples were type-II superconductors. Table III.F summarizes all the critical temperatures and fields at all pressures for DyTe₃ and GdTe₃. The small critical field values indicate that the superconducting state induced by pressure in the rare-earth tritellurides is very sensitive to magnetic fields.

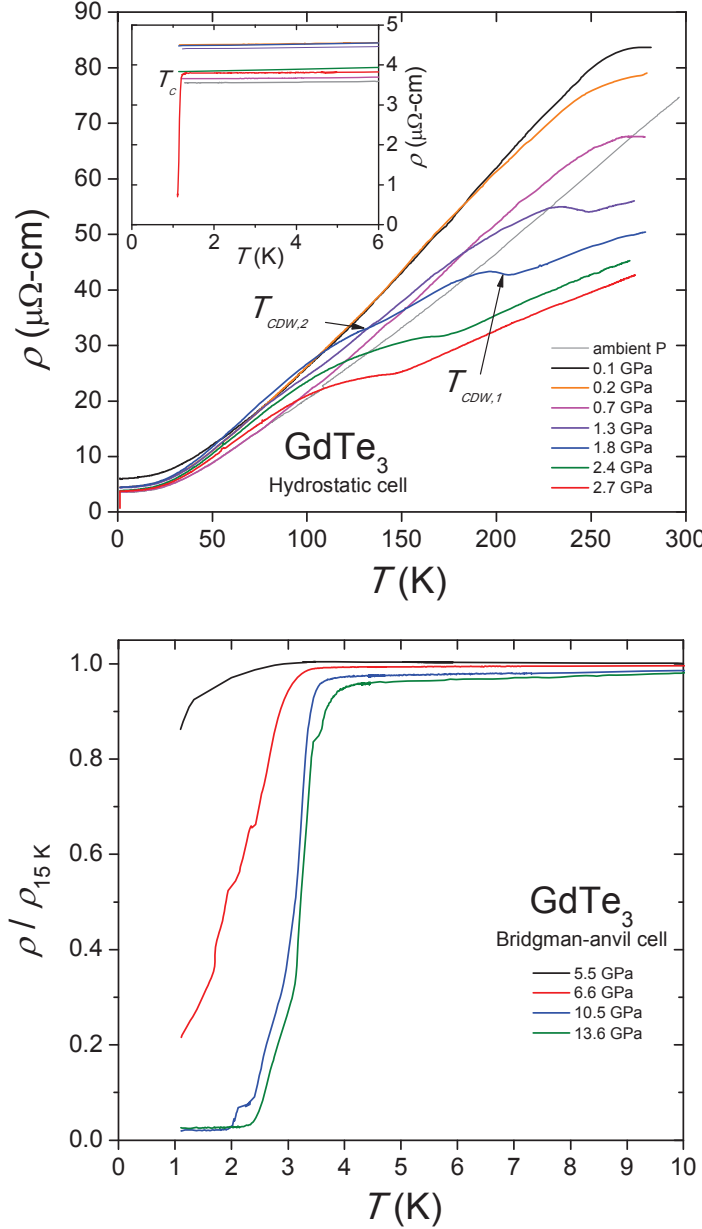


Figure III.13: Electrical resistivity of GdTe_3 . *Upper panel:* hydrostatic cell experiment. The onset to the upper CDW appears first at $T_{CDW,1}$ for the 1.3 GPa measurement. The lower CDW is only observed $T_{CDW,2}$ for the 1.3 GPa derivative of the electrical resistivity with respect to the temperature (not shown here). The *inset* displays the low temperature region, where a sharp drop at T_c is indicative of the onset of the superconductive state. *Lower panel:* Bridgman-anvil cell experiment. Curves were normalized to their respective values at 15 K.

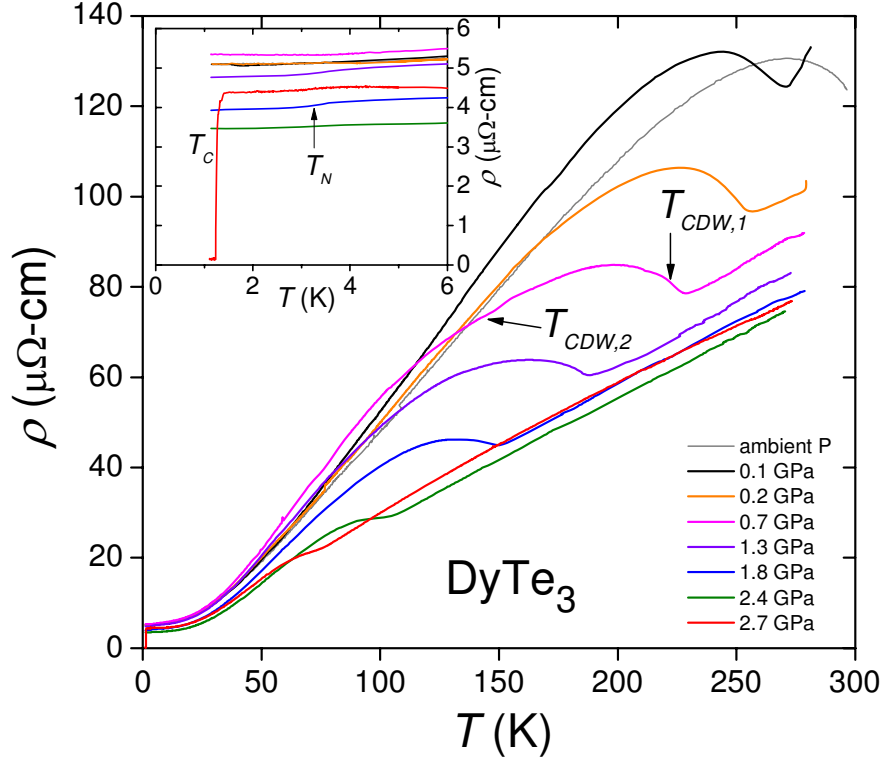


Figure III.14: Electrical resistivity of DyTe_3 from the hydrostatic experiments, up to pressures to 2.7 GPa. Since DyTe_3 is ordered in the upper CDW state at ambient pressure, the sharp feature at $T_{CDW,1}$ is observed for all the curves. The lower CDW is only observed $T_{CDW,2}$ for the 0.7 GPa derivative of the electrical resistivity with respect to the temperature (not shown here). In the *inset*, which displays the low temperature region, it is possible to distinguish a small step in the resistivity which corresponds to the onset to the AFM state. The sharp drop in the resistivity at T_c is indicative of the onset of the superconductive state.

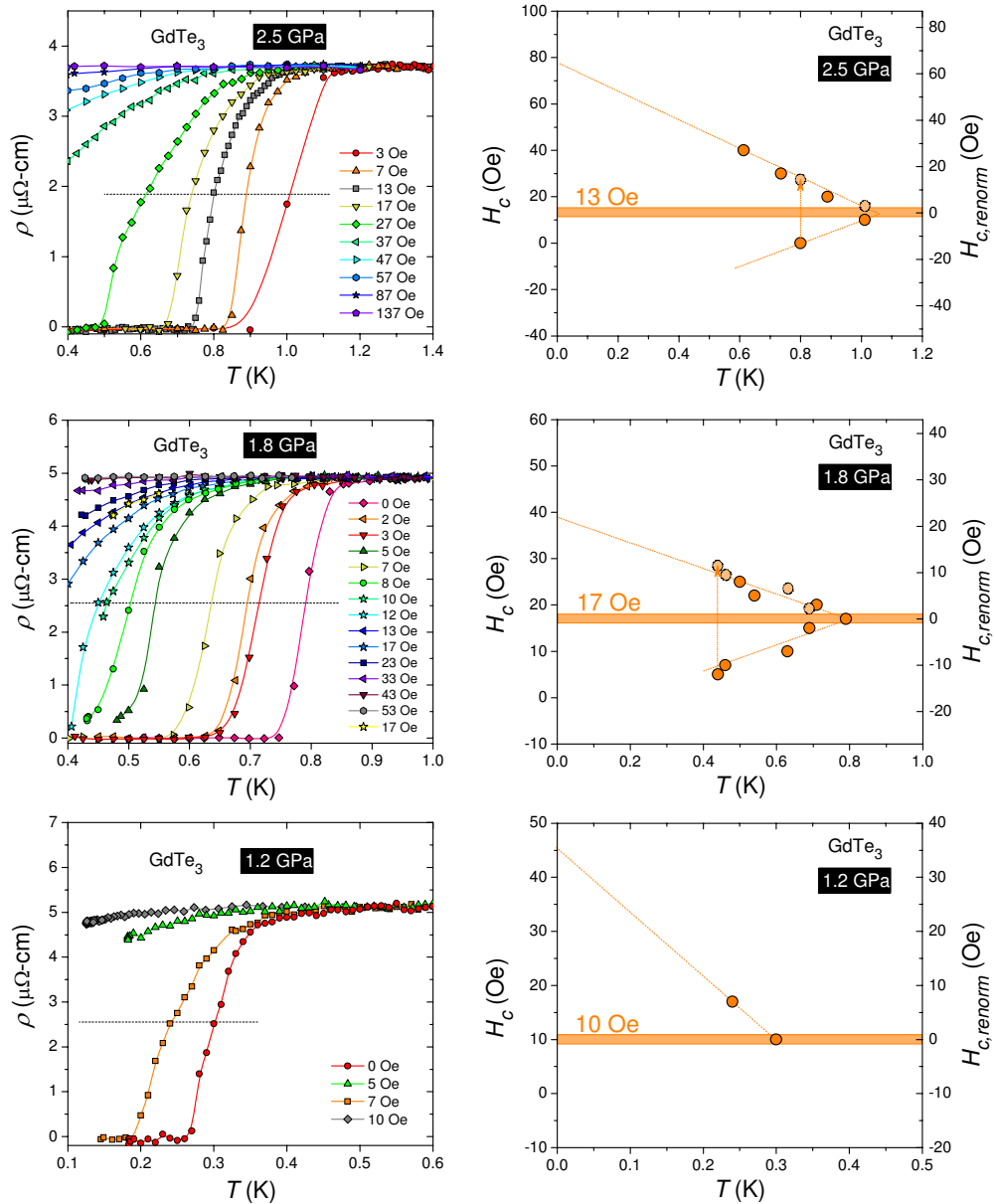


Figure III.15: *Left panels:* temperature and magnetic field dependence of the electrical resistivity close to the superconducting transition of GdTe_3 for pressures of 2.5, 1.8 and 1.2 GPa obtained in the hydrostatic cell experiments. Values of T_c were determined as the temperature at which the resistivity dropped by 50% (*horizontal dashed lines*). The values in Oe displayed in these diagrams were adjusted as described in the main text *right panels*.

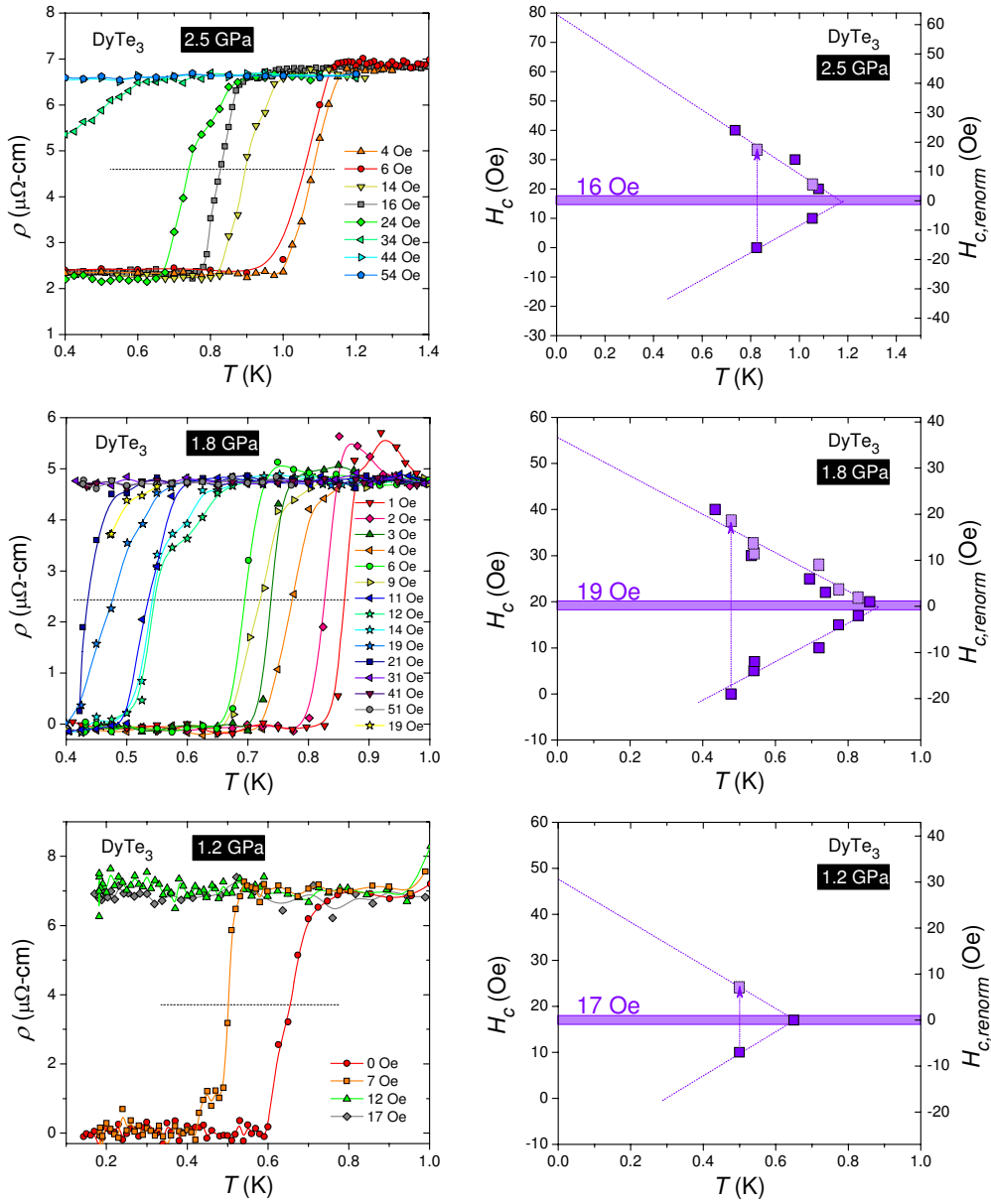


Figure III.16: *Left panels:* temperature and magnetic field dependence of the electrical resistivity close to the superconducting transition of DyTe₃ for pressures of 2.5, 1.8 and 1.2 GPa obtained in the hydrostatic cell experiments. Values of T_c were determined as the temperature at which the resistivity dropped by 50% (*horizontal dashed lines*). The values in Oe displayed in these diagrams were adjusted as described in the main text *right panels*.

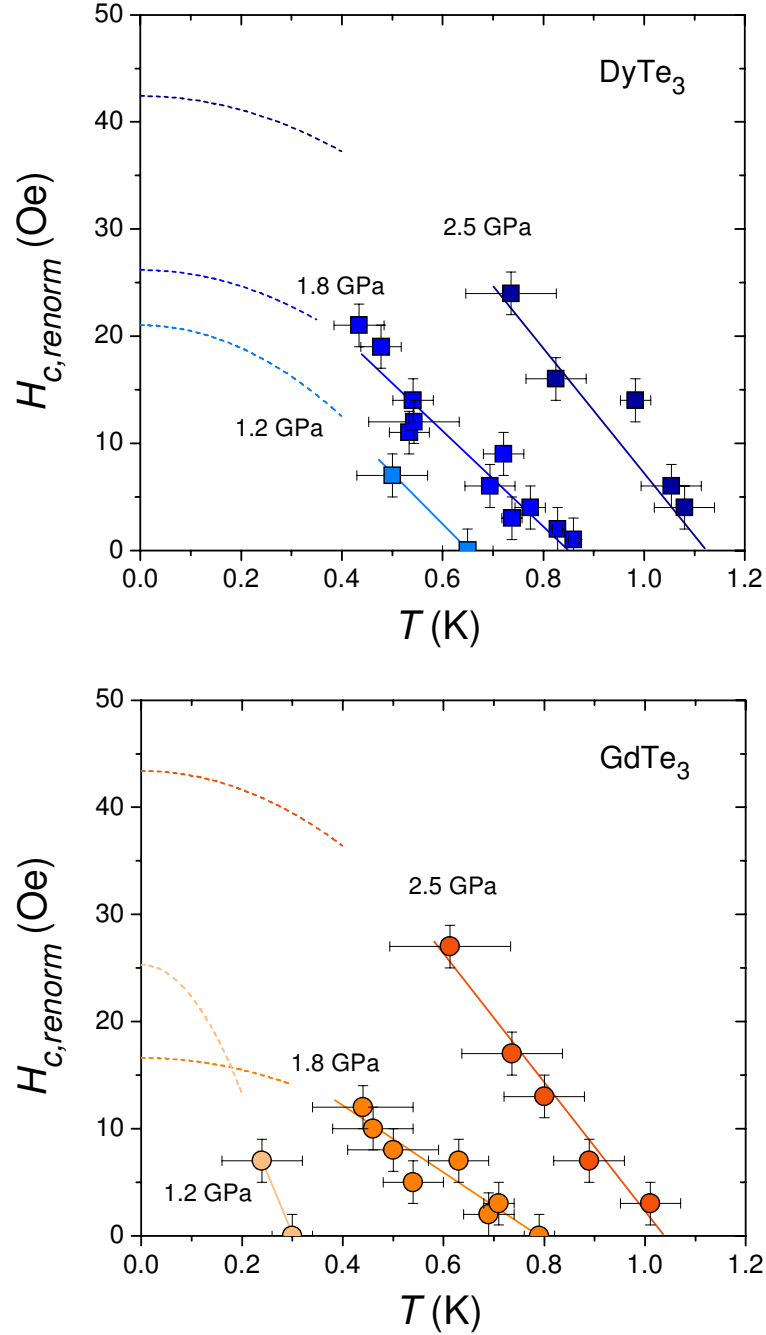


Figure III.17: Critical field H_c vs. temperature T for GdTe_3 and DyTe_3 at 1.2, 1.8 and 2.5 GPa. The renormalized values of H_c arise from a correction of the magnetic fields applied during the experiment. Solid lines correspond to linear fits to the actual data, while dashed lines are the calculated $H_c(T)$ curves for low T .

III.G Discussion

III.G.1 Pressure Evolution of the Charge-Density Wave State in $R\text{Te}_3$ Single Crystals

Figure III.18 shows the pressure evolution of the charge-density wave critical temperatures $T_{CDW,1}$ and $T_{CDW,2}$ with applied pressure for the GdTe_3 , TbTe_3 and DyTe_3 samples. T_{CDW} were obtained from the derivative curves as discussed in Section III.E. A linear suppression of $T_{CDW,1}$ with pressure for the three compounds is clearly evident, at a rate of -70 K/GPa approximately. These rates of suppression of T_{CDW} are of the same order of magnitude but higher than for other layered materials, such as NbSe_3 ($dT_{CDW}/dP \sim -45 \text{ K/GPa}$) [30], TaS_3 ($dT_{CDW}/dP \sim -30 \text{ K/GPa}$) [30], and $1T\text{-TiSe}_2$ ($dT_{CDW}/dP \sim -50 \text{ K/GPa}$) [31]. In order to compare the rate suppression of $T_{CDW,1}$ obtained with external pressure with the one shown in Fig. III.2 due the effect of chemical pressure in the rare-earth tritelluride series, one must first convert the lattice contraction to an equivalent value of externally applied pressure. From the Murnaghan equation for the pressure dependance of the lattice volume [32], the pressure ΔP needed to produce a change in volume from V_1 to V_2 is:

$$\Delta P = \frac{B_0}{B'} \left[1 - \left(\frac{V_1}{V_2} \right)^{B'} \right] \quad (\text{III.4})$$

where B_0 and B' are the coefficients of the linear bulk modulus expression $B(P) = B_0 + B'P$. From Fig. III.2, a change in $T_{CDW,1}$ from 500 K to 260 K corresponds to a compression of the lattice parameter a from 4.37 Å to 4.28 Å ($V \propto a^3$). For a value of the zero-pressure bulk modulus B_0 estimated to be 25 GPa for the rare-earth tritellurides and a derivative factor B' ranging between 4 and 8 [12], Eq. III.4 gives a rate of $dT_{CDW}/dP \sim -(120 \pm 15) \text{ K/GPa}$ for the chemically applied pressure, which is rather higher than the one obtained for external pressure. A similar result was found by Sacchetti *et al.* [12], where a higher rate of suppression of the single particle excitation energy associated with the CDW quasiparticle was found

for chemical pressure than for external pressure.

In the previously reported results on TbTe_3 , it seemed that $T_{CDW,1}$ and $T_{CDW,2}$ converged at the same point in the $T - P$ phase diagram, at a pressure which was coincident with the emergence of the superconducting state. In Fig. III.18, however, the situation seems to be different. Values of $T_{CDW,1}$ extend to even higher pressures, and even lower temperatures for the DyTe_3 sample, suggesting that the lower CDW no longer forms at temperatures higher than $T_{CDW,1}(P)$.

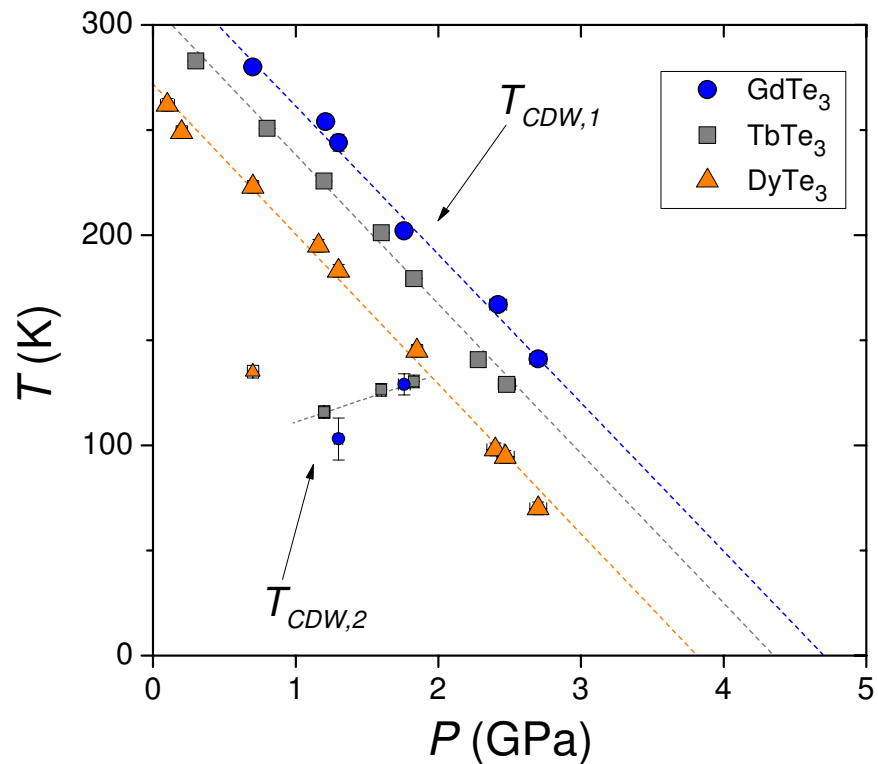


Figure III.18: Pressure dependence of the charge-density wave transition temperatures $T_{CDW,1}$ (*larger symbols*) and $T_{CDW,2}$ (*smaller symbols*) for the GdTe_3 , TbTe_3 and DyTe_3 samples. Dashed lines are guides to the eye.

III.G.2 The Superconducting State in $R\text{Te}_3$ Single Crystals

The small values of critical field presented in Section III.F imply that the superconducting state induced by pressure in these materials is very sensitive to magnetic fields. Small values of critical fields of the order of 200 Oe were recently reported in another layered compound, $1T\text{-TiSe}_2$ [31], which becomes a superconductor after suppressing a CDW state with pressure. The superconducting state induced by pressure in the $R\text{Te}_3$ and in $1T\text{-TiSe}_2$ does not seem to be very robust in comparison with, for example, NbSe_3 , which has critical fields an order of magnitude higher [33]. It has been recently speculated that such small values of upper critical field compared with heavy fermion compounds which have similar T_c but much higher $H_{c2}(0)$ could be related to the low density of states of the layered chalcogenides (for example, CeRhIn_5 has a T_c of 2.1 K with $H_{c2}(0) \sim 100$ kOe at 2 GPa) [15, 34].

Figure III.19 summarizes the superconducting transition temperatures T_c as a function of applied pressure P for the GdTe_3 , TbTe_3 and DyTe_3 samples measured in the different hydrostatic and Bridgman-anvil cell experiments described in the previous sections. For $4 \text{ GPa} \lesssim P \lesssim 6 \text{ GPa}$, T_c values for GdTe_3 and TbTe_3 jump abruptly from ~ 1.3 K to ~ 3.5 K, indicating that the high-pressure behavior differs somehow from the one at low pressures and low temperatures. Figure III.20 displays the electrical resistivity of CeTe_3 , GdTe_3 and TbTe_3 normalized to ambient pressure obtained at room temperature during loading of the pressure cells. It is evident that an abrupt drop of the resistivity occurs in the vicinity of 4 GPa, after which the resistivities of the three compounds remain fairly constant. The resistivity of the GdTe_3 sample drops by almost 100% of its value at ambient pressure. The relatively different results obtained from two distinct single crystals of TbTe_3 indicates that this effect is highly sample dependent.

The evidence presented above suggests that an unexpected effect is governing the high-pressure portion of the temperature-pressure phase diagram. Several scenarios could be taken place in the $R\text{Te}_3$ system, for example, a structural

phase transition occurring at high pressure, or the effect of impurities in the single crystals. For the first scenario, structural data can be found in recent x-ray experiments under pressure performed by Sacchetti *et al.* [25], where the authors measured the lattice parameters as a function of pressure of a sample of CeTe₃ (Fig. III.21), finding that the slight orthorhombic distortion of the unit cell that exists at ambient pressure gradually disappears as the pressure is increased, until 3 GPa where the *a* and *c* lattice parameters become indistinguishable. Despite the fact that the volume of the unit cell seems to decrease smoothly with pressure, is possible that the small changes in the *a* and *c* lattice parameters compensate one another and no appreciable jump in the volume occurs. It is then not possible to rule out a structural phase transition as being responsible for the abrupt variations in room-temperature electrical resistivity and T_c of the *RTe₃*. Moreover, the fact that the *a* and *c* lattice parameters become equal at 3 GPa might also explain why $T_{CDW,1}$ and $T_{CDW,2}$ converge close to 3 GPa. If a transformation from orthorhombic to tetragonal structure was taking place in the lattice, then this loss of broken spatial symmetry could also be responsible for the enhancement of T_c at higher pressures. The hypothetical change of structural symmetry could be favored in particular in the Bridgman-anvil cell experiments, where pressure gradients are important, and shear stresses can produce important anisotropic deformation.

The second possible scenario could be that an impurity phase is participating more strongly in the transport properties of the rare-earth tritellurides at high pressures. Since the single crystals were grown via self-flux technique, one might consider that tellurium inclusions could be present in some amount even in these high quality single crystals. Tellurium is an insulating material at ambient pressure, but becomes superconducting at high pressures [35]. Fig. III.22 summarizes the data from several high-pressure experiments performed on pure tellurium [36, 37, 38, 39]. Fig. III.22a shows that tellurium transforms from an insulator to a metal at ~ 5 GPa at room temperature, and enters a superconducting state upon cooling the sample below 4 K, reaching a maximum $T_c \sim 6$ K at 30.5 GPa [37]. The

critical field $H_c(0)$ is larger than 200 Oe at 5 GPa [36]. It seems highly probable that the abrupt decrease of the electrical resistivity in the rare-earth tritellurides measured at room temperature during compression is due to the metallization of tellurium inclusions in the samples.

One might speculate that the superconductivity in the rare-earth tritellurides could be due completely to tellurium inclusions, where a superconducting percolative path on the surface of the crystals could give rise to a zero measured resistance. Fig. III.22c shows the evolution of the superconducting transition temperature T_c of Te up to 30 GPa. After metallization, superconductivity arises at \sim 4 GPa and 2.5 K, and T_c increases rapidly to about 4.3 K at 6.3 GPa. As pressure increases, T_c falls below 3 K, until \sim 35 GPa, where a transition to a high-pressure superconducting phase occurs, as can be seen in Fig. III.22d, where T_c has a maximum value of almost 8 K. The superconducting phase of Te seems to overlap with the high-pressure portion of the $R\text{Te}_3$ $T_c(P)$ presented in Fig. III.19. Although this could explain the abrupt increase in T_c of the $R\text{Te}_3$ described above, it still remains unclear whether the superconducting phase of hypothetical inclusions of tellurium could extend to even lower pressures, eliminating the possibility that an intrinsic superconducting phase could actually be induced by pressure in the rare-earth tritellurides. For example, Fig. III.22b exhibits the known high-pressure structural phases of Te. The straight line that separates the insulating Te-I (hexagonal) and the metallic Te-II (monoclinic) phases (from approximately 2.8 GPa and 730 K to 4.4 GPa and 290 K) has a clear negative slope, which indicates that pure Te is still insulating below room temperature at pressures below \sim 5 GPa, that is, inside the low-pressure superconducting region of the $R\text{Te}_3$ $T - P$ phase diagram displayed in Fig. III.19.

In order to shed light on this issue, additional experiments were performed. A sample of tellurium was measured to lower pressure and temperature. Figure III.23 shows the electrical resistivity of a high-purity Te sample at 1.2 GPa. This sample was measured along with a single crystal of TbTe_3 , in the same condi-

tions of the previous experiments. The Te sample does not show metallic behavior, and no signs of superconductivity were found down to ~ 150 mK. In contrast, at the same pressure, the electrical resistivity of the TbTe₃ single crystal drops almost to zero below 1 K, similarly to the GdTe₃ and DyTe₃ samples measured at the same pressure.

A test for bulk superconductivity was attempted using the ac-calorimetry technique described in Section II.C.3. In this experiment, a single crystal of TbTe₃ was pressurized to 2.4 GPa, and the electrical resistivity and the heat capacity were measured during the same cool-down. The resistivity leads and the thermocouple were glued to the sample as it is shown in Fig. II.6. In order to test the ac-calorimetry technique and to find the best frequency for this specific thermocouple-heater set-up, the AFM transition at $T_N \sim 6.5$ K was first measured, as it is displayed in Fig. III.24. A sharp peak in the heat capacity was found at the same temperature as the feature found in $\rho(T)$ at T_N . In the attempts to find similar results at the superconducting transition temperature T_c , no indications of a jump in the heat capacity were found down to 300 mK, which might be an indication that TbTe₃ is not a bulk superconductor. However, a rough estimate of the size of the expected jump in the specific heat indicates that the feature could have been buried in the intrinsic noise of the measurement. From Fig. III.9, it is possible to estimate the coefficient γ of the electronic component of the specific heat, which is ~ 0.1 mJ/mol-K². From the well-known weak-coupling BCS formula $\Delta C/\gamma T_c = 1.43$, one can infer that for $T_c \sim 1$ K, the size of the expected superconducting jump in the specific heat would be $\Delta C \sim 140$ mJ/mol-K, which is almost three orders of magnitude smaller than the jump measured at T_N with the semiadiabatic calorimeter and a standard heat pulse technique. A feature of this magnitude could be extremely difficult to detect in ac-calorimetric experiments performed in the high-pressure cells, where the adiabatic condition is clearly violated.

A superconductor is a perfect diamagnet below T_c . Thus, its magnetic susceptibility $\chi = \partial \vec{M} / \partial \vec{H} \approx \vec{M} [\text{emu/cm}^3] / \vec{H} [\text{Oe}] = -1/4\pi$ in the ordered state.

Several pieces of TbTe₃ (total mass of 0.86 mg) cut from one single crystal were loaded in one side of the secondary coils described in Section II.C.2, and a disc of Sn on the opposite secondary coil (0.44 mg), as it is illustrated in the cartoon of the upper panel of Fig. III.25. This secondary coil system was then loaded in a hydrostatic piston-cylinder clamp under the same pressure conditions as described previously. This device has a coil built in the main body of the clamp, which can be used as the primary coil for the ac-susceptibility technique. The Sn disc served, on the one hand, as the pressure manometer, and on the other hand, to compare the susceptibility jump of the TbTe₃ samples with respect to the one of a well known superconductor. Fig. III.25 displays the results obtained at 1.75 GPa. In the upper panel, the data was measured with a LR-700 resistance bridge operating at 16 Hz and 100 μ A, while in the lower panel, the voltage was measured with a SR-830 lock-in amplifier, with a sinusoidal excitation of 26 μ A and 16.6 Hz, pre-amplifying the measured signal by 100. The upper panel shows that, upon cool down, the voltage detected by the secondary coils first drops just above 3 K, indicative of the onset to the superconducting state of the Sn sample, and that an opposite and larger jump takes place below 1 K, consistent with the T_c of TbTe₃ at 1.75 GPa. Knowing that the densities of Sn and TbTe₃ are 7.365 g/cm³ and 7.602 g/cm³, respectively, the calculated volumes of Sn and TbTe₃ samples utilized in this experiment were $0.597 \cdot 10^{-4}$ cm³ and $1.13 \cdot 10^{-4}$ cm³, respectively. Assuming that the Sn sample displayed full shielding of the magnetic field (100%), we estimate that the jump occurring below 1 K corresponds to $\sim 70\%$ shielding for the TbTe₃ samples. This value could be closer to 100% if we consider that most of the TbTe₃ samples were located off-centered with respect to the coils. In the lower panel of Fig. III.25, the ac-susceptibility of TbTe₃ is shown around T_c for different applied fields, giving the critical field H_c vs. T_c phase diagram displayed in the *inset*. We believe that the down-step occurring at the onset of T_c for all the curves is due to the proximity of the Sn sample in the coils set-up. Overall, these data give important evidence that supports the scenario in which the rare-earth

tritellurides present bulk superconductivity at low pressures.

The temperature versus pressure phase diagram of the superconducting rare-earth tritellurides is shown in Figure III.26. In order to facilitate the illustration of all the phases, the temperature axis has been plotted on a logarithmic scale. The high temperature behavior is clearly established, with the upper charge density wave(CDW) first appearing upon cooling the samples at $T_{CDW,1}$, and decreasing linearly with pressure at a rate of -70 K/GPa. The lower CDW temperature $T_{CDW,2}$ seems to slightly increase with pressure until it meets with the $T_{CDW,1}(P)$ line, disappearing at higher pressures. $T_{CDW,1}(P)$ continues decreasing below 100 K, and its characteristic feature can no longer be distinguished above 2.7 GPa, the highest value of pressure reached in the hydrostatic clamped-cell experiments. At low temperatures, two possible scenarios might be taking place, as inferred from the evidence presented in previous sections. In the first scenario, the low temperature phase would be entirely due to the superconductivity of the rare-earth tritellurides single crystals, or due to the superconductivity of inclusions of Te in the $R\text{Te}_3$ samples. In the second scenario, the imaginary line $T_{CDW}(P)$ extrapolated to lower temperatures appears to end at the top of the low-pressure region of the superconducting phase diagram, called “SC1”. This region has a dome-like shape, intrinsic to the $R\text{Te}_3$ system, typical of materials where a second-order phase transition is suppressed by pressure, magnetic field or chemical composition, giving rise to a low-temperature superconducting phase. At higher pressures, this “SC1” phase would overlap with the region denominated “SC2”, due to either the superconductivity arising from percolative tellurium inclusions on the samples, or to a high-pressure superconducting phase of the $R\text{Te}_3$ arising above a structural phase transition, as it was previously discussed. The solid black line indicates the superconductive transition temperatures of Te shown before in Fig. III.22c, which lies over the T_c ’s of the $R\text{Te}_3$ in the same pressure range. The red diamond symbols at high temperature, correspond to the insulator-to-metal transition line of Te discussed in the previous section (Fig. III.22b). The red dashed guiding

line, curved in the log- T scale, seems to extrapolate to lower temperatures to the pressure where the jump to higher T_c occurs in the $R\text{Te}_3$.

If the phase diagram corresponding to the second scenario presented in Figure III.26 was correct, and the $R\text{Te}_3$ system displayed superconductivity below the “SC1” dome-shaped boundary, this would suggest that the charge-density wave states and the superconducting state intrinsic to the $R\text{Te}_3$ are competing for Fermi surface states. Due to this competition, one could speculate that the primary pairing mechanism for the superconductivity intrinsic to the $R\text{Te}_3$ would be the electron-phonon interaction, forming an s -wave singlet SC. It is possible that this competition may be understood in terms of a Bilbro-McMillan partial gaping scenario [40] in which the SC and CDW compete for the Fermi surface and, when the CDW is suppressed, SC is enhanced as additional Fermi surface becomes available to the superconducting state. This scenario is widely found in other materials, such as the layered chalcogenides $1T\text{-TiSe}_2$ [31] and NbSe_3 [33], or the single element actinide $\alpha\text{-U}$ [41], as it was mentioned in previous sections (Section I). Also, this scenario suggests that the $R\text{Te}_3$ compounds under pressure could likely be magnetically ordered superconductors in which long range AFM order coexists with SC. If that were the case, it would be interesting if the magnetic order associated with the localized f electrons of the rare-earth ions would not be affected by the CDW and SC order. We expected to observe a de Gennes’ scaling of the T_c values with the T_N for the different $R\text{Te}_3$ [42]. At a same or similar pressure, the T_c ’s of GdTe_3 , TbTe_3 and DyTe_3 do not follow de Gennes’ scaling, or at least, the values of T_c are so close to each other it is not possible to distinguish a trend within the error in determining the pressure of the different experiments. It would be illuminating to follow T_N to pressures above 3 GPa to determine its evolution and relation to SC. If T_N drops below T_c , measurements in the superconducting state could reveal T_N through, for example, the upper critical field H_{c2} versus temperature curves, which can be either enhanced or depressed below the Néel temperature [43], or through features in the specific heat. A systematic study

of the remaining rare-earth tritellurides under pressure ought to be performed in order to determine whether they also display SC and if the T_c values follow a de Gennes' scaling.

It would also be interesting to perform ac-susceptibility measurements in the high-pressure region. If the superconducting jump observed at low pressure (1.75 GPa, Fig. III.25) was not present above 5 GPa, that would suggest that the superconductivity of the rare-earth tritellurides is limited to the low pressure region "SC1", and that the superconductivity at high pressures is entirely due to tellurium inclusions.

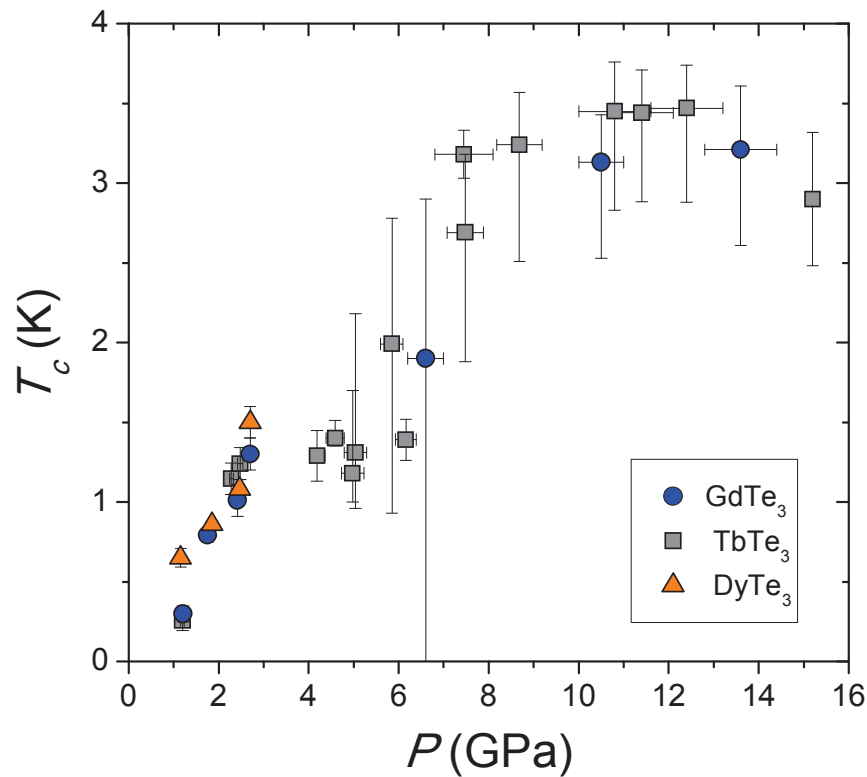


Figure III.19: Pressure dependence of the superconducting transition temperatures T_c for the GdTe_3 , TbTe_3 and DyTe_3 samples. Data below 3 GPa were obtained in the hydrostatic clamped-cell experiments, while higher pressure data were obtained from the Bridgman-anvil cell experiments.

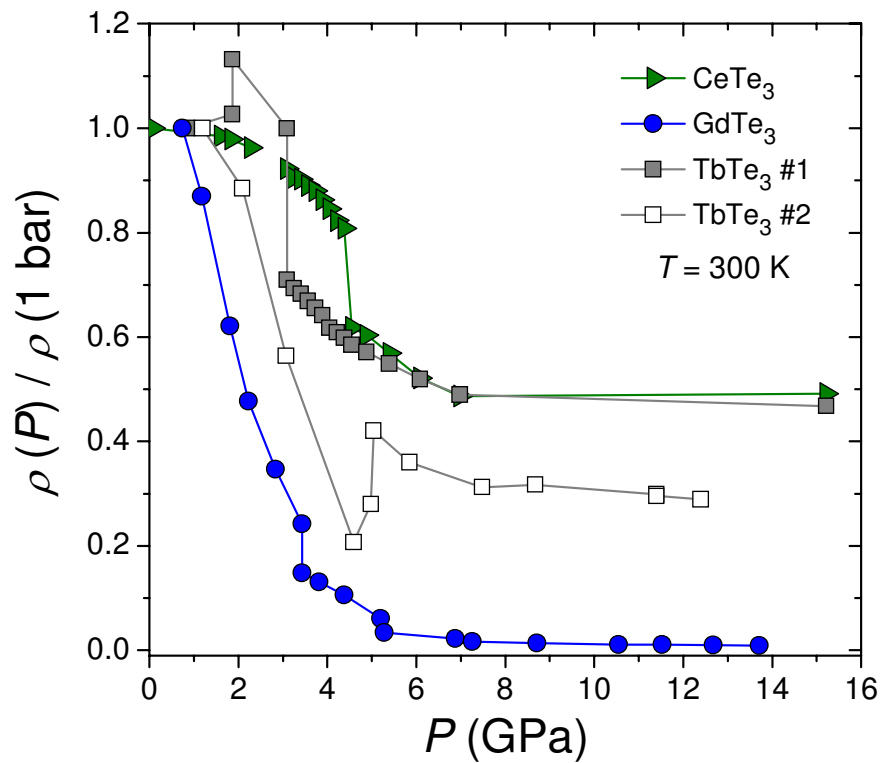


Figure III.20: Room-temperature electrical resistivity ρ as a function of applied pressure normalized to ambient pressure, obtained during pressurization of the cells. For TbTe_3 , two sets of data are presented since complementary measurements were performed in two separate Bridgeman-anvil cell runs.

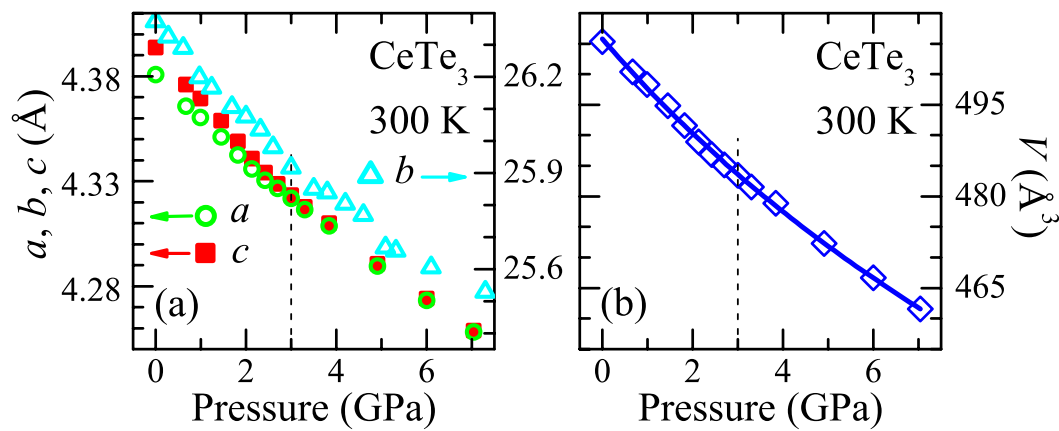


Figure III.21: Lattice parameters (a) and unit cell volume (b) for CeTe₃ at 300 K as a function of pressure (from Ref. [25]).

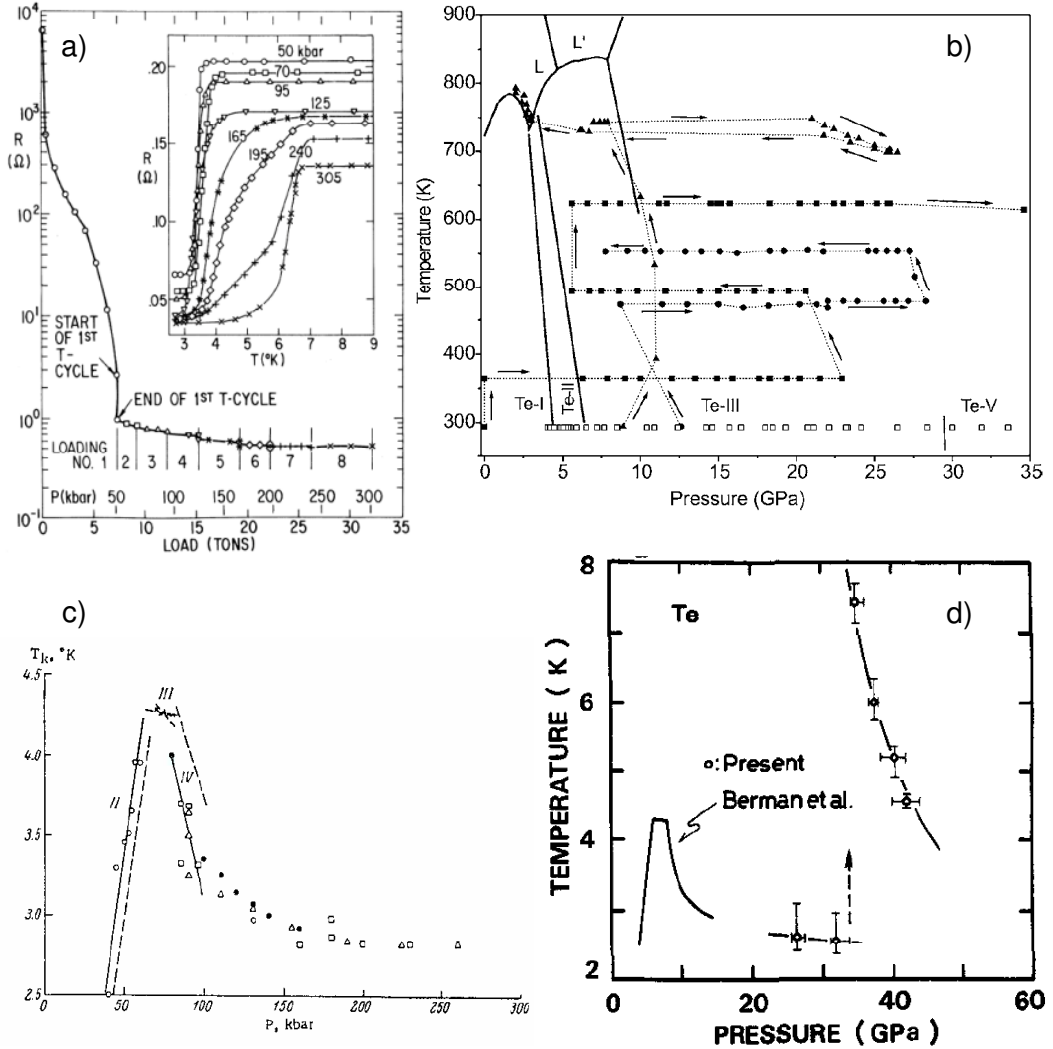


Figure III.22: The pressure dependence of tellurium. (a) Room-temperature electrical resistance vs. applied load and pressure. The *inset* shows $R(T)$ at various pressures in the superconducting transition temperature region (from Ref. [37]). (b) High-temperature and high-pressure phase diagram. The line between the Te-I (insulating) and Te-II (metallic) phases suggests that below 300 K, Te metal might be an insulator at pressures below 4 GPa (from Ref. [38]). (c) Superconducting temperature T_c of tellurium metal at various pressures below ~ 25 GPa (from Ref. [36]). (d) More recent T_c vs. P phase diagram of tellurium, up to ~ 40 GPa (from Ref. [39]).

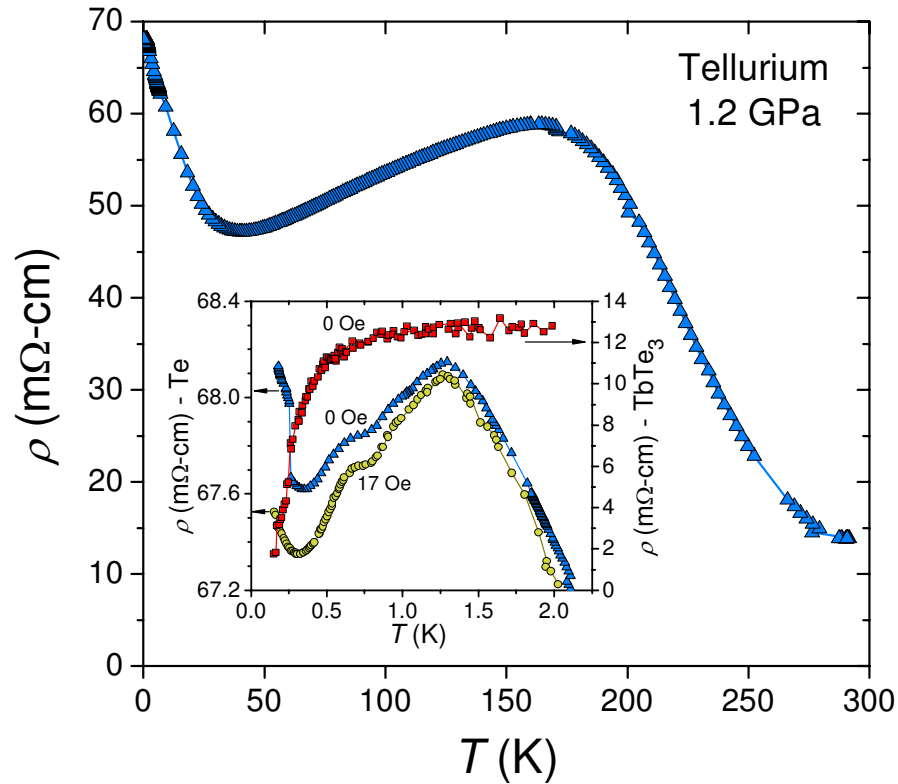


Figure III.23: Electrical resistivity of pure tellurium at 1.2 GPa obtained from the experiment carried out in the dilution refrigerator down to ~ 150 mK. The *inset* shows in more detail the low temperature region for the tellurium and TbTe₃ samples measured simultaneously in the same pressure cell. From these measurements, no indication of metallic nor superconducting state was found for the tellurium sample at this pressure, whereas the TbTe₃ sample measured at the same pressure displayed superconductivity.

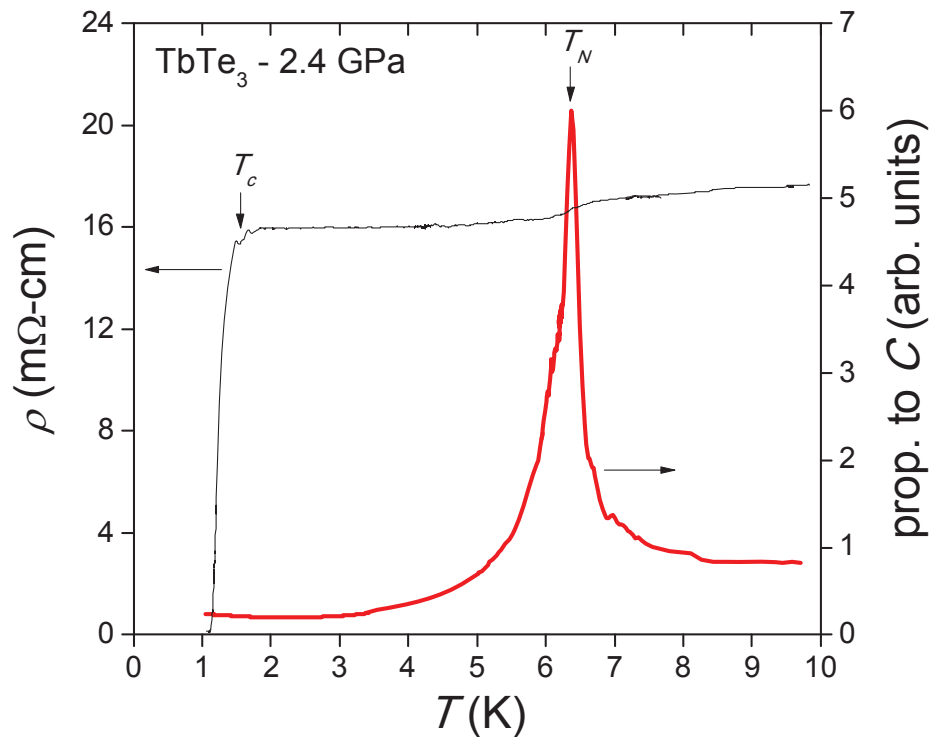


Figure III.24: Electrical resistivity ρ (*left axis*) and ac-calorimetry heat capacity C (*right axis*) versus temperature T for a TbTe_3 single crystal under 2.4 GPa of applied pressure in the hydrostatic clamp. Both measurements were taken with the same sample, in the same set-up. At 6.5 K, the AFM transition at T_N is clearly observed with both techniques. The superconducting transition is observed at T_c in the electrical resistivity only.

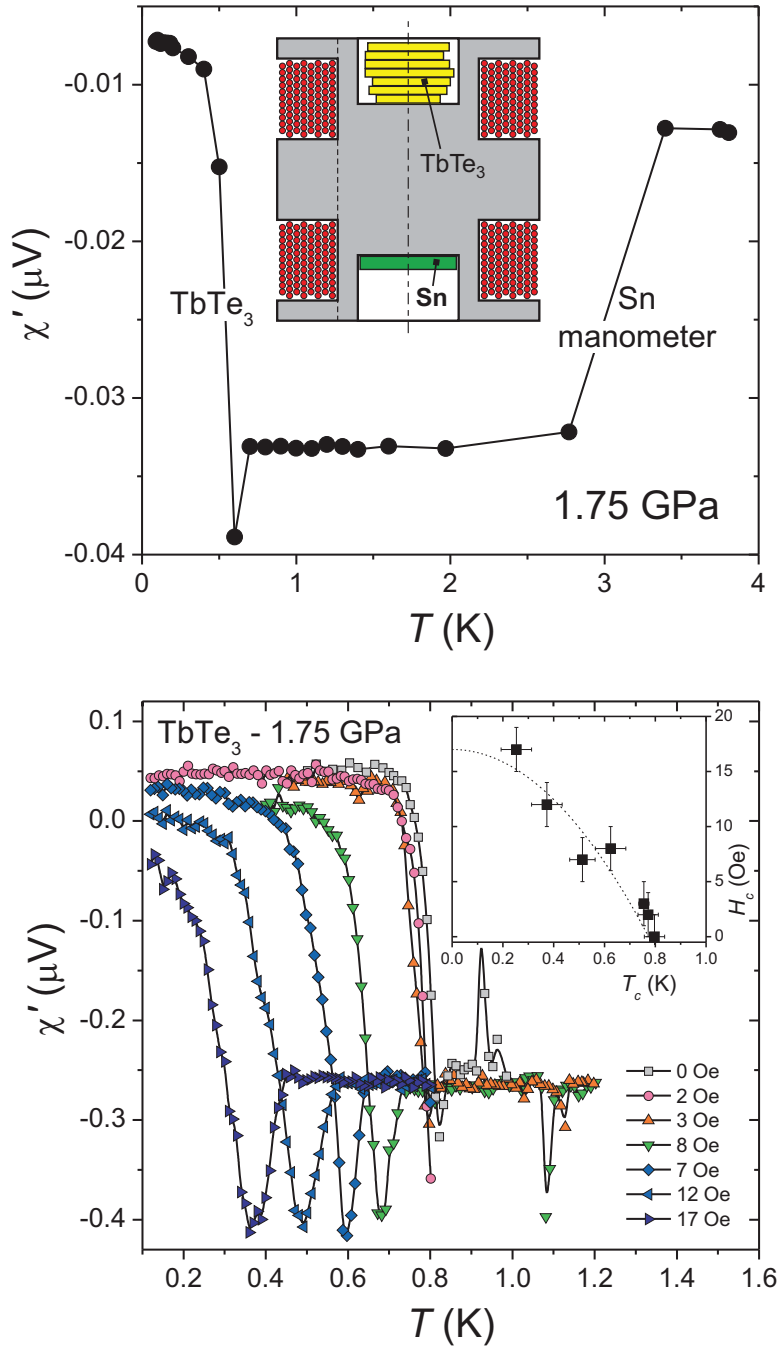


Figure III.25: *Upper panel:* AC susceptibility χ (in μV) for a sample of superconducting Sn and several samples of TbTe_3 loaded in opposite sides of the secondary coils as it is displayed in the cartoon. *Lower panel:* The superconducting transition of TbTe_3 at different applied magnetic fields. The *inset* displays the resulting H_c vs. T_c phase diagram.

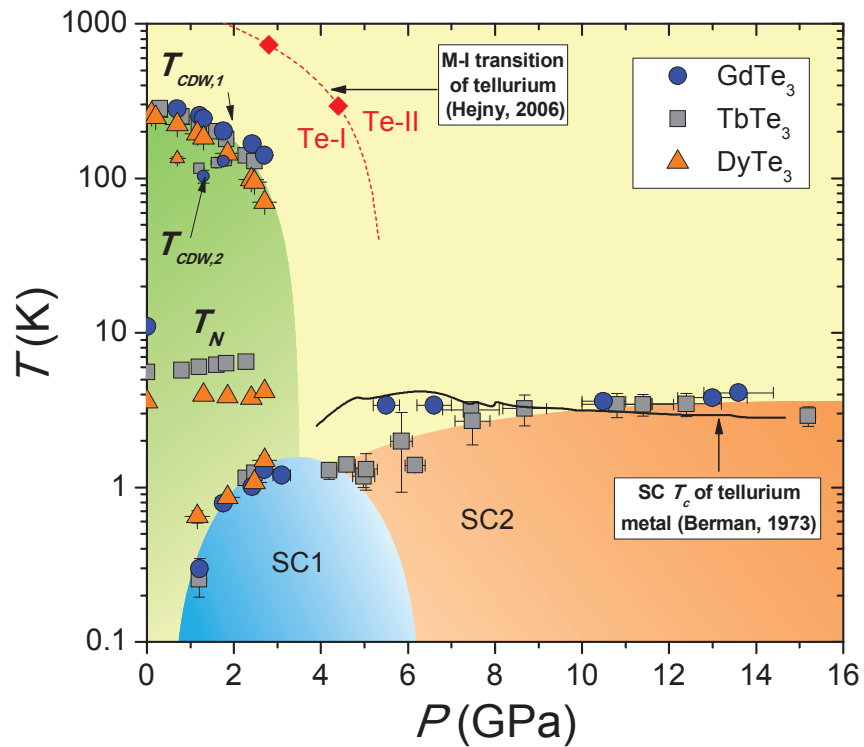


Figure III.26: $T - P$ phase diagram for the superconducting $RT\text{e}_3$. The charge-density wave temperature $T_{CDW,1}$ is suppressed with pressure, and its corresponding feature can no longer be distinguished from our measurements above 2.7 GPa. At intermediate temperatures, magnetism from the rare-earth ions is present at T_N . At lower temperatures, a superconducting phase appears at 1.2 GPa and $T_c \sim 0.3$ K, and reaches a maximum value of T_c of 3.5 K at 12 GPa. The possible origins of the superconducting phases are discussed in the main text. The black line corresponds to the Te data from Ref. [36], and red diamonds are from Ref. [38].

III.H Summary

The electric, magnetic and thermodynamic properties of the CeTe₃, GdTe₃, TbTe₃ and DyTe₃ has been studied at low temperatures and under high pressure. For CeTe₃ single crystals, the experiments yielded evidence for two magnetic phases detected in electrical resistivity and specific heat measurements at low temperatures, with non-parallel magnetic easy axes. It was also reported the emergence of a phase at high pressures and low temperatures and a possible structural transition detected at room temperature and at 4.5 GPa, which could be related to the reduction in the CDW transition temperature, illustrating that external pressure plays a key role in establishing the phase diagram of the highly anisotropic rare-earth tritellurides.

For the GdTe₃, TbTe₃ and DyTe₃ single crystals the effect of pressure on the charge-density wave and magnetic ordering temperatures was determined, and the emergence of superconductivity in the rare-earth tritellurides was observed at 1.2 GPa. Two possible scenarios that describe the origin of the superconducting phase were presented. In the first scenario, the superconductivity is due only to Te inclusions in the samples. In the second scenario, the temperature-pressure phase diagram is formed by a low-pressure superconducting phase “SC1” which is intrinsic to the rare-earth tritelluride system, and by a high-pressure superconducting region “SC2”, probably characteristic of the percolative effects of inclusions of tellurium in the samples. Further tests at low temperatures will be performed in order to shed light to this matter.

Superconductivity and charge-density waves are both collective electronic phenomena that originate from electron-phonon coupling (at least in the conventional BCS-theory picture), and the concept of Fermi surface competition between these two collective states is one of the most fundamental problems of condensed matter physics. The rare-earth tritellurides $R\text{Te}_3$ offer an excellent opportunity to study the competition of strongly correlated electronic ground states, such as

superconductivity, magnetism, and charge-density waves.

Bibliography

- [1] G. Grüner, *Density Waves in Solids* (Addison-Wesley, Reading, MA, 1994).
- [2] A. Fang, N. Ru, I. R. Fisher, and A. Kapitulnik, Phys. Rev. Lett. **99**, 046401 (2007).
- [3] E. DiMasi, M. C. Aronson, J. F. Mansfield, B. Foran, and S. Lee, Phys. Rev. B **52**, 14516 (1995).
- [4] V. Brouet, W. L. Yang, X. J. Zhou, Z. Hussain, N. Ru, K. Y. Shin, I. R. Fisher, and Z. X. Shen, Phys. Rev. Lett. **93**, 126405 (2004).
- [5] V. Brouet, W. L. Yang, X. J. Zhou, Z. Hussain, R. G. Moore, R. He, D. H. Lu, Z. X. Shen, J. Laverock, S. B. Dugdale, N. Ru, and I. R. Fisher, Phys. Rev. B **77**, 235104 (2008)
- [6] B. K. Norling and H. Steinfink, Inorg. Chem. **5**, 1488 (1966).
- [7] H. Komoda, T. Sato, S. Souma, T. Takahashi, Y. Ito, and K. Suzuki, Phys. Rev. B **70**, 195101 (2004).
- [8] P. Villars, *Pearson's Handbook Desk Edition, Crystallographic Data for Intermetallic Phases* (ASM International, Materials Park, OH, 1997), Vol. 1, p. 1221.
- [9] A. Sacchetti, L. Degiorgi, T. Giamarchi, N. Ru, and I. R. Fisher, Phys. Rev. B **74**, 125115 (2006).
- [10] N. Ru, C. L. Condron, G. Y. Margulis, K. Y. Shin, J. Laverock, S. B. Dugdale, M. F. Toney, and I. R. Fisher, Phys. Rev. B **77**, 035114 (2008).
- [11] N. Ru, J. -H. Chu, and I. R. Fisher, Phys. Rev. B **78**, 012410 (2008).
- [12] A. Sacchetti, E. Arcangeletti, A. Perucchi, L. Baldassarre, P. Postorino, S. Lupi, N. Ru, I. R. Fisher, and L. Degiorgi, Phys. Rev. Lett. **98**, 026401 (2007).
- [13] M. Lavagnini, A. Sacchetti, C. Marini, M. Valentini, R. Sopracase, A. Perucchi, P. Postorino, S. Lupi, J. H. Chu, I. R. Fisher, and L. Degiorgi, Phys. Rev. B **79**, 075117 (2009).
- [14] S. Sllow, M. C. Aronson, B. D. Rainford, and P. Haen, Phys. Rev. Lett. **82**, 2963 (1999).
- [15] M. H. Jung, A. Alsmadi, H. C. Kim, Y. Bang, K. H. Ahn, K. Umeo, A. H. Lacerda, H. Nakotte, H. C. Ri, and T. Takabatake, Phys. Rev. B **67**, 212504 (2003).

- [16] N. D. Mathur, F. M. Grosche, S. R. Julian, I. R. Walker, D. M. Freye, R. K. W. Haselwimmer, and G. G. Lonzarich, *Nature* **394**, 39 (1998).
- [17] Y. Iyeiri, T. Okumura, C. Michioka, and K. Suzuki, *Phys. Rev. B* **67**, 144417 (2003).
- [18] C. Berthier, P. Molinié, and D. Gérôme, *Solid State Commun.* **18**, 1393 (1976).
- [19] K. Momma and F. Izumi, *VESTA: a three-dimensional visualization system for electronic and structural analysis*. *J. Appl. Crystallogr.* **41**, 653-658, (2008).
- [20] S. Blundell, *Magnetism in Condensed Matter, Oxford master series in condensed matter physics* (Oxford University Press, New York, 2001).
- [21] H. Yao, J. A. Robertson, E. A. Kim, and S. A. Kivelson, *Phys. Rev. B* **74**, 245126 (2006).
- [22] N. Ru and I. R. Fisher, *Phys. Rev. B* **73**, 033101 (2006).
- [23] B. Bireckoven and J. Wittig, *J. Phys. E* **21**, 841 (1988).
- [24] T. F. Smith, C. W. Chu, and M. B. Maple, *Cryogenics* **9**, 53 (1969).
- [25] A. Sacchetti, C. L. Condron, S. N. Gvasaliya, F. Pfuner, M. Lavagnini, M. Baldini, M. F. Toney, M. Merlini, M. Hanfland, J. Mesot, J. -H. Chu, I. R. Fisher, P. Postorino, and L. Degiorgi, *Phys. Rev. B* **79**, 201101(R) (2009).
- [26] R. J. Elliott, *Phys. Rev.* **124**, 346 (1961).
- [27] Y. Shapira and S. Foner, *Phys. Rev. B* **1**, 3083 (1970).
- [28] J. Bardeen, L. N. Cooper, and J. R. Schrieffer, *Phys. Rev.* **108**, 1175 (1957).
- [29] R. R. Hake, *Appl. Phys. Lett.* **10**, 189 (1967).
- [30] M. Núñez-Regueiro, J. M. Mignot, M. Jaime, D. Castello, and P. Monceau, *Synth. Met.* **56**, 2653 (1993).
- [31] A. F. Kusmartseva, B. Sipos, H. Berger, L. Forró, and E. Tutiš, *Phys. Rev. Lett.* **103**, 236401 (2009).
- [32] F. D. Murnaghan, *Proc. Natl. Acad. Sci. U.S.A.* **30**, 244 (1944).
- [33] P. Monceau and J. Richard, *Physica B+C* **108B**, 1237 (1981).
- [34] T. Muramatsu, N. Tateiwa, T. C. Kobayashi, K. Shimizu, K. Amaya, D. Aoki, H. Shishido, Y. Haga, and Y. Onuki, *J. Phys. Soc. Jpn.* **70**, 3362 (2001).
- [35] B. T. Matthias and J. L. Olsen, *Phys. Lett.* **13**, 202 (1964).

- [36] I. V. Berman, Zh. I. Binzarow, and P. Kurkin, Fiz. Tverd. Tela. **14**, 2527 (1972); Sov. Solid State **14**, 2192 (1973).
- [37] F. P. Bundy and K. J. Dunn, Phys. Rev. Lett. **44**, 1623 (1980).
- [38] C. Hejny, S. Falconi, L. F. Lundgaard, and M. I. McMahon , Phys. Rev. B **74**, 174119 (2006).
- [39] Y. Akahamaa, M. Kobayashia, and H. Kawamuraa, Solid State Commun. **84**, 803 (1992).
- [40] G. Bilbro and W. L. McMillan, Phys. Rev. B **14**, 1887 (1976).
- [41] G. H. Lander, J. Magn. Magn. Mater. **29**, 271 (1982).
- [42] P. G. De Gennes, Journal de Physique et Le Radium **23**, 510 (1962).
- [43] M. B. Maple, H. C. Hamaker, and L. D. Woolf, in *Superconductivity in Ternary Compounds II*, edited by Ø. Fischer and M. B. Maple (Springer-Verlag, Berlin 1982), Chap. 4.

A portion of the text and data presented in this chapter are reprints of material that appears in “High-pressure, transport, and thermodynamic properties of CeTe₃,” D. A. Zocco, J. J. Hamlin, T. A. Sayles, M. B. Maple, J. -H. Chu, and I. R. Fisher, Phys. Rev. B **79**, 134428 (2009), “Pressure-induced superconducting phase in the charge-density-wave compound terbium tritelluride,” J. J. Hamlin, D. A. Zocco, T. A. Sayles, M. B. Maple, J. -H. Chu, and I. R. Fisher, Phys. Rev. Lett. **102**, 177002 (2009), and “Superconductivity in rare-earth tritellurides,” D. A. Zocco, J. J. Hamlin, M. B. Maple, J. -H. Chu, and I. R. Fisher, *in preparation*. The dissertation author is a primary researcher and first author of the first and third articles and primary researcher and second author of the second article.

IV

Superconductivity and Magnetism in Iron-Pnictide Compounds

IV.A Introduction

A new class of superconductors consisting of layered materials with the chemical formula $LnTPnO$, where Ln is a lanthanide element, T is a transition metal, and Pn is either P or As, has recently emerged. The phosphorus-based versions of these compounds, LaFePO and LaNiPO have rather low superconducting critical temperatures, T_c of 3 K [1] and 5 K [2], respectively. Much higher T_c values were achieved by fluorine-doping the corresponding arsenic-based compound to produce $\text{LaFeAsO}_{1-x}\text{F}_x$, where doping to $x \sim 0.11$ produces $T_c = 26$ K [3]. The T_c appears to pass through a maximum as a function of fluorine doping. Subsequently, it was found that under a modest pressure of 4 GPa, the T_c of $\text{LaFeAsO}_{1-x}\text{F}_x$ increases to 43 K [4], becoming the first non-cuprate superconductor with a T_c higher than that of MgB_2 . Remarkably, it was found that replacement of the nonmagnetic La by magnetic heavier rare-earth elements also leads to high T_c values, as in $\text{SmFeAsO}_{1-x}\text{F}_x$ with the highest T_c of the series up to 55 K [5].

The T_c of optimally doped $\text{SmFeAsO}_{1-x}\text{F}_x$ initially decreases with pressure [6]. On the other hand, superconductivity (SC) has only been found to be induced by the application of external pressure in the LaFeAsO parent compound [7].

The ZrCuSiAs -type (space group $\text{P}4/\text{nmm}$) crystal structure of a “1111” iron-pnictide compound is shown in Fig. IV.1. It contains FeAs layers with Fe atoms in a square planar lattice arrangement, and these layers alternate with rare-earth/oxygen layers along the c -axis. Subsequent work led to the identification of superconductors with similar FeAs layers in the tetragonal ThCr_2Si_2 -type “122” structure (space group $\text{I}4/\text{mmm}$), with a maximum T_c of 38 K for $\text{Ba}_{0.6}\text{K}_{0.4}\text{Fe}_2\text{As}_2$ [8]. Other similar superconducting materials such as LiFeAs (“111”-type, space group $\text{P}4/\text{nmm}$) containing FeAs layers have been reported [9]. Even the binary compound $\alpha\text{-FeSe}_x$ (“11”-type, space group $\text{P}4/\text{nmm}$) was found to be a superconductor with T_c of 8 K [10]. All these classes of materials share the same layered tetragonal structure, with $\text{Fe-}Pn_4$ or $\text{Fe-}Ch_4$ ($Ch = \text{Se, Te}$) tetrahedra, separated by alkali, alkaline earth or rare earth and oxygen/fluorine blocking layers. The geometry of the tetrahedra seems to play a crucial role in determining the electronic properties of the iron-based materials. It has recently been shown that the As-Fe-As tetrahedral bond angles are intimately related to the maximum value of the superconducting transition temperature in the Fe-based superconductors, with the highest T_c values found when this angle is closest to the ideal value of 109.47° [11, 12, 13, 14, 15, 16].

The undoped “1111” parent compounds, $Ln\text{FeAsO}$, exhibit a spin density wave (SDW) and transforms from a tetragonal to an orthorhombic structure near 150 K, remaining metallic to low temperatures, and only displaying superconductivity when the SDW is suppressed towards zero temperature either through doping or pressure [7, 11]. In contrast, the phosphorus-based analogues $Ln\text{FePO}$ [1] do not manifest a SDW transition and develops, for some of the compounds, a superconducting state in the undoped form at ambient pressure. Figure IV.2 displays the evolution of T_c across the lanthanide series for $Ln\text{FeAsO}_{1-x}\text{F}_x$, $Ln\text{FeAsO}_{1-\delta}$,

and $Ln\text{FePO}$ [18]. For conventional superconductors, it is expected that T_c values are suppressed by the introduction of magnetic ions, as is observed for the well known case of de Gennes' scaling in BCS superconductors [17]. However, for the $Ln\text{FeAsO}_{1-x}\text{F}_x$ and $Ln\text{FeAsO}_{1-\delta}$ systems, T_c increases when replacing La with magnetic Ln ions. This result, together with the apparent suppression of a spin density wave that is correlated with the appearance of superconductivity, has led to the suggestion that the superconductivity exhibited by these compounds is unconventional in the sense that it is promoted by magnetic interactions [19]. In contrast, for the series $Ln\text{FePO}$, the T_c values decrease upon replacing La with Pr, Nd, or Sm, as could be expected for a conventional superconductor in the presence of magnetic pairbreaking interactions. The following Sections summarize the results of high-pressure experiments in lanthanum- and cerium-based iron-pnictide compounds performed to further probe the superconducting and magnetic properties of these interesting materials. In the first part, the results of the As-based $\text{LaFeAsO}_{0.89}\text{F}_{0.11}$, $\text{CeFeAsO}_{0.88}\text{F}_{0.12}$ and CeFeAsO polycrystals are presented. The second part describes the experiments performed in the P-based LaFePO and CeFePO single crystals. A final section is devoted to the high-pressure study of the recently synthesized single crystals of CuFeTe_2 .

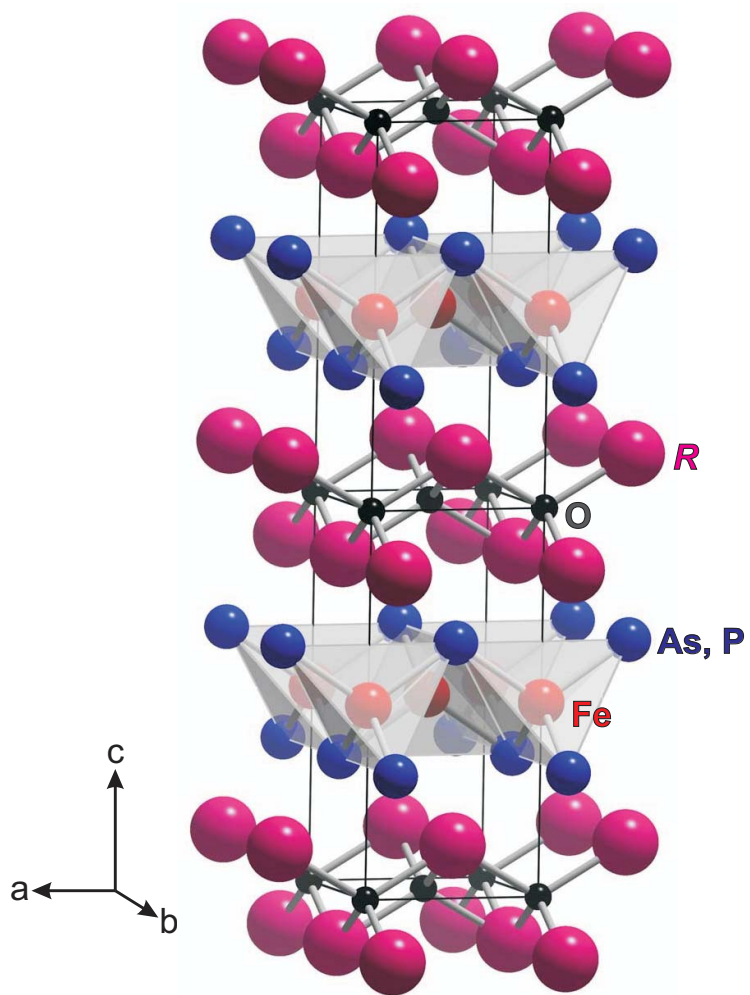


Figure IV.1: Crystal structure of $R\text{FePnO}$ (R = rare-earth atom, Pn = As, P), consisting of layers of Pn-Fe-Pn tetrahedra and alternating layers of rare-earth and oxygen. Crystal structure created with *Vesta* [20].

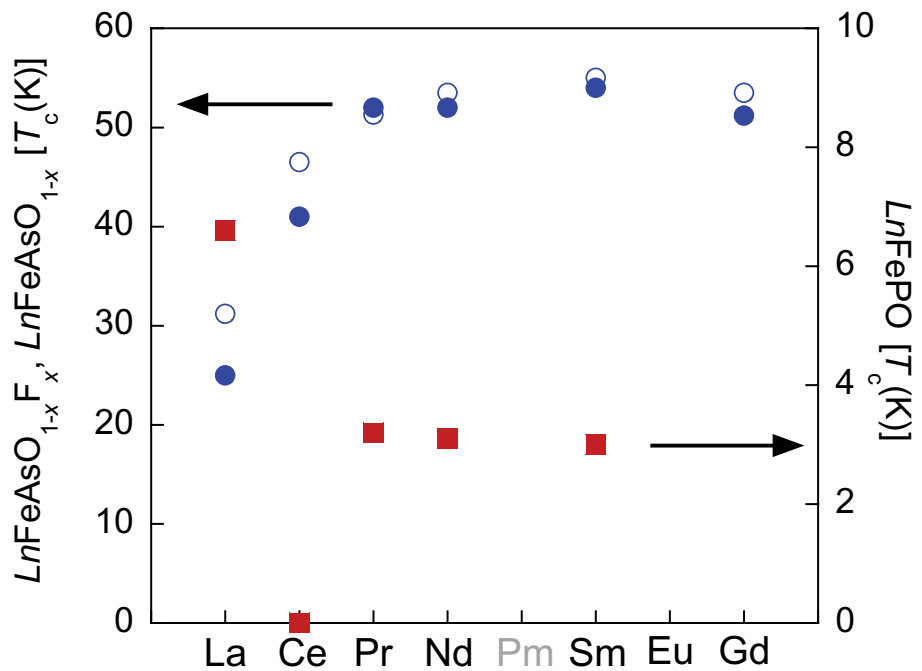


Figure IV.2: A comparison of the evolution of the superconducting transition temperature T_c versus lanthanide Ln for the series $LnFePO$ (*solid squares*), the optimally fluorine doped compounds $LnFeAsO_{1-x}F_x$ (*solid circles*), and the oxygen deficient compounds $LnFeAsO_{1-\delta}$ (*open circles*) (from Ref. [18]).

IV.B Experimental Details

Polycrystalline samples of $\text{LaFeAsO}_{0.89}\text{F}_{0.11}$ were prepared at Oak Ridge National Laboratory and taken from the same batch described in Ref. [21]. Polycrystalline samples of $\text{CeFeAsO}_{0.88}\text{F}_{0.12}$ and CeFeAsO were also prepared at Oak Ridge National Laboratory [22]. Single crystals of LaFePO and CeFePO were grown at UCSD, using the molten Sn:P flux technique described in Ref. [18].

Electrical resistivity measurements under pressure were performed employing three different techniques. In the low-pressure hydrostatic technique, pressures up to ~ 2.5 GPa were applied with a beryllium-copper, piston-cylinder clamped cell using a Teflon capsule filled with a 1:1 mixture of n-pentane:isoamyl alcohol as the pressure transmitting medium to ensure hydrostatic conditions during pressurization at room temperature. The pressure in the sample chamber was inferred from the inductively determined, pressure-dependent superconducting critical temperature of a lead or tin manometer [23, 24]. In the intermediate pressure regime, for pressures between ambient and 16 GPa, pressure was applied in a beryllium-copper Bridgman-anvil clamped cell with 4 mm diameter anvil flats, using solid steatite as the quasi-hydrostatic pressure transmitting medium. The pressure was determined from the superconducting transition of a strip of lead foil placed adjacent to the sample and measured using a 4-lead resistive method. For higher pressures, a diamond-anvil cell (DAC) technique was used. The DAC is a mechanically loaded commercial model, manufactured by Kyowa Seisakusho Ltd.. The diamond anvils are beveled from 500 to 250 μm tips. One of the diamonds contains six or eight deposited tungsten microprobes encapsulated in high-quality homoepitaxial diamond. These “designer” diamonds were obtained from a collaboration with Dr. S. T. Weir from Lawrence Livermore National Laboratory and Prof. Y. K. Vohra from University of Alabama at Birmingham. The fabrication of “designer” diamonds is described in Ref. [25]. The gasket was made from a 200 μm thick MP35N foil preindented to 40-50 μm and a 100 μm diameter hole was

drilled through the gasket using an electrical discharge machine (EDM). Several $\sim 5 \mu\text{m}$ diameter ruby spheres were loaded into the hole in the gasket and the remaining space in the hole was filled with sample, that is, no pressure transmitting medium was utilized, although in some cases solid steatite was used. Pressure was adjusted and determined at room temperature, using the fluorescence spectrum of the ruby spheres and the calibration of Chijoike *et al.* [26], with a $\delta P \leq 15\%$, inferred from the full width at half maximum (FWHM) of the fluorescence line. In some cases, more than one ruby chip was measured, allowing the estimation of pressure gradients in the sample space. Further details of the DAC technique are described in Ref. [27]. Pressure gradients for the hydrostatic ($\delta P < 2\%$) and Bridgman ($2\% < \delta P < 10\%$) cells were inferred from the width of the superconducting transition of a Sn manometer. In all cases, the electrical resistance in the *ac*-plane was measured using a 4-lead technique and a Linear Research Inc. LR-700 AC resistance bridge operating at 16 Hz. AC-susceptibility measurements in the hydrostatic cell were performed with the coil system described in Section II.C.2, using an SR-380 lock-in amplifier and an SR-554 pre-amplifier for signal detection. The experiments at high pressure were performed from room temperature to 1.2 K in a conventional ^4He bucket connected to a pumping system.

IV.C Iron-Arsenide Compounds

IV.C.1 The Superconducting $\text{LaFeAsO}_{1-x}\text{F}_x$ and $\text{CeFeAsO}_{1-x}\text{F}_x$ Compounds

Two separate high pressure-experiments on polycrystalline samples of $\text{LaFeAsO}_{0.89}\text{F}_{0.11}$ were performed. Figure IV.3 (top) shows the temperature dependence of the resistance at pressures of 0.05, 0.41 and 0.94 GPa measured in the hydrostatic clamped-cell. Upon attempting to increase the pressure beyond 0.94 GPa, the cell failed and we continued the experiment in a diamond anvil cell (DAC).

Figure IV.3 (bottom) shows the temperature dependence of the resistivity as measured in the DAC. Following the initial measurement at 6.8 GPa, pressure was increased to 17.7 GPa and then decreased to 14.5, 11.1 and 8.2 GPa. Note that the sample is in direct contact with the metallic gasket so that the measured resistance results from a combination of the sample and gasket resistivity. However, such a configuration is sufficient for locating the sharp drop in resistance when the sample becomes superconducting. The critical temperature was determined by the temperature at which the sample resistance reached 90% of the normal state value just above T_c .

Figure IV.4 illustrates the pressure dependence of T_c for $\text{LaFeAsO}_{0.89}\text{F}_{0.11}$. For comparison, the results of Takahashi *et al.* [4] and of Garbarino *et al.* [28] are plotted as blue-dashed and black-dotted lines, respectively. While T_c initially increases and then decreases beyond ~ 5 GPa, bearing some resemblance to the other experiments, the magnitude of the superconducting transition temperatures are quite different. The differing pressure dependences could be due to differences in stoichiometry or sample purity. The reported fluorine concentrations are nominal concentrations determined by the stoichiometry of the unreacted mixtures. The final concentration of fluorine in the reacted material may depend strongly on the details of the high-temperature processing such as the annealing schedule.

Two separate high-pressure experiments on polycrystalline samples of $\text{CeFeAsO}_{0.88}\text{F}_{0.12}$ were performed. At ambient pressure, the sample displays a value of T_c of 44 K in electrical resistivity. The resistive T_c value was determined by the temperature at which the resistivity drops to 90% of the normal state value just above T_c . The first high-pressure experiment was performed in a Bridgman-anvil cell up to pressures of 4.4 GPa. Above 4.4 GPa, the wires connecting to the Sn manometer broke and pressure was determined from the applied load. Previous experience with these Bridgman-anvil cells indicates that the pressure determined from the applied load is accurate to within $\pm 20\%$. Figure IV.5 shows the results of the Bridgman cell measurements on $\text{CeFeAsO}_{0.88}\text{F}_{0.12}$.

In order to verify the pressure dependence of T_c and to extend the results to higher pressure, a second experiment on $\text{CeFeAsO}_{0.88}\text{F}_{0.12}$ was carried out using a DAC. Figure IV.5 (*inset*) shows resistance versus temperature obtained from the DAC measurements. Figure IV.6 shows the T_c versus pressure for $\text{CeFeAsO}_{0.88}\text{F}_{0.12}$ obtained from the Bridgman and DAC experiments. At the lowest measured pressures it was found that the values of T_c were near 47 K, somewhat higher than the $T_c = 44$ K measured at ambient pressure. This small increase in the critical temperature is likely due to improvement in sample connectivity due to grain compaction under pressure, rather than the intrinsic pressure dependence of T_c . The T_c value decreases monotonically with pressure and is suppressed below 1.1 K at 26.5 GPa.

The strong dependence of T_c on pressure in these materials is rather remarkable. Shein *et al.* [29] calculate that the bulk modulus of LaFeAsO is only 98 GPa, significantly smaller than that found for the cuprate superconductors. It is likely that the strong dependence of T_c on pressure for $\text{LaFeAsO}_{0.89}\text{F}_{0.11}$ and $\text{CeFeAsO}_{0.88}\text{F}_{0.12}$ is related to their high compressibility. Experiments to determine structural parameters under pressure would help to clarify the effect of lattice properties on T_c .

For the iron-pnictides it is likely that, as in the cuprates, increasing pressure leads to an increase in carrier concentration. The initial increase in T_c with pressure for $\text{LaFeAsO}_{0.89}\text{F}_{0.11}$ may thus be due to the sample being underdoped. Indeed, Lu *et al.* [30] find that increased doping achieved through high-pressure synthesis raises T_c to 41 K in $\text{LaFeAsO}_{0.89}\text{F}_{0.11}$. In the high- T_c cuprate superconductors, it is found that T_c generally increases with pressure in optimally doped samples, highlighting the fact that the effect of pressure is more complicated than simply changing the carrier concentration [31]. The negative pressure dependence of T_c that is found for apparently optimally doped $\text{CeFeAsO}_{0.88}\text{F}_{0.12}$ combined with that previously reported for $\text{SmFeAsO}_{1-x}\text{F}_x$ [6] points to a possible difference between the iron-pnictides and cuprate superconductors. A systematic study of the

effect of pressure on T_c across a wide range of dopings is clearly needed in order to obtain a better understanding of the optimal conditions for high- T_c values in the iron-pnictide superconductors.

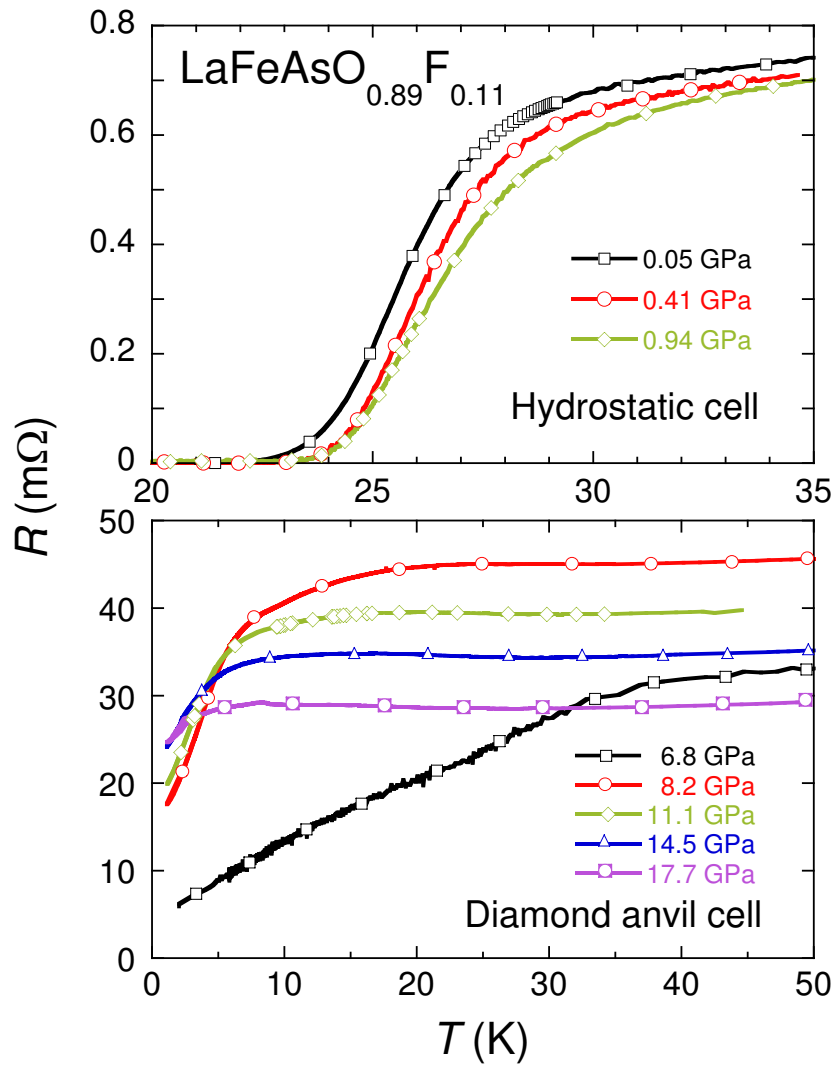


Figure IV.3: Electrical resistance R vs. temperature T of $\text{LaFeAsO}_{0.89}\text{F}_{0.11}$ for different applied pressures. *Upper panel*: curves corresponding to the hydrostatic clamped-cell technique. *Lower panel*: diamond-anvil cell experiment.

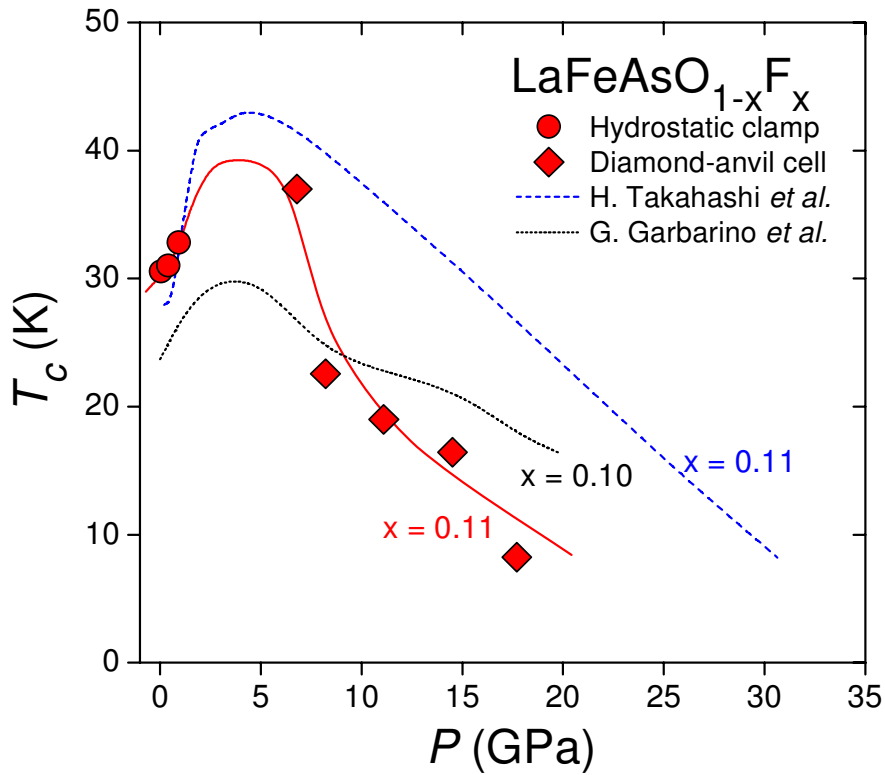


Figure IV.4: Superconducting transition temperature T_c vs. pressure P of $\text{LaFeAsO}_{1-x}\text{F}_x$. Red circles correspond to measurements in the hydrostatic cell, and red diamonds correspond to the diamond-anvil cell experiment, both for a sample containing $\sim 11\%$ of fluorine. The solid red line is a guide to the eye. The black dashed curve represents the data previously published by Takahashi *et al.* for a sample containing $\sim 11\%$ of F [4]. The black dashed curve represents the data previously published by Garbarino *et al.* for a sample containing $\sim 10\%$ of F [28].

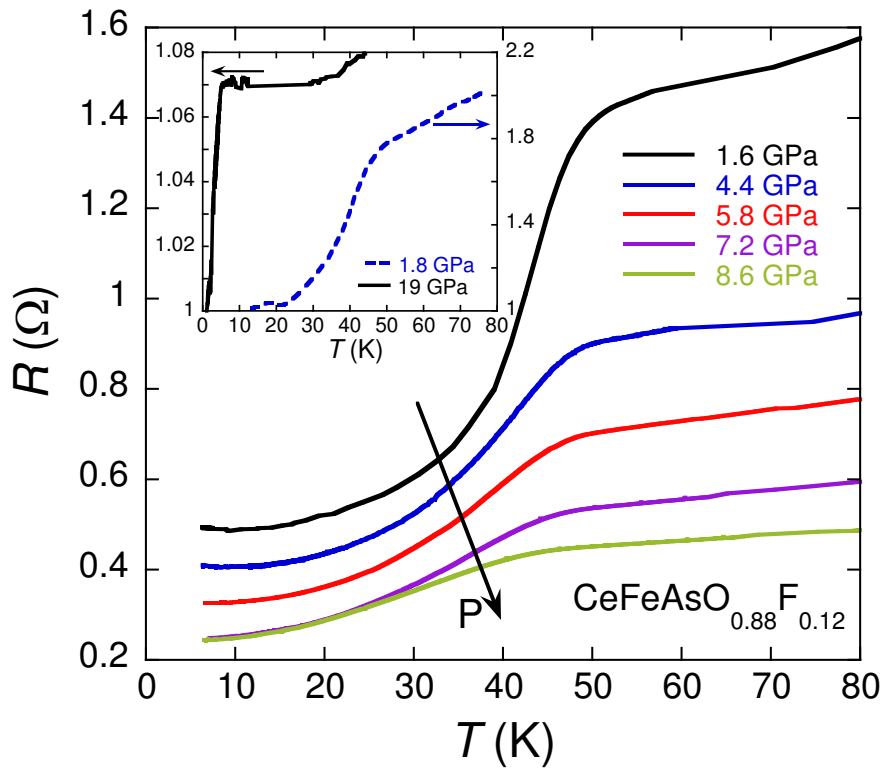


Figure IV.5: Temperature dependence of the electrical resistance R of $\text{CeFeAsO}_{0.88}\text{F}_{0.12}$ for different applied pressures up to 8.6 GPa using the Bridgman-anvil cell technique. The superconducting T_c is defined as the temperature at which the sample resistance reaches 90% of the normal state value. *Inset:* diamond anvil cell resistance curves for 1.8 and 19 GPa, normalized to their respective base temperature values.

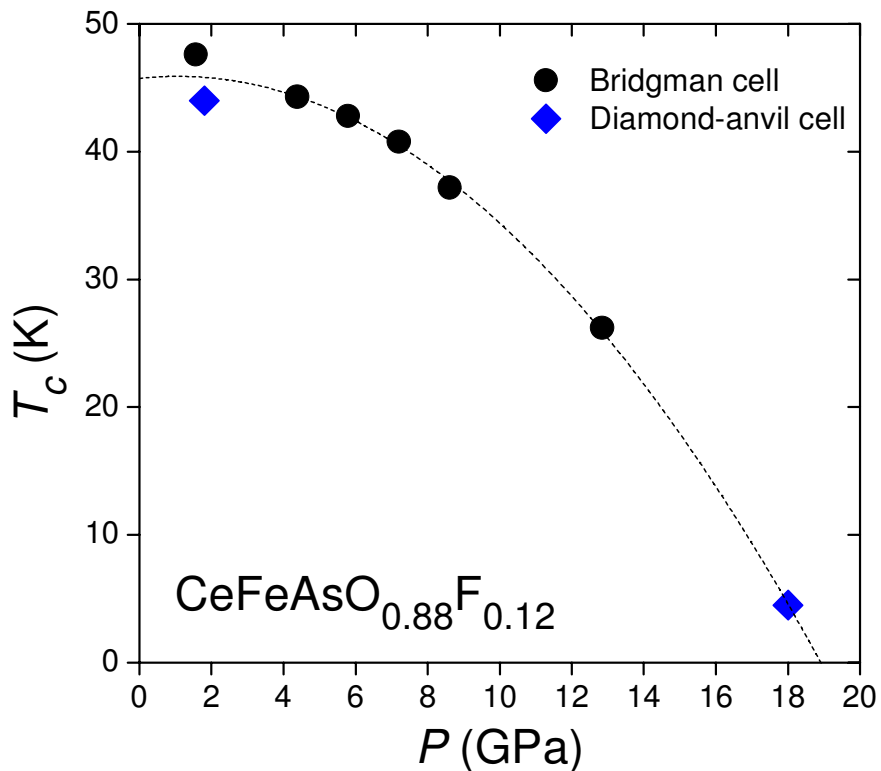


Figure IV.6: Superconducting T_c versus pressure P of $\text{CeFeAsO}_{0.88}\text{F}_{0.12}$. The dashed curve is a guide to the eye given by a quadratic fit of the data, extrapolating to zero temperature at ~ 19 GPa.

IV.C.2 Search for Pressure Induced Superconductivity in Undoped CeFeAsO

The compound CeFeAsO is a semimetal, with coexisting Fe-3d and Ce-4f antiferromagnetic (AFM) phases below 4 K, and becomes a superconductor below 41 K when 16% of oxygen is substituted by fluorine [32]. It was found that CeFeAsO undergoes a lattice distortion from a tetragonal to an orthorhombic structure near 155 K, followed by the formation of a commensurate spin density wave (SDW) on the Fe sublattice below 140 K [12], although it has been recently found that the temperature difference between the structural and the magnetic transitions of CeFeAsO is strongly sample dependent [33].

The experiments reported herein were carried out, in part, to address whether the Ce ion valences in CeFeAsO are sensitive enough to pressure to increase the electron concentration of the Fe-As layers by driving Ce from the 3+ towards the 4+ valence state. For CeFeAsO, this could have the effect of decreasing the fraction of the Fermi surface (FS) gapped by the long-range Fe magnetism, resulting in a dependence of the transition temperatures on pressure similar to that observed for F substitution.

The electrical resistivity of polycrystalline CeFeAsO as a function of temperature, obtained in the hydrostatic cell experiment, is plotted in Fig. IV.7. Two main features are identified: the peak-like feature centered at $T^* \sim 150$ K, which was previously identified as the onset to SDW order of the Fe electronic spins, and the kink at $T_{N,Ce} \sim 4$ K, attributed to the antiferromagnetism of the localized spin states of the Ce atoms [32]. In these experiments, T^* is defined as the mid-point temperature in the derivatives $d\rho(T)/dT$, indicated with the vertical arrows in Fig. IV.7c. For measurements using the hydrostatic clamp (Fig. IV.7a), T^* decreases with applied pressure at a rate of -9 K/GPa, which is similar to the value obtained for LaFeAsO [7]. On the other hand, $T_{N,Ce}$ increases at a rate of $+0.9$ K/GPa, as shown in detail in Fig. IV.7b. These results suggest that, with increasing pressure, more Fe *d*-electrons participate in the indirect interaction between

the magnetic Ce ions. The increase of $T_{N,Ce}$ with pressure can be qualitatively explained in both an SDW and a local moment picture for the AFM ordering of the Ce ions. In the SDW picture, the decrease with pressure of the FS fraction that is gapped by the Fe SDW results in an increase of the FS fraction that is available to be gapped by the Ce AFM state, thereby increasing $T_{N,Ce}$ with pressure. In the local moment picture, the increase of the FS fraction that remains “ungapped” by the Fe SDW results in an increase of the density of states at the Fermi level, $N(E_F)$. In addition, the increase of pressure results in an increase in the magnitude of the exchange interaction parameter $|J|$, which is well documented for the case of Ce ions in dilute alloys (*e.g.*, $\text{La}_{1-x}\text{Ce}_x$) or compounds (*e.g.*, SmS) [34, 35]. The increase of $|J|$ with pressure results from the increase of hybridization which can be visualized within the context of the Friedel-Anderson model through the Schrieffer-Wolff transformation $J \sim -\frac{\langle V_{fc}^2 \rangle}{\varepsilon_f}$, where $\langle V_{fc} \rangle$ is the matrix element that admixes the Ce 4f-electron states and the conduction electron states, $\varepsilon_f = E_F - E_f$ is the *f*-electron binding energy, and E_f is the centroid of the *f*-state, where the width Δ of the localized state is $\Delta \sim \pi N(E_F) \langle V_{fc}^2 \rangle$ (see Section I.A.3). A more complete picture, which includes the orbital angular momentum is given by the Coqblin-Schrieffer transformation (see, for example, Ref. [35]). This situation should also produce Kondo lattice physics in which a nonmagnetic ground state forms below the Kondo temperature $T_K \sim T_F \exp(-1/N(E_F)|J|)$, where T_F is the Fermi temperature. Since the Néel temperature T_N is expected to vary as $T_N \sim |N(E_F)J|^2$, the existence of AFM ordering and the increase of $T_{N,Ce}$ with pressure indicates that $T_N > T_K$ (see Fig. I.1 [36]).

Recently [37], LDA+DMFT calculations showed that, for CeFeAsO, the hybridization potential V_{fc} increases substantially with pressure, which is reflected as an exponential increase of T_K , from 10^{-4} K at ambient pressure, to 100 K at 15 GPa. A rough comparison of the rate of suppression of T^* with that observed when oxygen is replaced by fluorine in the same compound [32] with the subsequent appearance of superconductivity, motivated the additional measurements done on

CeFeAsO in the higher pressure region. The Bridgman-anvil cell results are shown in Fig. IV.8a, for $2.5 \text{ GPa} \leq P \leq 14.5 \text{ GPa}$. At the lowest pressure, the feature corresponding to T^* appears in the vicinity of 150 K, and then broadens at higher pressures. At 4.5 GPa, this feature is no longer distinguishable, as can also be seen in the very flat derivative curve in Fig. IV.8c. At higher pressures, the broad feature re-emerges and persists up to 14.5 GPa, although its association with the SDW can no longer be verified. An opposite trend is observed for the antiferromagnetic ordering of the Ce moments (Fig. IV.8b). $T_{N,Ce}$ increases from 6 K to a maximum value of 8 K at the same rate as in the hydrostatic cell experiments, and at 4.5 GPa, $T_{N,Ce}$ begins to decrease and reaches 5 K at 14.5 GPa. The hydrostatic cell and Bridgman-anvil cell results are summarized in the T - P phase diagram of Fig. IV.9. Since the values of T^* at 2.5 GPa do not match for the hydrostatic and Bridgman-anvil techniques, presumably due to sample dependence or larger strains in the Bridgman cell technique, but the slopes dT^*/dP are similar, the Bridgman-anvil experiment values of T^* are plotted offset down to match the last point obtained in the hydrostatic experiment, in order to facilitate comparison. The shaded area in Fig. IV.9a indicates the pressure region in which T^* is more difficult to identify from the measurements.

Fig. IV.8d shows the diamond-anvil cell (DAC) electrical resistivity vs. temperature for CeFeAsO for $1 \text{ GPa} \leq P \leq 50 \text{ GPa}$ (curves were normalized to the corresponding values at 270 K). At the lowest pressure (1 GPa), both the Fe-SDW and the Ce-AFM features were observed. At higher pressures, the Fe-SDW shoulder smeared out, and even the sharper Ce-AFM transition disappeared and was replaced by minima and upturns at the highest pressures (see Fig. IV.8e).

It is worth emphasizing the lack of pressure induced superconductivity (SC) in the CeFeAsO samples. So far, SC in an undoped “1111” iron arsenide was reported exclusively in LaFeAsO [7], where only one electrical resistivity curve dropped completely to zero below T_c . Also, in that work, a 1:1 mixture of Fluorinert FC70/77 was utilized as the pressure transmitting medium which is known

to be non-hydrostatic above 0.8 GPa [38]. A detailed discussion of the effects of non-hydrostatic pressure media in the “1111” and “122” Fe-pnictide families was recently reported by W. Bi *et al.* [39]. If we assume that the pressure induced SC in polycrystalline LaFeAsO is unrelated to oxygen deficiency, we might then speculate that the appearance of SC could be related to significant strain which can develop even in hydrostatic media, due to the anisotropic compressibility of adjacent randomly oriented grains. In polycrystalline CeFeAsO, however, SC did not appear despite the very non-hydrostatic conditions obtained in the diamond anvil cell, although the response to strain may be opposite for the 122 materials compared to the 1111 materials. It would be interesting to see if pressure induced SC could appear under nearly strain free conditions where single crystalline Ln FeAsO samples were compressed under hydrostatic conditions.

It was noted before that in the iron-pnictide compounds, the shape of the $FePn_4$ tetrahedra is highly correlated with the maximum T_c achieved [11, 12, 13, 14, 15, 16]. Theoretical work has shown that the Fermi surface topology is very sensitive to the $Fe-Pn$ bond length as well as the deviation of Pn - Fe - Pn angle from the value of 109.47° corresponding to a regular tetrahedron, mainly due to the rather high degree of covalency of the $Fe-Pn$ bond [40, 41, 42]. A comparison between the pressure and the doping dependences of the Pn - Fe - Pn angle of LaFeAsO and CeFeAsO would, perhaps, help us to understand the appearance of the superconducting state in these materials.

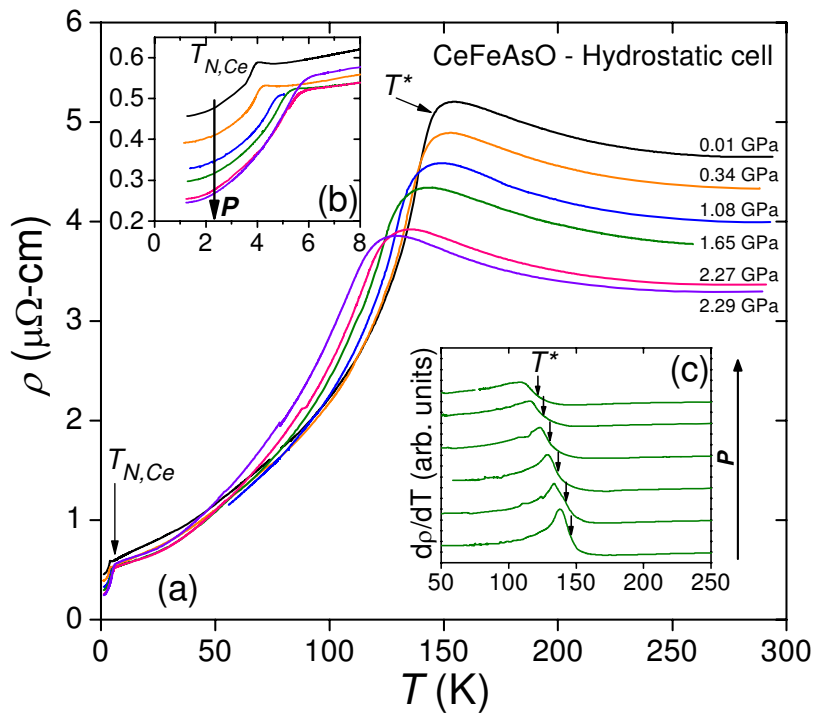


Figure IV.7: (a) Electrical resistivity ρ versus temperature T at various pressures P for CeFeAsO polycrystalline samples, obtained in the hydrostatic clamped cell experiment. (b) Evolution of $T_{N,Ce}$ at low temperatures. (c) $d\rho/dT$ vs. T curves for the hydrostatic experiment. The arrows indicate the position of T^* .

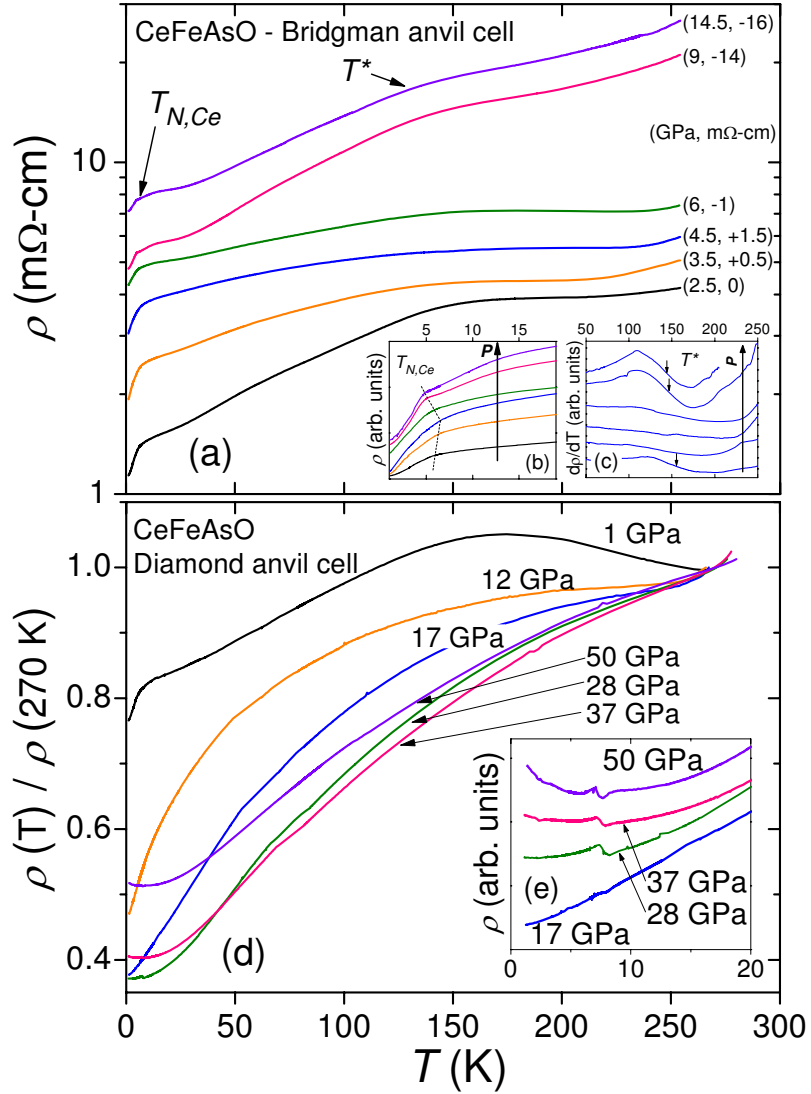


Figure IV.8: (a) Electrical resistivity ρ versus temperature T at various pressures P for CeFeAsO polycrystalline samples for the Bridgman-anvil cell experiment. The curves are shifted for clarity. The pressure and magnitude of the offset are indicated in parentheses at the right of the curves. (b) Low temperature detail, showing the evolution of $T_{N,Ce}$ at various pressures. (c) $d\rho/dT$ vs. T curves for the Bridgman-anvil cell experiment. (d) Diamond-anvil cell resistivity curves normalized to 270 K. (e) Low temperature detail for the higher pressures.

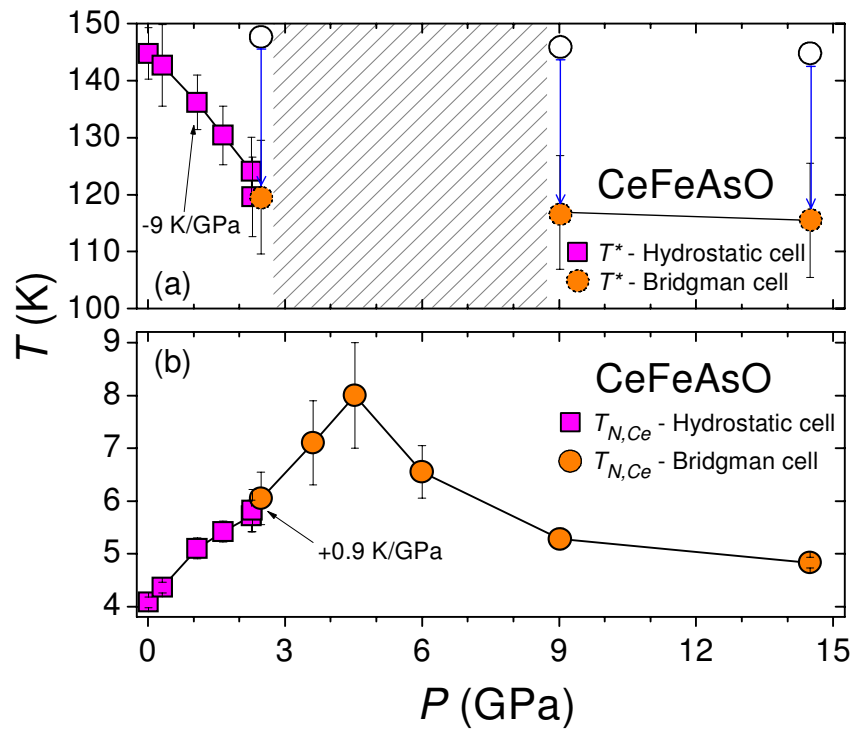


Figure IV.9: T - P phase diagram for CeFeAsO. In (a), data corresponding to the Bridgman-anvil technique are shown shifted to match the hydrostatic cell measurements. In the *upper panel*, the shaded region indicates the pressure range where the value of T^* is more difficult to determine from the measurements.

IV.D Iron-Phosphorous Compounds

IV.D.1 Superconductivity in Single Crystals of LaFePO

The electrical resistivity measurements of a single crystal of LaFePO are shown in Fig. IV.10, revealing metallic behavior, where $\rho(T)$ smoothly decreases with decreasing T until it drops abruptly to zero at the superconducting transition temperature $T_c = 6.6$ K. This transition temperature is defined as the temperature where $\rho(T)$ drops to 50% of its extrapolated normal state value. The transition width $\Delta T_c = 1.3$ K is taken as the difference in the temperatures where $\rho(T)$ drops to 10% and 90% of the extrapolated normal state value. For $\sim 100\text{-}300$ K, $\rho(T)$ has an approximately linear T dependence which evolves into a quadratic form for $\sim 10\text{-}100$ K, as shown in the left *inset* to Fig. IV.10. Fits over this temperature range show that the data are well described by the expression $\rho(T) = \rho_0 + AT^2$, where $\rho_0 \sim 14 \mu\Omega\text{cm}$, and $A = 9.46 \times 10^{-3} \mu\Omega\text{cm}/\text{K}^2$. The residual resistivity ratio $RRR = \rho(300\text{K})/\rho(0) = 32$ reflects the high quality of the LaFePO single crystal. Also shown in Fig. IV.10 are results for a platelet which was reduced at 700 °C in flowing Ar for 24 hours. For this specimen, $RRR = 58$, $T_c = 7.8$ K, and the $\Delta T_c = 1.6$ K, indicating that the superconducting state may be enhanced by reduction of oxygen concentration. Fits to the data for the reduced sample give $\rho_0 \sim 16.7 \mu\Omega\text{cm}$ and $A = 2.44 \times 10^{-2} \mu\Omega\text{cm}/\text{K}^2$.

Electrical resistivity $\rho(T)$ measurements were made under high pressures of 5.4, 10.6, 15.8, and 20.4 GPa in the diamond-anvil cell, as shown in Figs. IV.11 and IV.12. Fig. IV.11 displays the results in the whole temperature range, for two different configurations of the six tungsten leads of the designer diamond. Each different configuration measures a somewhat different section of the sample. The effect of pressure is first to lower the overall resistivity of the sample. At 20.4 GPa, however, the electrical resistivity becomes higher, although this might be due to the fact that the thickness of the sample has reduced considerably with the pressure, giving a higher resistance. At low temperatures, the sharp drop in the

resistivity indicates the onset of superconductivity. The curves do not reach zero resistance, and this is somehow expected at very high pressures obtained in an anvil technique, since very large pressure gradients develop along the sample, broadening the features observed in the experiments. The upper panels in Fig. IV.12 display the resistance versus pressure in the vicinity of the superconducting transition, normalized to the 15 K resistance. The values of T_c shown in the lower panel were determined graphically as illustrated by the dashed lines in the upper panels and averaged over the two configurations of leads. The values for the vertical bars represent the superconducting onset temperature and were determined by the temperature at which the resistivity passes through a maximum. The pressure was determined from an average of the pressure given by the two different pieces of ruby in the cell and the horizontal bars represent the pressure difference was determined from each individual piece of ruby. The point at ambient pressure was taken from the resistivity curve shown in Fig. IV.10. Remarkably, a rather moderate pressure of 10.6 GPa is sufficient to nearly double the onset of superconductivity from ~ 7 K to ~ 14 K, above which pressure acts to suppress T_c .

Plotted in Fig. IV.12 along with our data, are the results from three different experiment recently reported by Igawa *et al.* [43]. The open circles were obtained from electrical resistivity measured in a hydrostatic cell experiment, using a 1:1 mixture of Fluorinert 70/77 as pressure transmitting medium. The open triangles were obtained from electrical resistivity in a diamond-anvil cell (DAC) loaded with NaCl as pressure medium, and the open-star symbols were obtained from measurements of magnetization in a DAC, where a methanol-ethanol mixture in a 4:1 ratio was utilized as pressure medium. These experiments show that T_c initially rises steeply at very low pressures, and reaches a maximum of 8.8 K at 0.8 GPa, and decreases slowly at higher pressures. These values of T_c differ somehow from our results, although the overall behavior seems rather similar.

It is interesting to note that, in all these experiments, the values of T_c raise during initial pressurization. An important question to ask would be what are

the effects of different pressure media on the evolution of T_c . Shear stresses, developed at high pressures in the medium, may strongly influence the properties of the samples. The measurements performed in the DAC with no pressure medium are highly non-hydrostatic. Similarly, a 1:1 mixture of FC 70/77 is known to remain hydrostatic up to 0.8 GPa [38]. We performed ac-susceptibility measurements at high pressures in the hydrostatic clamped-cell, using FC70 as pressure medium, which remains hydrostatic up to only 0.4 GPa. Figure IV.13 shows the results of our data, along with the low-pressure data of Igawa *et al.* described before. In addition, the ac-susceptibility data obtained by Schilling *et al.* [44] using a He gas system are plotted as grey diamonds. Surprisingly, the values of T_c obtained using the FC70 medium decrease monotonically up to ~ 1 GPa, with no appreciable change around 0.4 GPa, where FC70 is no longer hydrostatic. This result is very different from the one shown in Igawa's paper, although it is in strong agreement with the results obtained in the best hydrostatic conditions attained in the He gas system. Since the single crystals measured in the He gas system were grown in our laboratory as the ones we used in our experiment, one could conclude that the behavior of T_c under applied pressure is governed by the intrinsic properties of the samples, such as doping, and not by the condition in which the pressure experiments were performed. More high pressure experiments will soon be performed in order to elucidate this issue.

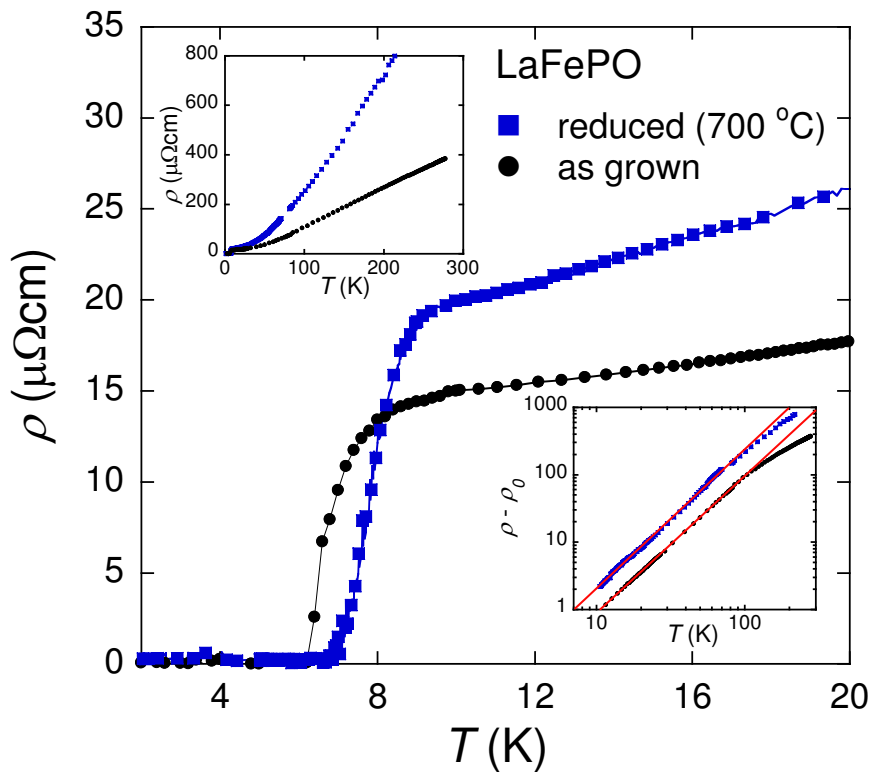


Figure IV.10: Electrical resistivity ρ versus temperature T of a LaFePO single crystal measured in the ab -plane for an as-grown single crystal and a crystal that was reduced in flowing argon at 700 °C for ~ 12 hours. *Left inset:* Resistivity over the entire measured temperature range showing T^2 behavior for ~ 10 -100 K and linear T behavior for ~ 100 -300 K. *Right inset:* Log-log plot of $\rho - \rho_0$ versus T . The solid red lines are fits to the data which demonstrate the T^2 behavior for 10-100 K for the as grown sample and 10-80 K for the reduced sample.

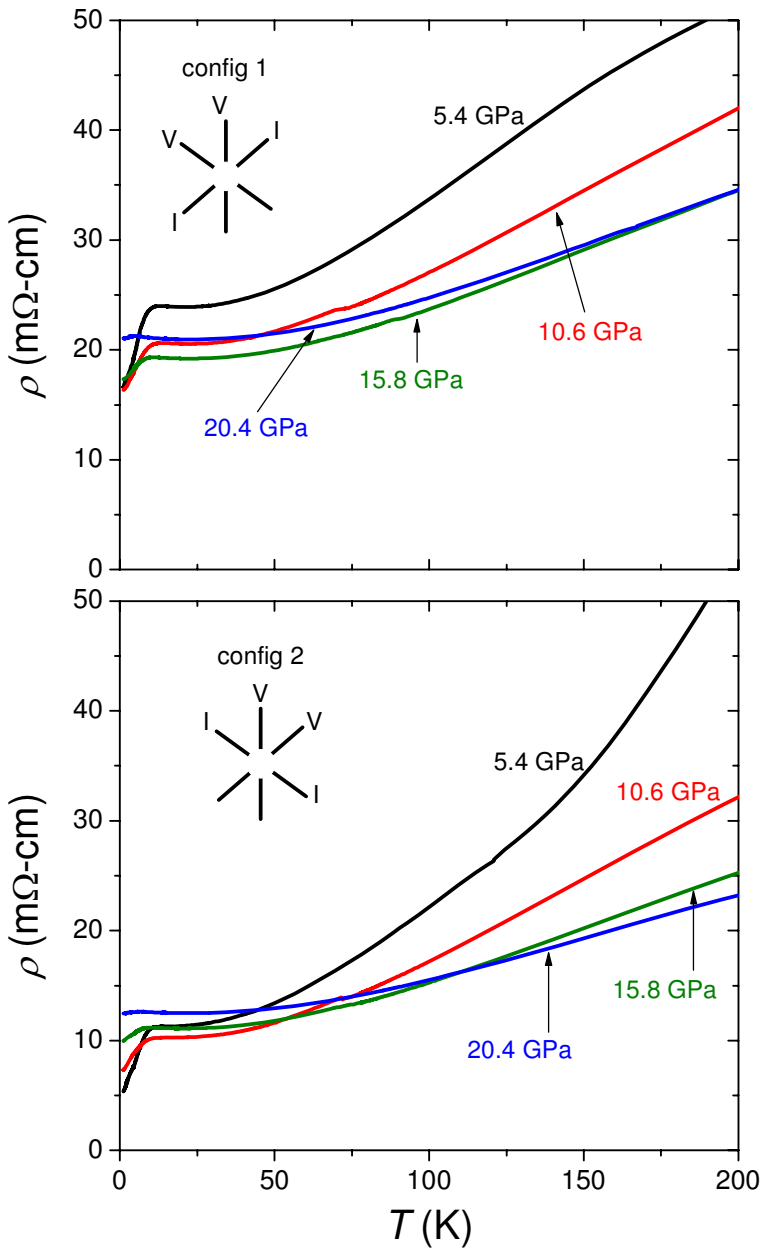


Figure IV.11: Electrical resistivity ρ versus temperature T of a LaFePO single crystal measured in the diamond-anvil cell. The top and bottom panels display the data obtained from two different contact configurations of the six-lead designer diamond.

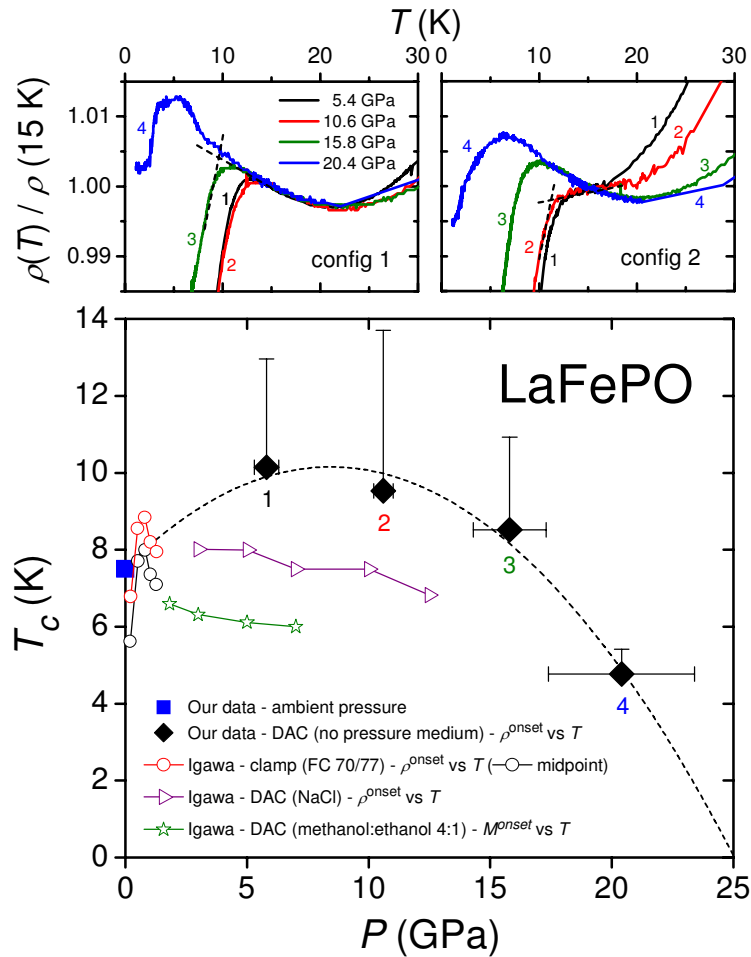


Figure IV.12: *Top panels:* Electrical resistance normalized to the values at 15 K for two different lead configurations. The onset T_c is defined as the intersection of the dashed lines. Numbers indicate the order in which the pressures were applied. *Main panel:* Pressure dependence of the onset T_c . The value of the T_c at ambient pressure corresponds to the measurement of R versus T shown in Fig. IV.10, while the high-pressure points correspond to the DAC measurements. The high temperature limit of the vertical bars correspond to the temperature at which $\rho(T)$ deviates from the normal state behavior. Data from three different experiments performed by Igawa *et al.* are also shown for comparison [43].

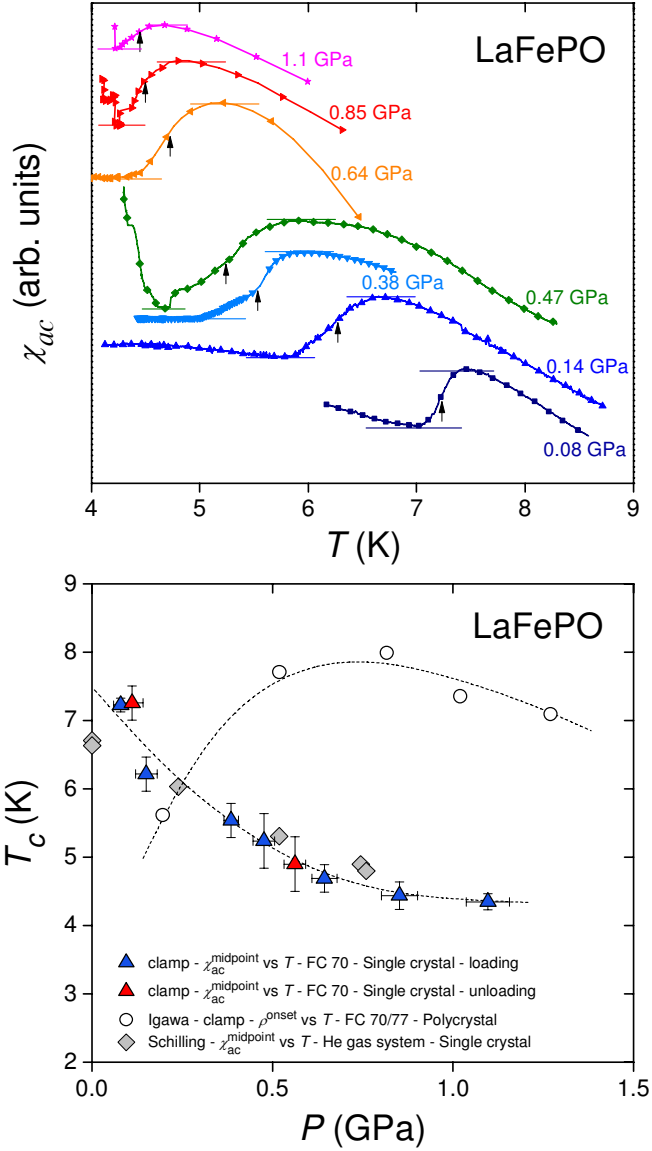


Figure IV.13: *Top panel:* AC-magnetic susceptibility of LaFePO at various increasing pressures, indicated beside each measurement. The values of T_c are indicated by the arrows, and correspond to the voltage value at the midpoint of the maximum and minimum voltages observed at the superconducting transition. *Bottom panel:* Low-pressure evolution of the T_c of LaFePO from the ac-susceptibility experiments (*blue and red triangles*). The open circles and filled diamonds correspond to previous data by Igawa *et al.* [43] and Schilling *et al.* [44].

IV.D.2 High Pressure Stabilization of the Kondo Lattice behavior in CeFePO Single Crystals

CeFePO is a heavy fermion metal ($\gamma \sim 700 \text{ mJ/molK}^2$) with no magnetic order found to date [45]. Recently [46, 47], the isoelectronic substitution of As by P has revealed a rich phase diagram, in which an antiferromagnetic (AFM) and a ferromagnetic (FM) quantum critical point (QCP) are found at intermediate compositions.

Fig. IV.14 shows the electrical resistivity $\rho(T)$ for a single crystalline CeFePO sample for different pressures applied in the hydrostatic piston-cylinder clamp (ambient $\leq P \leq 2.7 \text{ GPa}$). The resistivity exhibits a typical Kondo lattice behavior throughout the entire pressure range, *i.e.*, $\rho(T)$ decreases weakly at high temperatures and drops strongly below T_{coh} , the Kondo-coherence temperature. It is well known that for Ce compounds, pressure increases the value of the hybridization matrix element V_{fc} between $4f$ - and conduction electrons [48], causing an increase of T_{coh} . In the CeFePO case, as pressure increases, T_{coh} shifts towards higher temperatures, with an initial slope of $+14 \text{ K/GPa}$, and at a much higher rate of $+43 \text{ K/GPa}$ above 1 GPa (Fig. IV.15).

A broad feature develops below 30 K, which is apparent at 2.68 GPa, as can be seen in the *inset* of Fig. IV.14. In order to further study this low temperature feature, a series of magnetization M and specific heat C experiments were performed for both unannealed and annealed samples. M vs. T and M vs. H measurements were performed from 2 K to 300 K in a commercial Quantum Design MPMS in fields up to 7 T. C vs. T measurements were made from 2 K to 300 K in a Quantum Design PPMS semiadiabatic calorimeter using a heat-pulse technique and a small amount of Apiezon N grease to attach the specimens to a sapphire platform, in magnetic fields H up to 9 T. In all cases we used an array of approximately 30 crystals for a total mass of $\lesssim 500 \text{ mg}$. The annealed samples were obtained by heating the single crystals at 700°C in flowing O_2 over a period of 24 hours. For as-grown samples, M vs. T curves showed paramagnetic behavior over

the entire temperature range for crystals arranged with the c -axis perpendicular and parallel to the applied magnetic field, and no order was detected down to 2 K. Curie-Weiss fits in the $4 \text{ K} \leq T \leq 160 \text{ K}$ range gave an effective magnetic moment of $2.41 \mu_B$, which is close to the expected for Ce^{3+} free ions.

Fig. IV.16 and Fig. IV.17a display the results of the zero-field-cooled and field-cooled magnetization experiments of the annealed single crystals, for magnetic fields applied perpendicular and parallel to the c -axis of the crystals. Clearly, CeFePO presents anisotropic magnetic properties, with larger susceptibility in the ab -planes. The magnetization depart from paramagnetic behavior below 10 K for magnetic fields applied perpendicular to the c -axis, as can be seen in more detail in the upper panel of Fig. IV.17. A broad feature below 3 K was also seen in the specific heat measurements performed in both unannealed and annealed samples (Fig. IV.17b, for the annealed crystals), for which the size of the jump is approximately 500 mJ/molK^2 . For comparison, the data of previous specific heat measurements performed by Brüning *et al.* [45] are included in Fig. IV.17b. In that case, the curve does not show any indication of magnetic order down to 1 K. The *inset* of Fig. IV.16, displays the M vs. H measurements at 2 and 30 K. For $H \perp c$, the magnetization measured at 2 K shows paramagnetic behavior with fields up to $\sim 5 \text{ T}$. Above 5 T, the magnetization curves down, characteristic of a system that undergoes magnetic order.

The results presented above suggest that CeFePO might be entering a magnetic phase at low temperatures, although we cannot rule out other origins. It is possible that these features are related to the ones observed at low temperature in the electrical resistivity under pressure experiments. For example, in a recent study on CeRhSn [49], a similar feature near 6 K in the $\rho(T)$ data and a small jump in C/T were also observed. These features were attributed to non-Fermi liquid (NFL) behavior in the proximity to a QCP and were explained as possibly originating from inhomogeneous magnetic ordering of the spin-glass-type, promoted by atomic disorder. In that paper, the authors also showed that the

size of the jump in C/T at 6 K depends on annealing time, varying from 60 to 350 mJ/molK², comparable to the value obtained in our experiments. Further experiments are currently being carried out in order to elucidate this matter.

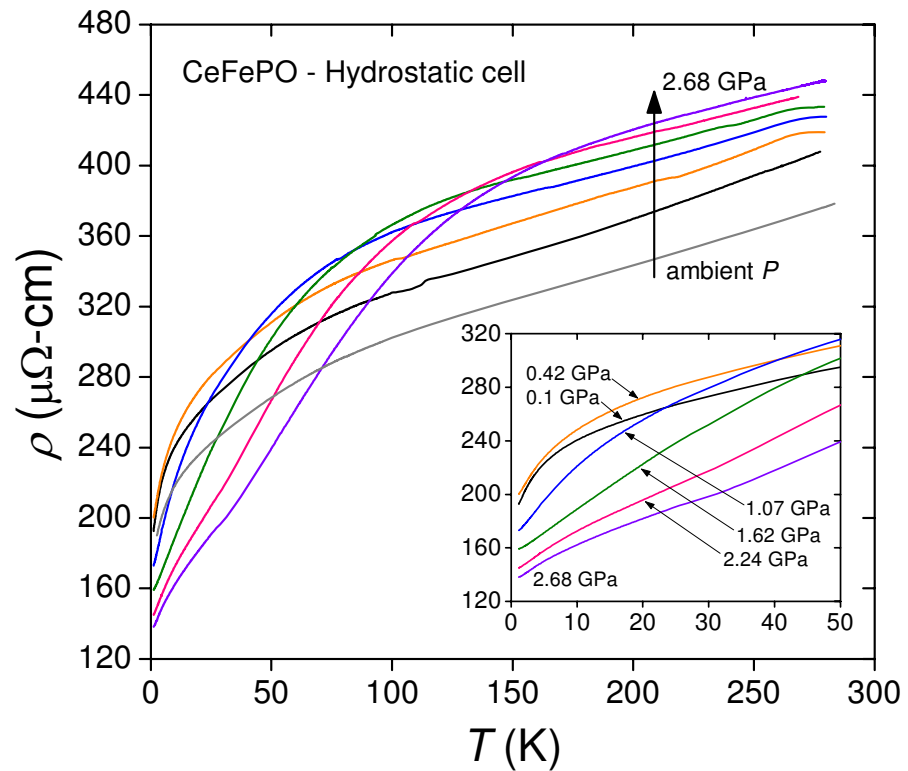


Figure IV.14: Electrical resistivity ρ versus temperature T of CeFePO single crystals at pressures P of 0.01, 0.10, 0.42, 1.07, 1.62, 2.24 and 2.68 GPa, obtained with the hydrostatic clamped cell technique. *Inset:* low temperature region.

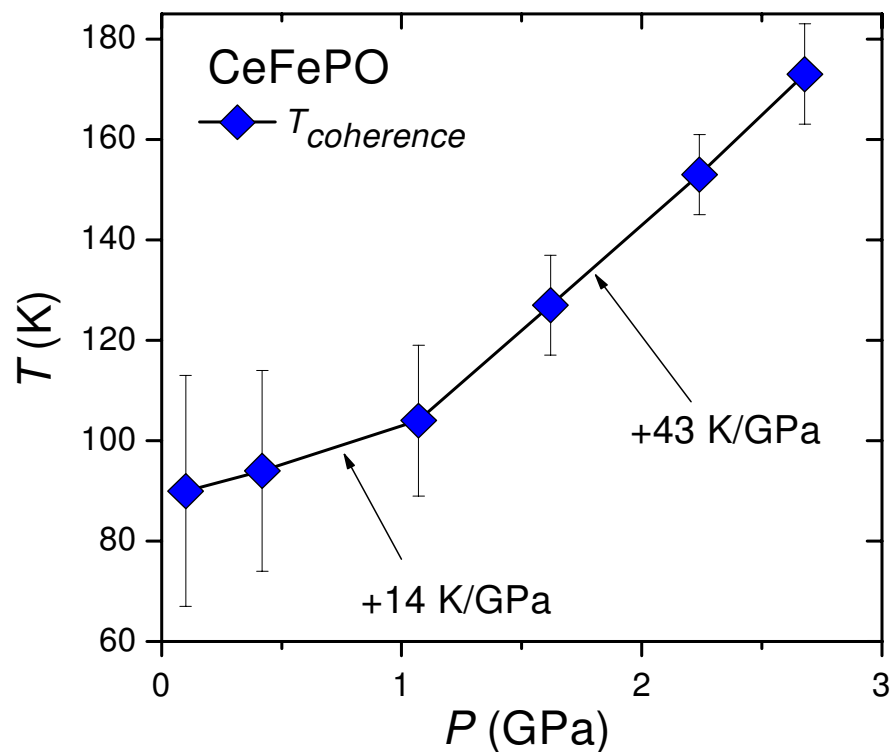


Figure IV.15: Evolution of the coherence temeperature of CeFePO as a function of pressure.

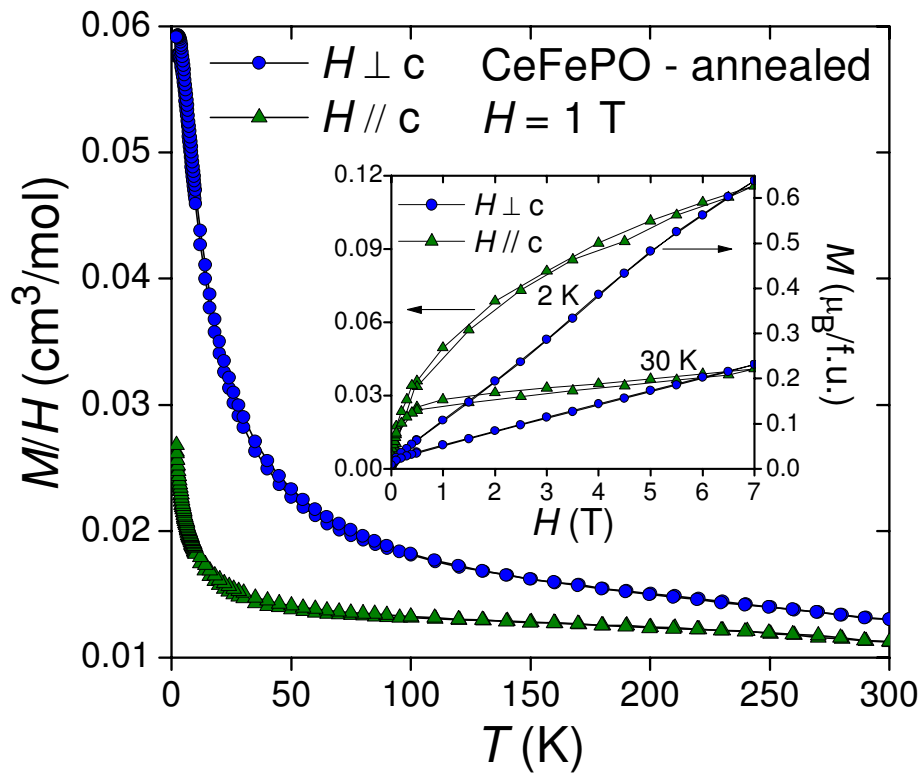


Figure IV.16: Magnetization M divided by applied magnetic field H versus temperature T of CeFePO. Fields of 1 T were applied perpendicular to the c -axis (blue circles) and parallel to the c -axis (green triangles). The *inset* displays the $M - H$ measurements performed at 2 K and at 30 K, also for H applied perpendicular and parallel to the c -axis of the samples.

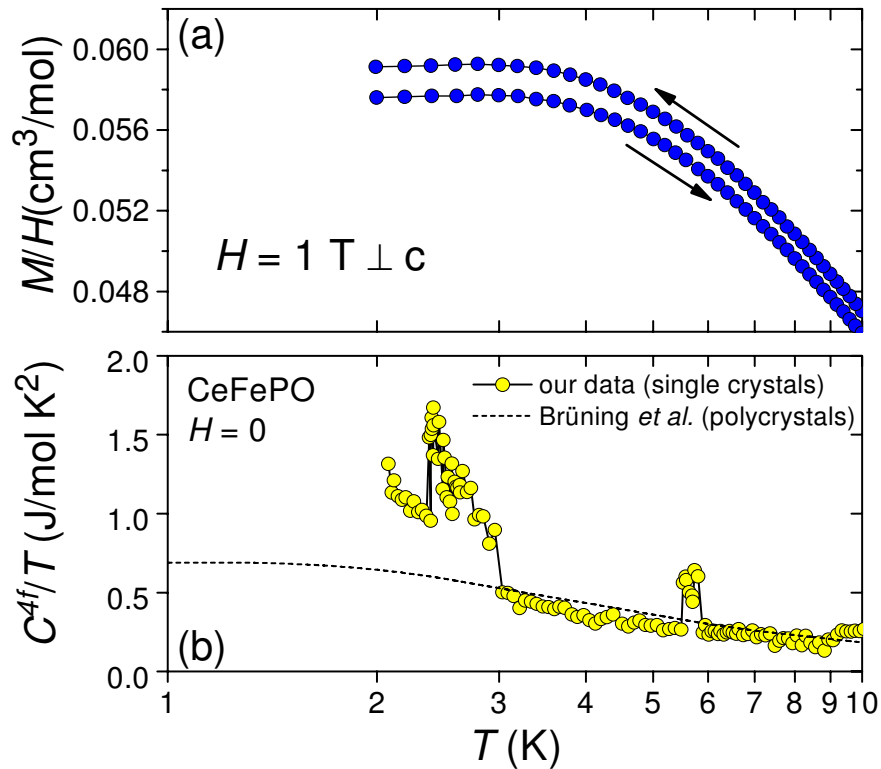


Figure IV.17: Low temperature detail of the magnetization and specific heat measurements performed on annealed single crystals of CeFePO. The magnetization data shown in (a) was taken with a magnetic field of 1 T applied along the c -axis of the crystals, and the arrows indicate the cooling and warming curves. The Ce-contribution to the specific heat shown in (b) was obtained after subtracting the non-magnetic LaFePO data. The dashed line corresponds to the previous results presented in Ref. [45].

IV.E Synthesis and High-Pressure Study of CuFeTe₂ Single Crystals

It has been mentioned in the previous sections that the tetrahedra formed by the Fe atoms with the pnictide or chalcogen atoms, and the apical oxygen height from the Fe planes, together play an important role in controlling the superconducting properties of the iron-based materials. Recently, it was found that superconductivity arises upon the application of pressure to a non-magnetic analog of the Fe-based superconductors, SnO [50]. SnO is a diamagnetic semiconductor at ambient pressure, and it forms in the α -PbO structure, similarly to β -FeSe, which superconducts below $T_c = 8$ K [51]. SnO becomes metallic at room temperature above $P \sim 5$ GPa without a change of the lattice structure up to $P \sim 17$ GPa. In that work, the authors showed that SnO becomes superconducting under pressure $P \geq 6$ GPa with a maximum T_c of 1.4 K at $P \sim 9$ GPa, and that $T_c(P)$ reveals a domelike shape similar to other Fe-based superconductors. Following the same line of thinking, we looked for materials which contained Fe and that also have the same α -PbO structure, finding CuFeTe₂ [52].

Single crystals of CuFeTe₂ were first synthesized by Vaipolin *et al.* [53, 54]. Their x-ray analysis of the grown crystals indicated tetragonal symmetry with unit cell parameters of $a = 3.934 \pm 0.004$ Å and $c = 6.078 \pm 0.004$ Å, and corresponding to the space group P4/nmm, similarly to the “1111” Fe- Pn superconductors. The crystal structure was reported to be, however, a defect Cu₂Sb-type structure, which is identical to the PbO structure but with additional sites in between the Cu/Fe-Te tetrahedra (Fig. IV.18). The Cu and Fe atoms occupied the $2a(0\ 0\ 0)$ -sites, with occupancies of the order of 50% for each of these atoms, and the Te atoms the $2c(0\ \frac{1}{2}\ z)$ -sites. The additional sites at $[2c'-(0\ \frac{1}{2}\ z')]$ were partially filled with Cu and Fe atoms, with an occupancy of less than 15% [54]. For this reason, the structure of CuFeTe₂ seem to be more closely related to the PbO one. From measurements of electrical resistivity and Hall effect, CuFeTe₂ has been identified

as a gapless semiconductor [55].

In previous works, it was found that stoichiometric CuFeTe₂ possessed more than one structural phase at room temperature. For this reason, single crystals with nominal composition of Cu_{1.13}Fe_{1.22}Te₂ were grown. Samples were prepared by standard melt, using high purity materials (Cu shots: AESAR, Johnson Mattney Inc.; Fe powder: ALFA AESAR, 22 mesh, puratronic 99.998%; Te ingot: ALFA AESAR). Elements were weighted inside an argon glovebox with excess of Te, and sealed under vacuum in a quartz tube. The tube was heated in an electrical furnace for 24 hours at 1100 °C, slowly cooled down to 600 °C at a rate of 50 °C/h, and dwelled at 600 °C for another 100 h, after which the furnace was turned off and let cool to room temperature. Fig. IV.19 shows a photograph of a single crystal. The samples are 1 mm golden color platelets, of micaceous characteristics, which make them easy to cleave along the *ab*-planes. X-ray powder diffraction (XRD) measurements were made at room temperature using a diffractometer with a non-monochromated Cu K α source to check the purity and crystal structure of the samples. Due to their malleability, the crystals were difficult to grind into a fine powder. The coarse powder was obtained by grounding several crystals using a mortar and pestle. The Rietveld profile refinement of XRD results using the General Structure Analysis System (GSAS) [56], revealed a good agreement with the Cu₂Sb-type tetragonal structure, with few impurity peaks of unknown origin (Fig. IV.20). In the previous report by Lamarche *et al.* [54], the impurity peaks were attributed to magnetite (Fe₃O₄) or copper ferrite (CuFe₂O₄). Fig. IV.21 displays the magnetization vs. temperature measurements of the CuFeTe₂ samples. A sharp peak occurs at \sim 125 K, below which the zero-field cooled and field-cooled curves saturate at different values. Fe₃O₄ exhibits a metal-insulator transition at this temperature, called the Verwey transition at which the electrical resistivity rises abruptly by two orders of magnitude [57]. Small amounts of magnetite could have been formed inside the quartz tube, which could be responsible for the large magnetic signal observed in our measurements. For this reason, only clean crys-

talline platelets were utilized for the high-pressure resistivity experiments.

Figure IV.22 shows the high-pressure electrical resistivity of CuFeTe₂ measured in the hydrostatic clamped pressure cell. The cell was prepared the same way described previously in Section IV.B. The ambient pressure curve displays non-metallic behavior, in agreement to the semiconductor-like electrical resistivity reported by Vaipolin *et al.* [55]. Upon application of pressure, the resistivity curves start to loose the non-metallic character. The *inset* of Fig. IV.22 displays the resistivity values measured at 4 K as a function of applied pressure (left axis). Modest pressures 2.5 GPa are enough to make the resistivity decrease by almost two orders of magnitude. The measurement taken at 2.43 GPa is very flat, with the resistance changing by only 3% from room temperature to 1 K. Also in the *inset* of Fig. IV.22, the values of energy gap Δ are plotted as a function of pressure. The values of Δ were obtained by plotting $\log\rho(T) = \log\rho_0 + \Delta/k_B T$ and by performing a linear fit in the 180 K $\leqslant T \leqslant$ 300 K region (ρ_0 is the resistivity value at $T \rightarrow 0$ and k_B is the Boltzmann constant). It is clear that the energy gap is reduced by the application of hydrostatic pressure, which is indicative that the sample is acquiring a metallic character.

A small piece of a single crystal of CuFeTe₂ was loaded in a diamond-anvil cell (DAC), as described also in Section IV.B, although in this case a 4-lead designer diamond was used in the piston side, with a culet size of 190 μm in diameter and space between encapsulated leads of $\sim 30 \mu\text{m}$, and a non-matching blank diamond of 300 μm in diameter was placed on the cylinder side. Due to the mismatch of the two diamonds, and in order to protect the designer diamond, maximum pressures of 34 GPa were only applied. Also for this experiment, the sample was surrounded by steatite powder in the remaining space available inside the hole of the metallic gasket, to improve the hydrostatic conditions of the experiment. Fig. IV.23 displays the results of the DAC experiment from room temperature to 1.2 K. Black curves correspond to the measurements taken during the cooling of the probe, while red, green and blue curves were measured during the warming cycles for pressures of

4, 14 and 34 GPa, respectively. The upper panel of Fig. IV.23 shows the electrical resistance curves, showing that at 34 GPa the resistance increases slightly up to \sim 150 K, and that for lower temperatures, it starts to decrease. This effect can be observed more clearly in the lower panel of Fig. IV.23, where the resistance curves are plotted normalized to their respective values of resistance measured at 270 K. A sharp drop at \sim 8 K appears in all the curves, and it is more prominent at the highest pressure. The *inset* of the lower panel Fig. IV.23 displays the low temperature region of the 34 GPa curve measured during warmup. This sharp drop is most probably due to the superconductivity of tellurium, which becomes metallic near 5 GPa and has a high-pressure superconducting phase above 30 GPa, as it was previously discussed in the previous Chapter. It would be certainly interesting to perform further experiments at higher pressures to find out whether an insulating-to-metal transition could be induced by external pressure in samples of CuFeTe₂.

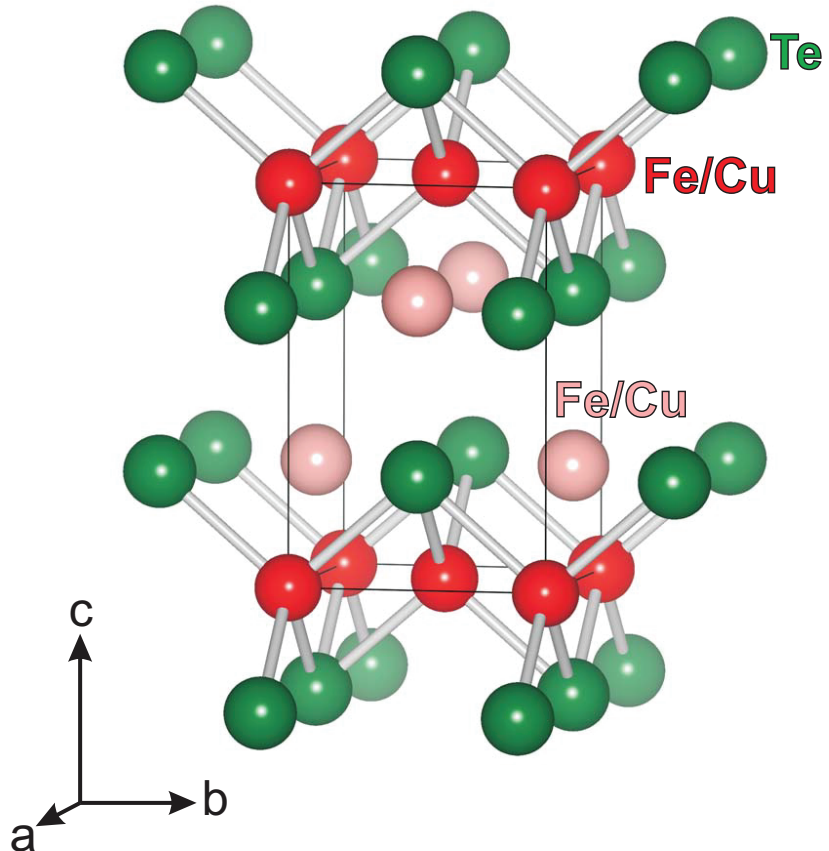


Figure IV.18: Crystal structure of CuFeTe₂. Cu and Fe atoms (*red*) occupy the $2a(0\ 0\ 0)$ -sites, with occupancies of the order of 50%, with the Te atoms (*green*) tetrahedrally coordinated with the Cu/Fe atoms. In the defect Cu₂Sb structure, additional sites at $[2c'-(0\ \frac{1}{2}\ z')]$ are partially occupied ($\lesssim 15\%$) by Cu and Fe atoms.

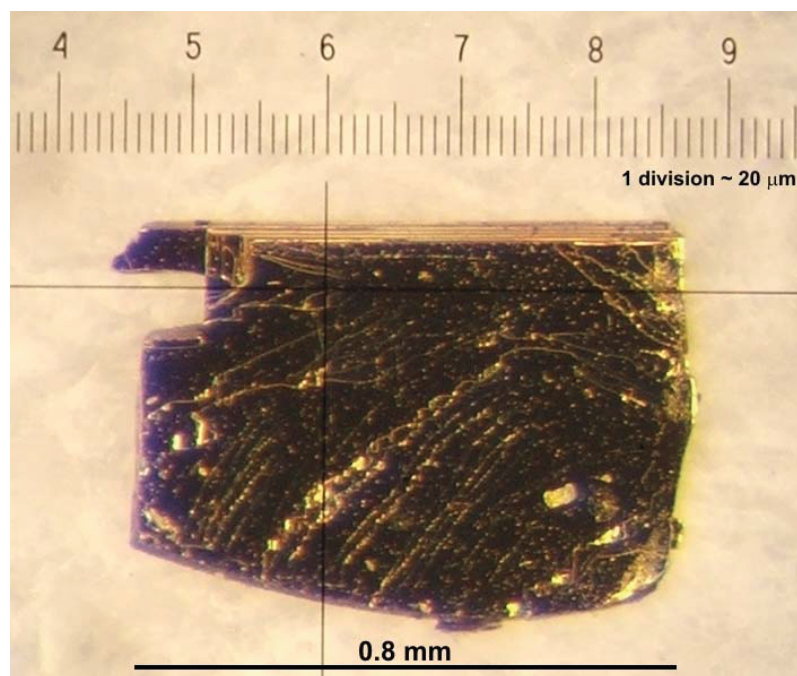


Figure IV.19: Photography of a single crystal of CuFeTe₂. Typical platelets are $\sim 50 \mu\text{m}$ thick.

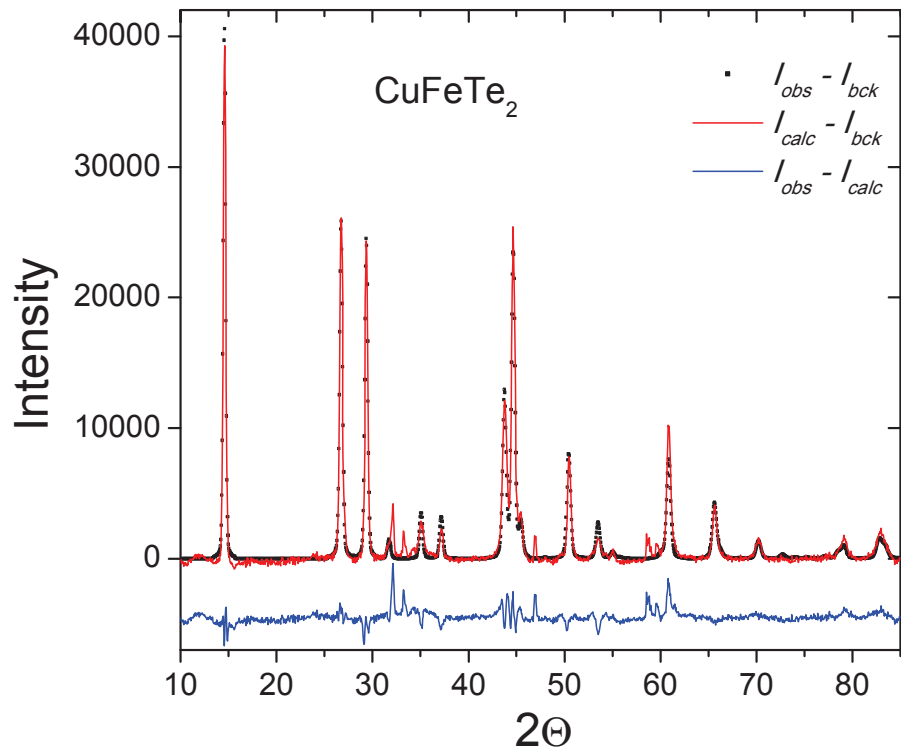


Figure IV.20: Powder x-ray diffraction pattern of CuFeTe₂ ($I_{obs} - I_{bck}$, black squares). The fit to the data was obtained from the Rietveld analysis ($I_{calc} - I_{bck}$, red line). The background was subtracted from the experimental data and the fit. The blue line indicates the difference between observed and calculated data.

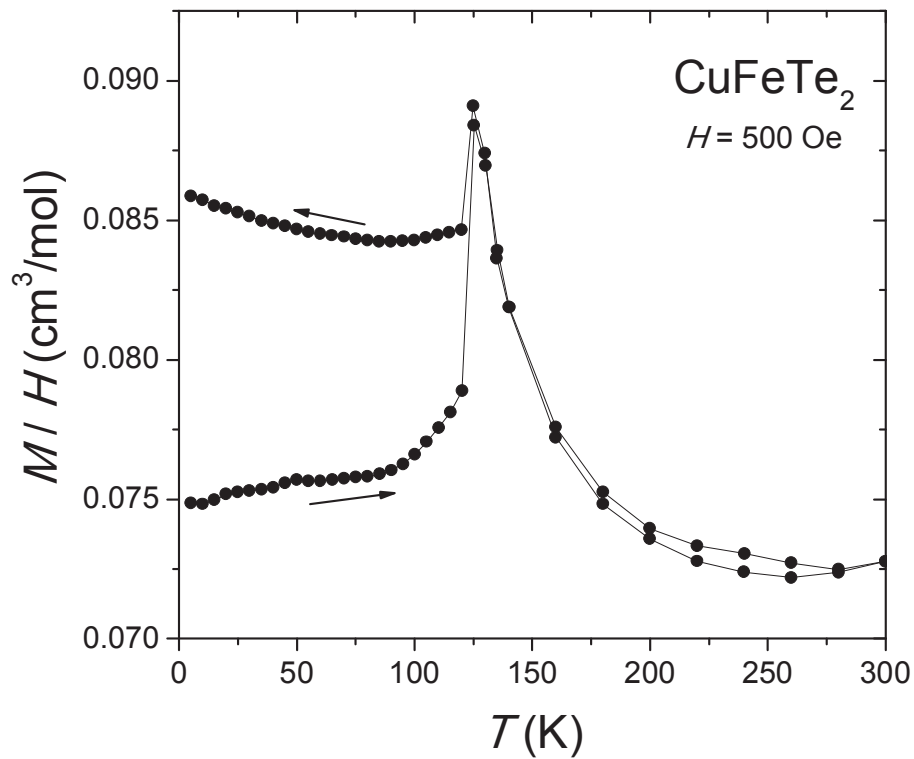


Figure IV.21: Zero-field cooled and field-cooled magnetization M versus temperature T of CuFeTe_2 obtained with an applied magnetic field of 500 Oe. The prominent feature at 125 K is consistent with the Verway transition found in magnetite (Fe_3O_4) [57].

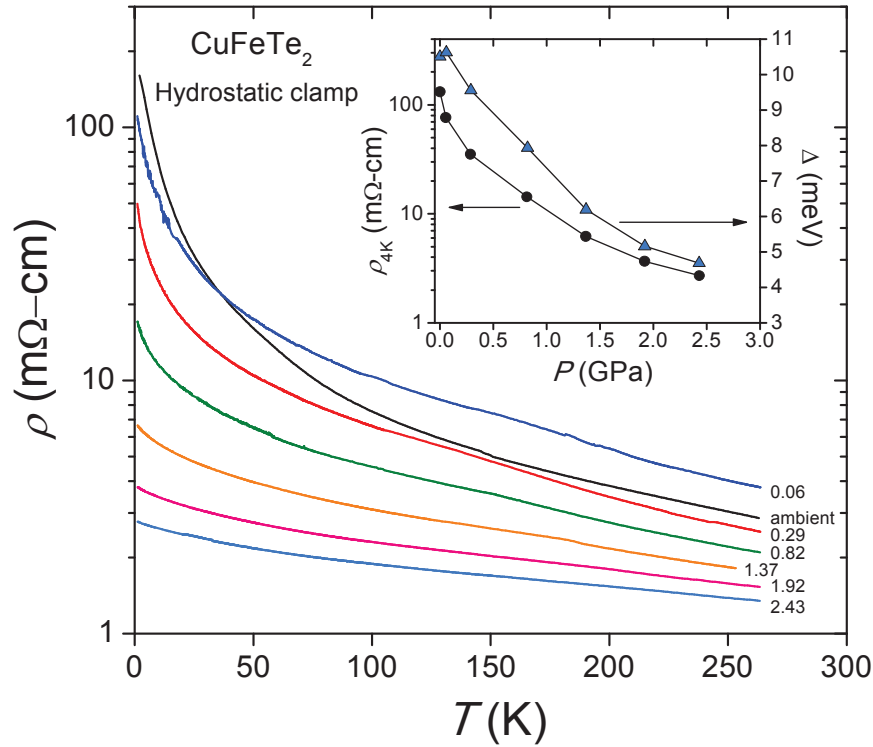


Figure IV.22: Electrical resistivity ρ versus temperature T of CuFeTe_2 obtained in the hydrostatic clamped-cell experiment. The *inset* shows, in the left axis, the values of resistivity ρ_{4K} measured at 4 K as a function of pressure, and in the right axis, the energy gap values Δ also as a function of pressure, obtained as described in the main text.

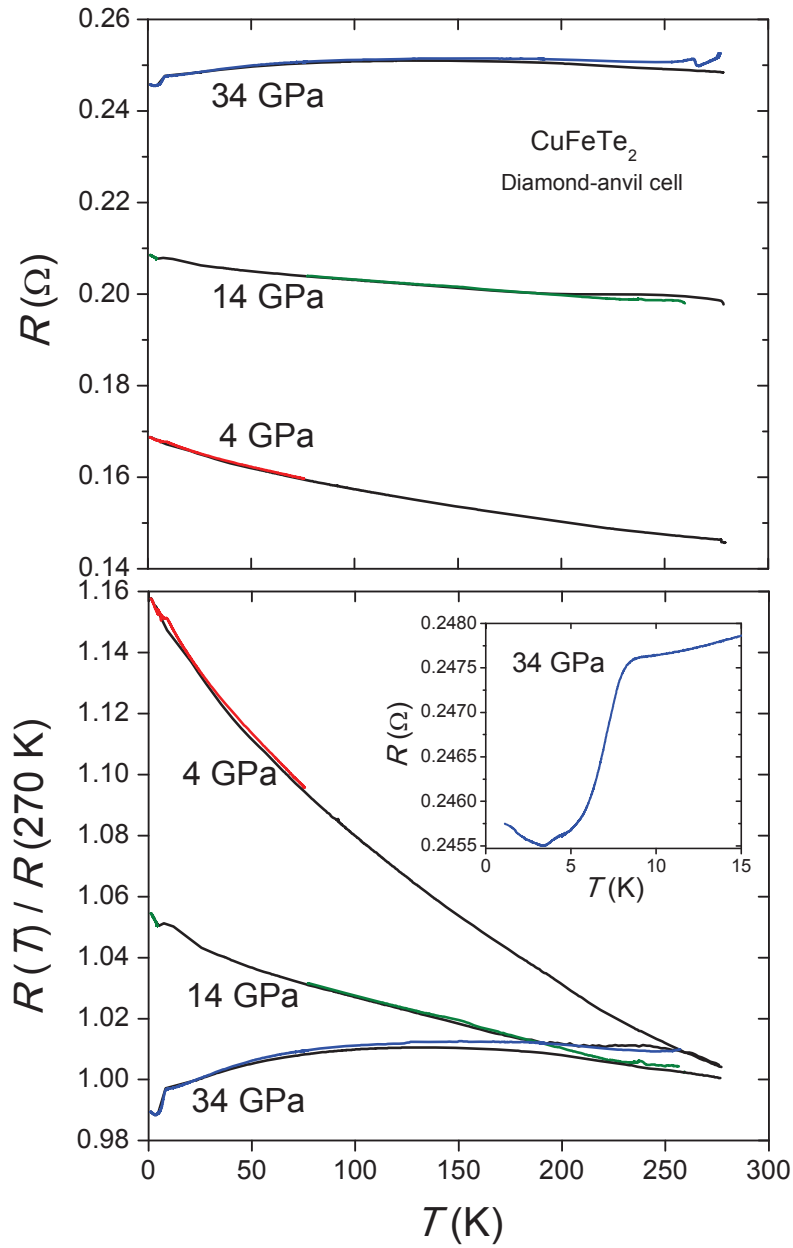


Figure IV.23: Electrical resistance R versus temperature T of CuFeTe₂ obtained in the diamond-anvil cell experiment. Black curves correspond to the measurements taken during the cooling of the probe, while red, green and blue curves were measured during the warming cycles for pressures of 4, 14 and 34 GPa, respectively. The lower panel displays the resistance curves normalized to their respective values of resistance measured at 270 K. The *inset* shows in detail the low temperature region of the 34 GPa curve measured during the warm-up cycle.

IV.F Summary

The discovery of high temperature superconductivity in 2008 in the iron-based materials has attracted an immense amount of attention during the last three years since these compounds have the highest values of critical temperature found since the discovery of the cuprates in 1986. High pressure investigations of iron-based compounds have contributed significantly to a better understanding of this new class of materials, although it was not possible to increase the superconducting temperature beyond the 56 K limit. However, in all measured samples, it was found that the superconducting temperature vs. pressure phase diagram presents a dome-like shape, similarly to the cuprates, and that pressure serves as a tuning parameter of the doping of the Fe-pnictide planes. The superconducting $\text{LaFeAsO}_{1-x}\text{F}_x$, $\text{CeFeAsO}_{1-x}\text{F}_x$ and LaFePO compounds all display a superconducting dome of T_c vs. pressure, reaching maximum superconducting temperatures of 32 K, 47 K, and 14 K, respectively. The experiments carried out with the LaFePO single crystals raise the question of what role is the hydrostaticity of the pressure medium playing in determining the superconducting phase diagram of the Fe-pnictide materials.

In CeFeAsO polycrystals, it was found that the magnetic phases involving the Fe and Ce ions coexist for hydrostatically applied pressures up to 15 GPa, and with no signs of pressure-induced superconductivity up to 50 GPa for the less hydrostatic pressure techniques. For the CeFePO single crystals, pressure further stabilizes the Kondo screening of the Ce $4f$ -electron magnetic moments, and it was found that annealing the samples modify the low temperature properties of the CeFePO single crystals, although further examination of these properties should be carried out.

CuFeTe_2 has a crystal structure similar to that of the Fe-based superconductors. Single crystals of CuFeTe_2 were synthesized after slowly cooling the melt. The high-pressure study of the electrical resistivity showed that this compound loses its semiconducting behavior when is subject to pressures of ~ 30 GPa,

with a possible metal-insulator transition occurring at that pressure. Chemical substitution or doping of CuFeTe₂ would change the electronic properties of this compound, and it could induce a superconducting state, as it was previously done with the non-superconducting Fe-based materials.

Bibliography

- [1] T. Watanabe, Y. Yanagi, T. Kamiya, Y. Kamihara, H. Hiramatsu, M. Hirano, and H. Hosono, Inorg. Chem. **46**, 7719 (2007).
- [2] Y. Kamihara, H. Hiramatsu, M. Hirano, R. Kawamura, H. Yanagi, T. Kamiya, and H. Hosono, J. Am. Chem. Soc. **128**, 10012 (2006).
- [3] Y. Kamihara, T. Watanabe, M. Hirano, and H. Hosono, J. Am. Chem. Soc. **130**, 3296 (2008).
- [4] H. Takahashi, K. Igawa, K. Arii, Y. Kamihara, M. Hirano, and H. Hosono, Nature **453**, 376 (2008).
- [5] Z. -A. Ren, W. Lu, J. Yang, W. Yi, X. -L. Shen, Z. -C. Li, G. -C. Che, X. -L. Dong, L. -L. Sun, F. Zhou, and Z. -X. Zhao, Chin. Phys. Lett. **25**, 2215 (2008).
- [6] B. Lorenz, K. Sasmal, R.P. Chaudhury, X.H. Chen, R.H. Liu, T. Wu, C.W. Chu, Phys. Rev. B **78**, 012505 (2008).
- [7] H. Okada, K. Igawa, H. Takahashi, Y. Kamihara, M. Hirano, H. Hosono, K. Matsubayashi, and Y. Uwatoko, J. Phys. Soc. Japan **77**, 113712 (2008).
- [8] M. Rotter, M. Tegel, and D. Johrendt, Phys. Rev. Lett. **101**, 107006 (2008).
- [9] J. H. Tapp, Z. Tang, B. Lv, K. Sasmal, B. Lorenz, P. C. W. Chu, and A. M. Guloy, Phys. Rev. B **78**, 060505(R) (2008).
- [10] F. -C. Hsu, J. -Y. Luo, K. -W. Yeh, T. -K. Chen, T. -W. Huang, P. M. Wu, Y. -C. Lee, Y. -L. Huang, Y. -Y. Chu, D. -C. Yan, and M. -K. Wu, Proc. Nat. Acad. Sci. USA **105**, 14262 (2008).
- [11] C. de la Cruz, Q. Huang, J. W. Lynn, J. Li, W. R. II, J. L. Zarestky, H. A. Mook, G. F. Chen, J. L. Luo, N. L. Wang, and P. Dai, Nature (London) **453**, 899 (2008).
- [12] J. Zhao, Q. Huang, C. de la Cruz, S. L. Li, J. W. Lynn, Y. Chen, M. A. Green, G. F. Chen, G. Li, Z. Li, J. L. Luo, N. L. Wang, and P. Dai, Nat. Mater. **7**, 953 (2008).
- [13] C. -H. Lee, A. Iyo, H. Eisaki, H. Kito, M. T. Fernandez-Diaz, T. Ito, K. Kihou, H. Matsuhata, M. Braden, and K. Yamada, J. Phys. Soc. Jpn. **77**, 083704 (2008).
- [14] M. Mito, M. J. Pitcher, W. Crichton, G. Garbarino, P. J. Baker, S. J. Blundell, P. Adamson, D. R. Parker, and S. J. Clarke, J. Am. Chem. Soc. **131**, 2986 (2009).

- [15] S. A. J. Kimber, A. Kreyssig, Y. -Z. Zhang, H. O. Jeschke, R. Valent, F. Yokaichiya, E. Colombier, J. Yan, T. C. Hansen, T. Chatterji, R. J. McQueeney, P. C. Canfield, A. I. Goldman, and D. N. Argyriou, *Nat. Mater.* **8**, 471 (2009).
- [16] D. R. Parker, M. J. P. Smith, T. Lancaster, A. J. Steele, I. Franke, P. J. Baker, F. L. Pratt, M. J. Pitcher, S. J. Blundell, and S. J. Clarke, *Phys. Rev. Lett.* **104**, 057007 (2010).
- [17] P. G. De Gennes, *Journal de Physique et Le Radium* **23**, 510 (1962).
- [18] R. E. Baumbach, J. J. Hamlin, L. Shu, D. A. Zocco, N. M. Crisosto, and M. B. Maple, *New J. Phys.* **11**, 025018 (2009).
- [19] A. J. Drew, F. L. Pratt, T. Lancaster, S. J. Blundell, P. J. Baker, R. H. Liu, G. Wu, X. H. Chen, I. Watanabe, V. K. Malik, A. Dubroka, K. W. Kim, M. Rössle, and C. Bernhard, *Phys. Rev. Lett.* **101**, 097010 (2008).
- [20] K. Momma and F. Izumi, *VESTA: a three-dimensional visualization system for electronic and structural analysis*. *J. Appl. Crystallogr.* **41**, 653-658, (2008).
- [21] A. S. Sefat, M. A. McGuire, B. C. Sales, R. Jin, J. Y. Howe, and D. Mandrus, *Phys. Rev. B* **77**, 174503 (2008).
- [22] M. A. McGuire, R. P. Hermann, A. S. Sefat, B. C. Sales, R. Jin, D. Mandrus, F. Grandjean, and G. J. Long, *New J. Phys.* **11**, 025011 (2009).
- [23] B. Bireckoven and J. Wittig, *J. Phys. E* **21**, 841 (1988).
- [24] T. F. Smith, C. W. Chu, and M. B. Maple, *Cryogenics* **9**, 53 (1969).
- [25] S. T. Weir, J. Akella, C. Aracne-Ruddle, Y. K. Vohra, and S. A. Catledge, *Appl. Phys. Lett.* **77**, 3400 (2000).
- [26] A. D. Chijioke, W. J. Nellis, A. Soldatov, I. F. Silvera, *J. Appl. Phys.* **98** (11), 114905 (2005).
- [27] D. D. Jackson, J. R. Jeffries, W. Qiu, J. D. Griffith, S. McCall, C. Aracne, M. Fluss, M. B. Maple, S. T. Weir, and Y. K. Vohra, *Phys. Rev. B* **74**, 174401 (2006).
- [28] G. Garbarino, P. Toulemonde, M. Álvarez-Murga, A. Sow, M. Mezouar, and M. Núñez-Regueiro, *Phys. Rev. B* **78**, 100507(R) (2008)
- [29] I. R. Shein and A. L. Ivanovskii, [jcond-mat/0804.0712](https://arxiv.org/abs/0804.0712) (2008).
- [30] W. Lu, X. -L. Shen, J. Yang, Z. -C. Li, W. Yi, Z. -A. Ren, X. -L. Dong, G. -C. Che, L. -L. Sun, F. Zhou, and Z. -X. Zhao, *Solid State Commun.* **148**, 168 (2008).

- [31] J.S. Schilling, What High Pressure Studies have Taught us About High-Temperature Superconductivity. *Frontiers of High Pressure Research II: Application of High Pressure to Low-Dimensional Novel Electronic Materials*, Kluwer Academic Publishers, pp. 345360 (2001).
- [32] G. F. Chen, Z. Li, D. Wu, G. Li, W. Z. Hu, J. Dong, P. Zheng, J. L. Luo, and N. L. Wang, *Phys. Rev. Lett.* **100**, 247002 (2008).
- [33] A. Jesche, C. Krellner, M. de Souza, M. Lang, and C. Geibel, *Phys. Rev. B* **81**, 134525 (2010).
- [34] J. S. Schilling, *Adv. Phys.* **28**, 657 (1979).
- [35] M. B. Maple, *J. Phys. Soc. Jpn.* **74**, 222 (2005)
- [36] S. Doniach, *Physica B* **91**, 231 (1977).
- [37] L. Pourovskii, V. Vildosola, S. Biermann, and A. Georges, *Europhys. Lett.* **84**, 37006 (2008).
- [38] V. A. Sidorov and R. A. Sadykov, *J. Phys. Condens. Matter* **17**, S3005 (2005)
- [39] W. Bi, H. B. Banks, J. S. Schilling, H. Takahashi, H. Okada, Y. Kamihara, M. Hirano, and H. Hosono, *New J. Phys.* **12**, 023005 (2010).
- [40] T. M. McQueen, M. Regulacio, A. J. Williams, Q. Huang, J. W. Lynn, Y. S. Hor, D. V. West, M. A. Green, and R. J. Cava, *Phys. Rev. B* **78**, 024521 (2008).
- [41] V. Vildosola, L. Pourovskii, R. Arita, S. Biermann, and A. Georges, *Phys. Rev. B* **78**, 064518 (2008).
- [42] J. A. Wilson, *J. Phys. Condens. Matter* **22**, 203201 (2010).
- [43] K. Igawa, H. Okada, K. Arii, H. Takahashi, Y. Kamihara, M. Hirano, H. Hosono, S. Nakano, and T. Kikegawa, *J. Phys. Soc. Jpn.* **78**, 023701 (2009).
- [44] J. S. Schilling *et al.*, private communication.
- [45] E. M. Brüning, C. Krellner, M. Baenitz, A. Jesche, F. Steglich, and C. Geibel, *Phys. Rev. Lett.* **101**, 117206 (2008).
- [46] Y. Luo, Y. Li, S. Jiang, J. Dai, G. Cao, and Z. A. Xu, *Phys. Rev. B* **81**, 134422 (2010).
- [47] C. de la Cruz, W. Z. Hu, S. Li, Q. Huang, J. W. Lynn, M. A. Green, G. F. Chen, N. L. Wang, H. A. Mook, Q. Si, and P. Dai, *Phys. Rev. Lett.* **104**, 017204 (2010).

- [48] M. B. Maple and D. K. Wohlleben, in Magnetism and Magnetic Materials 1973, AIP Conference Proceedings No. 18, edited by C. D. Graham Jr. and J. J. Rhyne (American Institute of Physics, New York, 1974), p. 447.
- [49] A. Ślebarski, M. Radłowska, T. Zawada, M. B. Maple, A. Jezierski, and A. Zygmunt, Phys. Rev. B **66**, 104434 (2002).
- [50] M. K. Forthaus, K. Sengupta, O. Heyer, N. E. Christensen, A. Svane, K. Syassen, D. I. Khomskii, T. Lorenz, and M. M. Abd-Elmeguid, Phys. Rev. Lett. **105**, 157001 (2010).
- [51] C. W. Chu and B. Lorenz, Physica C **469**, 385 (2009).
- [52] P. Villars, *Pearson's Handbook Desk Edition, Crystallographic Data for Intermetallic Phases* (ASM International, Materials Park, OH, 1997), Vol. 1, p. 1221.
- [53] A. A. Vaipolin, V. D. Prochukhan, V. Yu. Rud, V. E. Skoriukin, Izv. Acad. Nauk. SSSR Neorg. Mater. **20**, 578 (1984).
- [54] A. M. Lamarche, J. C. Woolley, G. Lamarche, I. P. Swainson, and T. M. Holden, J. Magn. Magn. Mater. **186**, 121 (1998).
- [55] A. A. Vaipolin, S. A. Kijaev, L. V. Kradinova, A. M. Polubetko, V. V. Popov, V. D. Prochukhan, V. Yu. Rud, V. E. Skoriukin, J. Phys.: Condens. Mater. **4**, 8035 (1992).
- [56] A. C. Larson, R. B. Von Dreele, General Structure Analysis System, MS-H805, Los Alamos National Laboratory, Neutron Scattering Center (Copyright, The Regent of the University of California, 1993).
- [57] E. J. W. Verwey, Nature **144**, 327 (1939).

A portion of the text and data presented in this chapter are reprints of material that appears in “Effect of pressure on the superconducting critical temperature of $\text{La}[\text{O}_{0.89}\text{F}_{0.11}]\text{FeAs}$ and $\text{Ce}[\text{O}_{0.88}\text{F}_{0.12}]\text{FeAs}$,” D. A. Zocco, J. J. Hamlin, R. E. Baumbach, M. B. Maple, M. A. McGuire, A. S. Sefat, B. C. Sales, R. Jin, D. Mandrus, J. R. Jeffries, S. T. Weir, and Y. K. Vohra, *Physica C* **468**, 2229 (2008), “Superconductivity in single crystals of LaFePO ,” J. J. Hamlin, R. E. Baumbach, D. A. Zocco, T. A. Sayles, and M. B. Maple, *Journal of Physics: Condensed Matter* **20**, 365220 (2008), “Superconductivity in LnFePO ($\text{Ln} = \text{La, Pr, and Nd}$) single crystals,” R. E. Baumbach, J. J. Hamlin, L. Shu, D. A. Zocco, N. Crisosto, and M. B. Maple, *New J. of Phys.* **11**, 025018 (2009), and “Search for pressure induced superconductivity in CeFeAsO and CeFePO iron pnictides,” D. A. Zocco, R. E. Baumbach, J. J. Hamlin, M. Janoschek, I. K. Lum, M. A. McGuire, A. S. Sefat, B. C. Sales, R. Jin, D. Mandrus, J. R. Jeffries, S. T. Weir, Y. K. Vohra, and M. B. Maple, *Phys. Rev. B* **83**, 094528 (2011). The dissertation author is a primary researcher and first author of the first and fourth articles, primary researcher and third author of the second article, and co-author of the third article.